
Multi-resolution nowcasting of clouds and DNI with MSG/SEVIRI for an optimized operation of concentrating solar power plants

Tobias Sirch



München 2017

Multi-resolution nowcasting of clouds and DNI with MSG/SEVIRI for an optimized operation of concentrating solar power plants

Tobias Sirch

Dissertation
an der Fakultät für Physik
der Ludwig-Maximilians-Universität
München

vorgelegt von
Tobias Sirch
aus Mindelheim

München, den 14. Dezember 2017

Erstgutachter: Prof. Dr. Bernhard Mayer
Zweitgutachter: Prof. Dr. Markus Rapp
Tag der mündlichen Prüfung: 15.03.2018

Zusammenfassung

Eine funktionierende Energieversorgung ist unerlässlich für die wirtschaftliche Entwicklung einer Gesellschaft und die Nachfrage erhöht sich stetig. Dabei ist der Anteil erneuerbarer Energien am gesamten Energieverbrauch über die letzten Jahre angestiegen, ein Trend, der sich auch in den nächsten Jahrzehnten fortsetzen wird. Deshalb werden Methoden benötigt, die eine optimale Nutzung erneuerbarer Ressourcen, wie z.B. solarthermischer Kraftwerke mit Strahlungsbündelung (CSP), ermöglichen. Aufgrund der hohen räumlichen und zeitlichen Variabilität der Sonnenenergie ist ein Betrieb dieser CSP-Kraftwerke sehr anspruchsvoll.

In dieser Arbeit wird ein neuartiger Ansatz für die Kurzfristvorhersage von Wolken und Direktnormalstrahlung (DNI) vorgestellt, welcher auf dem Wolkensensor "Spinning Enhanced Visible and Infrared Imager" (SEVIRI) an Bord des geostationären "METEOSAT Second Generation" (MSG) Satelliten basiert. Dabei beträgt der Vorhersagezeitraum 120 Minuten mit einer zeitliche Auflösung von 5 Minuten. Der Algorithmus basiert auf einer "optical flow" Methode, die für alle bewölkten Pixel Verschiebungsvektoren bestimmt. Um Vorhersagen über einen entsprechenden Zeitraum zu ermöglichen, wird eine Klassifizierung von Wolken als Objekte und eine gewichtete Dreiecksinterpolation der wolkenfreien Gebiete angewendet. Niedrige und hohe Wolken werden getrennt detektiert und vorhergesagt, da sie unterschiedliche Geschwindigkeiten und Bewegungsrichtungen aufweisen können. Zusätzlich wird eine Unterscheidung in advektive und konvektive Wolken in Verbindung mit einer Intensitätskorrektur für sich schnell auflösende konvektive Zellen eingefügt. Die DNI wird aus der prognostizierten optischen Dicke der niedrigen und hohen Wolken berechnet. Um die Leistung des Algorithmus quantitativ bewerten zu können, wird eine Vorhersagevalidierung mit MSG/SEVIRI-Beobachtungen über einen Zeitraum von zwei Monaten durchgeführt. Bei einer 5-minütigen Vorhersage werden in den meisten Wolkensituationen mehr als 95% aller Pixel korrekt als bewölkt oder wolkenfrei klassifiziert. Diese Zahl verringert sich für eine 2-stündige Vorhersage auf 80-95% abhängig vom vorherrschendem Wolkentyp. Die "Hanssen-Kuiper skill scores" der Wolkenmasken verringern sich auf 0.6-0.7 für eine 2-stündige Vorhersage. Eine Validierung mit Strahlungsmessungen am Boden an einem Standort über einen Zeitraum von drei Monaten ergibt einen mittleren Fehler um null, einen mittleren absoluten Fehler von $\sim 200 \text{ W/m}^2$ und einen mittleren quadratischen Fehler von $\sim 360 \text{ W/m}^2$ für eine Vorhersage von zwei Stunden.

Um eine Verbesserung in der Vorhersagegenauigkeit zu ermitteln, wurde der Nutzen des hochaufgelösten Kanals (HRV) von MSG/SEVIRI untersucht. Mithilfe einer synergetischen Nutzung der niedrig- und hochaufgelösten MSG/SEVIRI-Daten werden Wolkenmasken und Wolkenphasenmasken bestimmt sowie die optische Dicke der Wolken mit Strahlungstransportrechnungen. Eine statistische Evaluierung mit Strahlungsmessungen am Boden und drei Fallstudien zeigen eine Verbesserung in Vorhersagegenauigkeit für kleinskalige Bewölkung und an Wolkenkanten für Vorhersagen bis zu 15 Minuten. Aber für die meisten Fälle und

II

längere Vorhersagezeiträume sollten die Vorhersagen mit Bewegungsvektoren erstellt werden, die mit niedrigaufgelösten Satellitendaten bestimmt wurden, da diese eher dazu geeignet sind die großskaligen atmosphärischen Strömungen wiederzugeben.

Um lokale Wolkensituationen an einem spezifischen Standort genauer zu charakterisieren, werden sogenannte "all-sky imagers" verwendet, da sie Wolken in höherer Auflösung bestimmen können. Dafür wurde ein neuartiger Ansatz zur Kombination von Kamera- und Satellitendaten entwickelt, der die höhere räumliche Auflösung der Kamera mit der großen räumlichen Abdeckung des Satelliten kombiniert und somit Vorhersagen mit einer zeitlichen Auflösung von einer Minute ermöglicht. Die höhere räumliche Auflösung der Kamera erlaubt eine genauere Bestimmung und Vorhersage der DNI als mit Satellitendaten allein bis zu einem Vorhersagezeitraum von 30 Minuten oder mehr für bestimmte Situationen, z.B. an Wolkenkanten und im Falle von kleinskaliger Bewölkung.

Abstract

A functioning power supply is crucial for the economical evolution of society and the demand is constantly rising. The share of renewable energy in overall energy consumption has increased in the last years, a trend that will continue in the next decades. For this, methods are required which allow for an optimal use of the renewable resources, such as concentrating solar power (CSP) systems. As solar resources are very variable in space and time the operation of CSP systems is challenging.

A novel multi-resolution approach for the nowcasting of clouds and Direct Normal Irradiance (DNI) based on the Spinning Enhanced Visible and Infrared Imager (SEVIRI) aboard the geostationary Meteosat Second Generation (MSG) satellite for a forecast horizon up to 120 min and a forecast temporal resolution of 5 min is presented in this work. The basis of the algorithm is an optical flow method to derive cloud motion vectors for all cloudy pixels. To facilitate forecasts over a relevant time period, a classification of clouds into objects and a weighted triangular interpolation of clear-sky regions are used. Low and high level clouds are identified and forecasted separately because they show different velocities and motion directions. Additionally, a distinction in advective and convective clouds together with an optical thickness correction for quickly thinning convective clouds are integrated. The DNI is calculated from the forecasted optical thickness of the low and high level clouds. In order to quantitatively assess the performance of the algorithm, a forecast validation against MSG/SEVIRI observations is performed for a period of two months. For a forecast of 5 min for most cloud situations more than 95% of all pixels are predicted correctly cloudy or clear. This number decreases to 80-95% for a forecast of 2 h depending on cloud type and vertical cloud level. Hanssen-Kuiper skill scores for cloud masks go down to 0.6-0.7 for a 2 h forecast. Compared to persistence an improvement of forecast horizon by a factor of two is reached for all forecasts up to 2 h. A validation against ground-based irradiance measurements at one site over a period of three months shows a mean bias error around zero, a mean absolute error of $\sim 200 W/m^2$ and a root mean square error of $\sim 360 W/m^2$ for a forecast lead time of 2 h.

In order to examine the enhancement in forecast accuracy the benefit of the high resolution channel (HRV) of MSG/SEVIRI is investigated. By means of a synergistic exploitation of high and low resolution MSG/SEVIRI data cloud masks as well as cloud phase masks are determined in high resolution and cloud optical thickness is derived with radiative transfer calculations. A statistical evaluation against ground-based irradiance measurements and three case studies show an improvement in forecast accuracy for small-scale clouds and at cloud edges for forecast lead times up to 15 min when compared to forecasts in low resolution, but for most cases and longer lead times the forecasts should be performed with motion vectors derived in low resolution as those are more appropriate to represent the large-scale atmospheric flow.

In order to better characterise the local cloud situation at a specific site all-sky

imagers have been used to identify clouds in higher resolution. For this, a novel approach for the combination of camera and satellite data is performed, thus combining the camera's higher spatial resolution with the large spatial coverage of the satellite performing forecasts with a temporal resolution of 1 min. The higher spatial resolution of the cameras enables a more accurate determination and forecast of DNI than with satellite data up to a forecast lead time of 30 min or more for certain situations, i.e. at cloud edges and in case of small-scale clouds.

Contents

1	Introduction	1
2	Theoretical background	9
2.1	Radiative transfer quantities	9
2.2	Interaction of radiation with matter	10
2.2.1	Absorption	11
2.2.2	Scattering	11
2.2.3	Atmospheric extinction	14
2.2.4	Lambert-Beer's law	14
2.2.5	Emission	15
2.3	Radiative transfer equation	15
2.4	Cloud properties	17
2.5	Aerosols	18
2.6	Solar irradiance at TOA and the surface	18
2.7	Direct Normal Irradiance at the surface	19
2.8	Passive remote sensing	21
3	Instrumentation and Methods	23
3.1	Cloud remote sensing with MSG/SEVIRI	23
3.1.1	Instrument	23
3.1.2	Ice cloud detection (COCS)	25

3.1.3	Water and ice cloud optical properties (APICS)	27
3.1.4	Detection of convective clouds (Cb-TRAM)	27
3.2	Ground observation of clouds with all-sky imagers	28
3.2.1	Camera	28
3.2.2	Calibration	29
3.2.3	Cloud mask	31
3.3	DNI measurements with pyrhemometers	32
3.4	Cloud motion analysis using scale dependent image matching . . .	32
3.5	Satellite-based nowcasting methods	35
4	Forecast of clouds and DNI with low resolution MSG/SEVIRI data	39
4.1	Cloud classification	40
4.1.1	Cloud optical properties	40
4.1.2	Convective clouds	43
4.2	Forecast algorithm	44
4.2.1	Pixel-based motion vectors	45
4.2.2	Object-based cloud motion vectors	47
4.2.3	Cloud-free background	50
4.2.4	Optical thickness correction for quickly thinning convective clouds	51
4.2.5	DNI parameterisation	55
4.3	Cloud forecast verification	57
4.3.1	Cloud masks	57
4.3.2	Cloud optical thickness	62
4.3.3	Direct Normal Irradiance	63
4.4	Case studies	65
4.4.1	Parallax correction	65

4.4.2	24 June 2014	67
4.4.3	8 September 2014	70
4.4.4	25 June 2014	72
4.5	Systematic validation of DNI	73
4.5.1	Selected cases	74
4.5.2	Statistical evaluation	77
4.5.3	Comparison and validation of forecasted DNI for all cases .	78
4.5.4	Comparison and validation of forecasted DNI with respect to cloud types	80
4.6	Conclusions	83
5	Synergistic use of high and low resolution MSG/SEVIRI data for an improved cloud and DNI forecast	85
5.1	Synergistic cloud mask	86
5.1.1	Challenges	86
5.1.2	HRV cloud detection	86
5.1.3	HRV cloud classification	89
5.2	Synergistic cloud optical properties	89
5.2.1	Input parameter	90
5.2.2	Uncertainties: atmospheric gas extinction	92
5.3	Forecast in high resolution	93
5.4	Case studies	94
5.4.1	24 June 2014	94
5.4.2	8 September 2014	97
5.4.3	25 June 2014	98
5.5	Statistical evaluation	99
5.6	Conclusions	103

6 Synergistic use of all-sky imagers and MSG/SEVIRI data for an improved cloud and DNI forecast	105
6.1 Collocation of ASI and MSG/SEVIRI	105
6.2 Forecast	108
6.3 Case studies	109
6.3.1 24 June 2014	109
6.3.2 8 September 2014	111
6.3.3 25 June 2014	113
6.4 Conclusions	114
7 Summary, Conclusions and Outlook	115
7.1 Summary and Conclusions	115
7.2 Outlook	118
Literaturverzeichnis	121

Chapter 1

Introduction

Availability of power plays a central role for society and its economical evolution. Due to rising commodity prices for fossil fuels and the anthropogenic greenhouse effect the power supply with clean (CO_2 neutral) renewable energy gains in importance. For this, the share of renewable energy in overall energy consumption has increased in the last years, a trend that will continue in the near future [U.S. Energy Information Administration (EIA), 2016]. Renewables are the fastest-growing source of energy for electricity generation, with expected global annual increases averaging 2.9% from 2012 to 2040 (Fig. 1.1).

Next to wind power and hydropower, solar energy is one of the main contributor to renewable energy (12.5% of the world net electricity generation from renewable power in 2016, Renewable Energy Policy Network for the 21st Century (REN21) [2016]) using multiple techniques, e.g. photovoltaics (PV) or concentrating solar power (CSP) systems, which account for $\sim 2\%$ of solar energy generation. The great potential of CSP systems lies in the combination of electricity production and thermal storage capacity (e.g. molten salt), if present. By means of mirrors the incoming solar irradiance is concentrated, heating a fluid (oil, water/steam or molten salt) and driving a heat engine. In the focal point/line the flux of radiant energy is orders of magnitude larger compared to non-concentrating technologies, thus allowing higher conversion efficiencies due to the high energy density. The used technologies are parabolic trough, Fresnel reflectors, dish Stirling and solar power tower (Fig. 1.2). In case of low insolation or for periods of high variability the electricity production is taken over by the storage or a fuel (e.g. gas) for a system without storage, which can also be used to support the start-up process. The time which can be bridged by a storage system depends on the storage size and may typically last up to 10 hours. A storage is also able to reduce changes in the power output of a power plant, so-called ramps, which can negatively affect power quality and the network reliability [de la Parra et al., 2015, Marcos et al., 2014, Denholm and Mehos, 2012]. The installation and usage of these backup systems increase the operating costs of solar power plants.

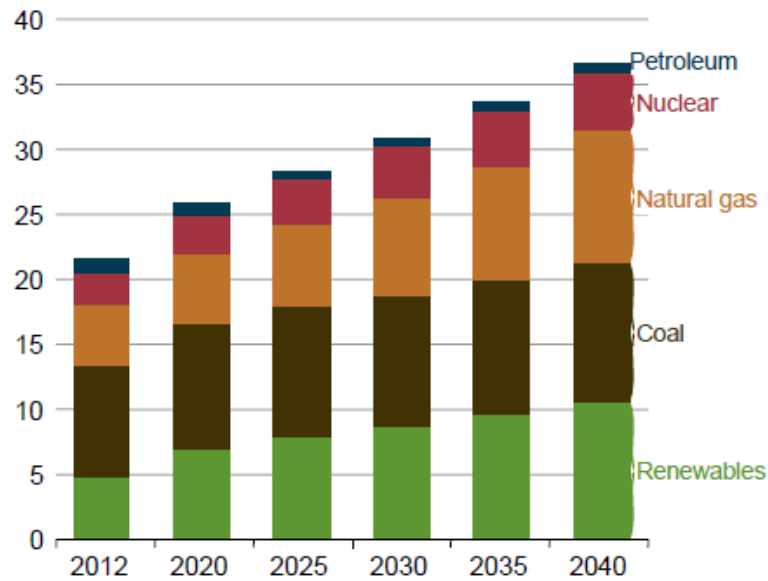


Figure 1.1: World net electricity generation by fuel, 2012-40 (trillion kilowatt-hours), U.S. Energy Information Administration (EIA) [2016].

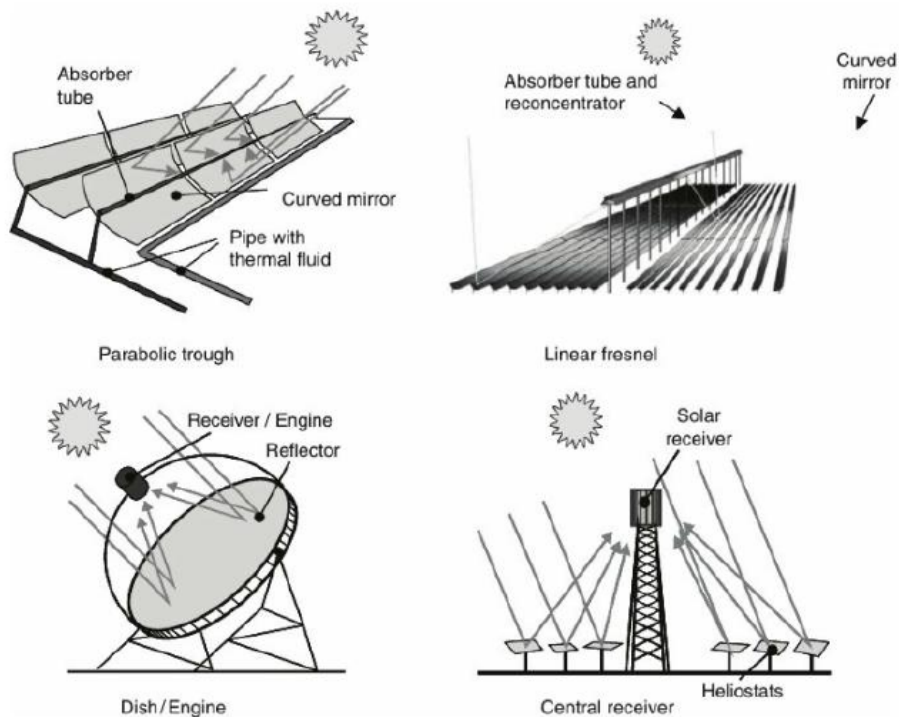


Figure 1.2: Types of concentrating solar power techniques, from Goswami and Kreith [2007].

The operation of CSP plants is challenging since the thermodynamic properties of the heated fluid are difficult to control in case, for instance, when the CSP

plant is only partly illuminated by the sun or when insolation is strongly variable over time ranges of a few minutes to a few hours. Also, large changes in radiation can lead to damages of the collectors. The fuel of solar power plants is direct normal irradiance (DNI). The main source of its spatio-temporal variability is cloudiness due to its intrinsic spatio-temporal inhomogeneity and to the fact that already thin clouds can reduce DNI to unusable levels for CSP. CSP is shut down when $\text{DNI} < 200 \text{ W/m}^2$, which corresponds to a vertical optical thickness of less than 2. In the clear-sky case especially aerosols contribute to the attenuation of DNI by a factor of 20 – 30% [Gueymard, 2012b, Nikitidou et al., 2014, Henzing et al., 2004, Jacovides et al., 2000] and, to a lesser extent, water vapour and ozone [Gueymard, 2012a].

Thus, the knowledge and the prediction of atmospheric properties for the derivation of DNI is essential for the optimisation of the CSP operation strategy as for day-ahead and intra-day wholesale spot markets the hourly electricity production must be announced to the market operator and deviations from the production schedule may lead to financial penalties. This production schedule may be revised according to intra-day trading rules, which impose additional constraints for the required forecasts, e.g. gate closure times.

The persistence approach is the simplest forecast model and works well for periods of low cloud variability and obviously for clear-sky cases. Of course, the accuracy of persistence models is reduced substantially when the variability increases. Therefore, other methods are used based on data from various sources depending on the forecast horizon. Kraas et al. [2013] show the economic merits of a forecasting system for day-ahead forecasts for concentrated solar power, which reduces penalties by 47.6% compared to a persistence model. More recently, Law et al. [2016] evaluated the benefit of using 1-h forecasts for the operation of CSP plants, thus achieving higher financial value and reliability.

For the optimized operation of CSP both technical and economic aspects apply as the main aim is to provide stable plant operations and a predictable electricity flow. The nowcasting of DNI helps the operator to fulfill this goal, e.g. if and when the start-up and shut-down of the sub-systems of the plant should take place. As the start-up phase of a power plant takes between 30-60 minutes, depending on the used technology, the expected solar gain for the next hours must be considered and the operators have to decide if the amount of DNI is sufficient for a profitable operation of the station. Additionally, a reliable nowcasting of DNI enables an optimisation of storage and fossil fuel use as well as a compensation of fluctuations in the power output. For this, forecasts up to several hours are required with a temporal resolution of 10 min and a spatial resolution of the solar field area average (1-3 km) [Hirsch, 2014]. Regarding the technical aspect of optimized operation heterogeneous distribution of DNI over the solar field, which results in efficiency losses, must be considered. For that purpose, a spatial resolution of 30-60 m and a short term resolution of single minutes are required [Hirsch, 2014].

For the prediction of solar irradiance one or two days ahead numerical weather

prediction (NWP) models are used, which provide better results if combined with artificial neural networks (ANNs) [Marquez and Coimbra, 2011, Gonzalez et al., 2010] or radiative transfer simulations [Casado-Rubio et al., 2017]. However, for short-term forecasts up to 6 h NWP models are not well suited and satellite-based methods come into play: Perez et al. [2010] and Lorenz et al. [2012] show that below a forecast horizon of 4-6 h forecasting methods of NWP models have a lower accuracy compared to satellite-based algorithms (e.g. Cros et al. [2014], Hammer et al. [1999]). Geostationary satellites usually provide multispectral images with a temporal resolution between 5 and 30 min and a spatial resolution in the order of kilometers that can be used for determining and predicting the motion of clouds and their properties. Several approaches deal with the detection and tracking of cloud patterns with satellite data - a challenging task due to the non-linearity in atmospheric motion. They range from standard pattern recognition techniques [Bolliger et al., 2003, Schmetz et al., 1993], where cloud patterns are tracked, to multichannel correlation-relaxation labeling [Evans, 2006, Wu, 1995, Wu et al., 1997], which determines the most appropriate motion vectors from several channels. With the predicted cloud properties, the irradiance at the ground can be determined. Several approaches deal with the calculation of DNI with satellite data, e.g. the HELIOSAT methods [Cano et al., 1986, Diabate et al., 1988, Beyer et al., 1996, Rigollier et al., 2004, Qu et al., 2016] or SICCS [Greuell et al., 2013]. The temporal and spatial resolution of satellite images are inappropriate for accurate intra-hour forecasts of clouds and solar irradiance at particular (power plant) sites. This lack can be overcome by using local high-frequency image-capturing devices, such as sky imagers. For the forecast of solar irradiance with sky imagers methods are used which derive cloud motion vectors (CMV) from two consecutive images. Examples for the derivation of CMVs are optical flow methods [Schmidt et al., 2016, West et al., 2014, Wood-Bradley et al., 2012], cross-correlation [Chow et al., 2011] or particle image velocimetry (PIV) [Marquez and Coimbra, 2013, Chu et al., 2013, 2014]. More recently, a four-camera system called WobaS [Kuhn et al., 2017] has been installed at three solar power plants determining and predicting DNI maps. Next to the usage of sky imagers, forecasts of solar irradiance are performed by means of pyranometers [Bosch et al., 2012] or by determining cloud shadow speed with luminance sensors [Fung et al., 2014].

For an optimized operation of solar power plants, a continuous forecast over all temporal and spatial scales is necessary as (day-ahead and) intra-day hourly electricity production must be announced to the market operator. For this, ground-based, satellite-based and NWP-based forecasts methods have to be combined. But this is a challenging task due to their varying temporal and spatial scales. Lorenz et al. [2012] and Mathiesen et al. [2013] show that for the forecast of solar irradiance a combination of satellite-based and NWP-based methods outperform the forecasts of the single methods for forecast lead times of several hours. More recently, Müller and Remund [2016] developed a method for the nowcasting of DNI based on geostationary satellite data and wind velocities from a mesoscale

numerical weather model. Also, hybrid systems using satellite-based and ground-based methods, e.g. measurements of global horizontal irradiance [Marquez et al., 2013], are able to perform more accurate forecasts as the single methods up to several hours. A forecast of solar irradiance by combining satellite and sky imagers could provide a continuous forecast on the minute to several hours scale before weather model information becomes useful.

In this work the following hypothesis will be evaluated:

It is possible to provide seamless and accurate forecasts of clouds and surface DNI for the next minutes up to several hours with high spatial resolution for the improved operation of CSP plants.

Therefore, it is not only important to predict the position of the clouds, i.e. the location of DNI attenuation, but also their optical properties, i.e. optical thickness, as thin clouds may reduce DNI to a still usable level. For this a novel nowcasting algorithm based on satellite data from the SEVIRI imager aboard Meteosat Second Generation (MSG) has been developed. With its high repetition rate of 15 min, its spatial sampling distance of 3 km and the availability of 12 spectral channels, this sensor is very well suited for the determination and forecast of the derived cloud optical properties to be used to calculate DNI since clouds are highly variable in space and time.

In order to assess the hypothesis, several questions have to be answered. The first question examined in this thesis is:

- 1) Can low resolution MSG/SEVIRI data be used for the accurate nowcasting of warm and cold cloud properties and surface DNI at the 3-5 km scale?

With the high resolution visible (HRV) channel of MSG/SEVIRI optical properties and DNI can be detected and forecasted more accurately. Therefore, a novel method for a synergistic exploitation of the high and low resolution MSG/SEVIRI data has been developed. In this context, a second question is investigated:

- 2) To what extent does the high resolution visible channel of MSG/SEVIRI help enhancing the spatial resolution of the nowcasting of warm and cold cloud properties and surface DNI to the 1-2 km scale?

The spatial resolution could be enhanced once more by a collocation of all-sky and MSG/SEVIRI images in order to combine the high spatial resolution of the all-sky imagers with the large spatial coverage of the satellite. Thereby, the following question arises:

- 3) Is there a promising approach to get a reasonable forecast of surface DNI by combining satellite and camera data?

The answers to these questions will be given in this thesis, which is structured as follows.

Sect. 2 gives an overview of the physical background, i.e. radiative transport, cloud physics and remote sensing as well as a short summary of forecast terminology in the context of DNI nowcasting.

Sect. 3 introduces the used instrumentation and methods, i.e. the optical flow algorithm (Sect. 3.4), which is the basis for the nowcasting algorithm. Also, two satellite-based nowcasting methods are presented, which are used for comparison (Sect. 3.5).

The forecast algorithm is described in Sect. 4 and focuses on forecast lead times from 5 to 120 min. By means of the optical flow algorithm atmospheric motion vectors for every pixel instead for cloud patterns can be determined. The starting point is represented by the optical thickness of clouds that are first split up into two (vertically overlapping) layers in order to take care of different velocities of upper level and low level clouds (Sect. 4.1). To reduce the turbulent character of the atmospheric motion field on small scales, rendering long range forecasts impossible, cloud subsets are defined as rigid objects that move with time. Convection initiation cannot be forecasted adequately this way due to its rapid development as well as its small spatial (few 100 m) and temporal (minutes) resolution. However, nowcasting methods are well suited to forecast the development of convective clouds after initiation using near real-time information from radars, e.g. CONRAD [Lang, 2001] and TRT [Hering et al., 2004], and passive imagers, e.g. Zinner et al. [2008] or Feidas and Cartalis [2005], or a combination of both [Henken et al., 2011]. Our approach considers dissipating convective clouds where extended anvils are produced that can live for many hours and have an important impact on DNI.

DNI is eventually computed from the forecast of the optical thickness of the atmosphere with ancillary data (Sect. 4.2). A validation against MSG/SEVIRI observations (Sect. 4.3) as well as ground measurements and two other satellite-based forecast methods (Sect. 4.5) is shown, together with case studies (Sect. 4.4) illustrating the benefits and limitations of the forecast algorithm. Sect. 4.1- 4.3 have been published in Sirch et al. [2017].

In order to examine the gain in forecast accuracy of clouds and DNI by enhancing the spatial resolution a synergistic exploitation of the high and low resolution MSG/SEVIRI data is presented (Sect. 5.1, 5.2). Together with radiative transfer calculations cloud mask and cloud optical properties are derived. The forecast results of this method are compared to low resolution MSG/SEVIRI forecasts by means of case studies (Sect. 5.4) and ground measurements of DNI (Sect. 5.5).

The spatial resolution is enhanced once more by the use of all-sky imagers. In Sect. 6.1 a novel approach for the collocation of all-sky and MSG/SEVIRI images is presented. This synergistic use of camera and satellite data enables a continu-

ous forecast for the next minutes up to several hours (Sect. 6.2). The benefits and limitations of this method are shown by means of three case studies (Sect. 6.3).

Chapter 2

Theoretical background

2.1 Radiative transfer quantities

Radiative transfer describes the propagation of electromagnetic radiation through a medium, for example the atmosphere. Electromagnetic radiation travels in wave form at the speed of light $c = 299792458 \text{ m/s}$. One particular feature is the wave-particle duality as radiation can be explained by wave mechanics (e.g. scattering) and quantum mechanics (e.g. absorption). Electromagnetic waves are characterised by their wavelength $\lambda [m]$:

$$\lambda = \frac{c}{\nu}, \quad (2.1)$$

where $\nu [\frac{1}{s}]$ represents the frequency.

The radiant energy $Q [J]$ transported by electromagnetic waves per unit time is described as the radiant power $\Phi [W]$:

$$\Phi = \frac{dQ}{dt}. \quad (2.2)$$

The radiant flux of energy through a unit area dA with a specified orientation is defined as the irradiance $E [W/m^2]$:

$$E = \frac{d^2Q}{dAdt}. \quad (2.3)$$

Due to the directional dependency incoming radiant quantities are considered in a differential solid angle element $d\Omega = \sin\vartheta d\vartheta d\varphi$ [sr] in polar coordinates with the azimuth angle φ (Fig. 2.1). The zenith angle ϑ is the angle between the

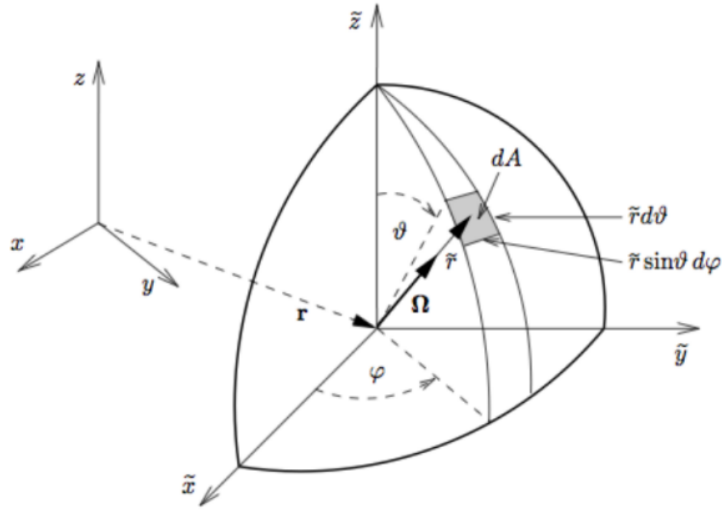


Figure 2.1: Local spherical $(\tilde{r}, \varphi, \vartheta)$ -coordinate system, where \tilde{r} is the radial distance from the origin located at \vec{r} , and the direction $\vec{\Omega}$, taken from Zdunkowski et al. [2007].

direction $\vec{\Omega}$ of the incoming radiation and the surface normal \vec{n} at a location \vec{r} (Fig. 2.2). The monochromatic radiance $L = L(\vec{r}, \vec{\Omega}, t)$ [$W/(m^2 sr)$] at a specific wavelength λ is defined as the radiant energy Q through the differential area element dA during a time dt through the angle element $d\Omega$:

$$L = \frac{dQ}{dA \cos \vartheta d\Omega dt}. \quad (2.4)$$

By integrating the normal component of L over the entire hemispheric solid angle [Liou, 2002] the irradiance F over the hemisphere can be calculated:

$$F = \int_0^{2\pi} \int_0^{\pi/2} L \cos \vartheta \sin \vartheta d\vartheta d\varphi. \quad (2.5)$$

2.2 Interaction of radiation with matter

The sources of the attenuation of radiation in the atmosphere are absorption and scattering by gas molecules, aerosols and clouds. It is proportional to the intensity of the incoming radiation, the concentration of gases/particles and their effectiveness to absorb or scatter.

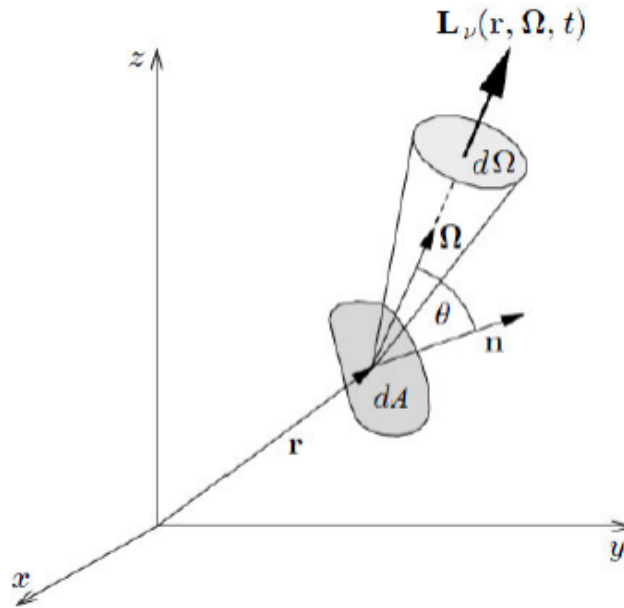


Figure 2.2: Radiant energy transmitted through the infinitesimal area element dA with the surface normal \vec{n} at location \vec{r} into the solid angle element $d\Omega$ along the direction $\vec{\Omega}$ of the photons, adapted from Zdunkowski et al. [2007].

2.2.1 Absorption

The intensity of incoming radiation is reduced by absorption in the atmosphere by transforming radiation into internal energy of molecules, thus changing the state of the molecule. The absorption cross-section $\sigma_{\text{abs}} [cm^2]$ determines the probability of absorption and the intensity of absorption is dependent of the concentration of the absorbers referred to as the volume density $\rho_{\text{abs}} [cm^{-3}]$. Thus, the absorption coefficient $k_{\text{abs}} [m^{-1}]$ is calculated with:

$$k_{\text{abs}} = \rho_{\text{abs}} \sigma_{\text{abs}}. \quad (2.6)$$

2.2.2 Scattering

Next to absorption, scattering contributes to the attenuation of incoming solar radiation in the atmosphere. Through the interaction with molecules or particles the direction of the radiation is changed. In the atmosphere, the particles responsible for scattering range in size from gas molecules ($\sim 10^{-4} \mu m$) to aerosols ($\sim 1 \mu m$), water droplets ($\sim 10 \mu m$), ice crystals ($\sim 100 \mu m$), large raindrops and hail ($\sim 1 cm$). Scattering occurs at all wavelengths and depends on the ratio of particle size and wavelength, which is expressed by the dimensionless size

parameter x :

$$x = \frac{2r\pi}{\lambda}, \quad (2.7)$$

with the radius of a spherical scattering particle r and the wavelength λ of the incident electromagnetic wave.

The distribution of the scattered radiation depends on shape, size and refractive index of the scattering particle and the dimensionless scattering phase function P is used to describe this distribution. $P = P(\vec{\Omega}', \vec{\Omega})$ is a measure for the probability of electromagnetic radiation with the incident direction $\vec{\Omega}'$ being scattered into the direction $\vec{\Omega}$ [Zdunkowski et al., 2007] and is normalised according to unity [Liou, 2002]:

$$\frac{1}{4\pi} \int_{4\pi} P(\vec{\Omega}', \vec{\Omega}) d\Omega = 1. \quad (2.8)$$

The angle Θ between the incident direction $\vec{\Omega}'$ and scattered direction $\vec{\Omega}$ is given by $\cos\Theta = \vec{\Omega}' \cdot \vec{\Omega}$ [Thomas and Stamnes, 1999]. Thus, scattering is rotationally symmetric about the direction of incidence for homogeneous spherical particles. The term forward scattering is used in case of $\Theta < \pi/2$ and backward scattering in case of $\Theta > \pi/2$, respectively.

With the scattering cross section $\sigma_{\text{sca}} [cm^2]$, which describes the probability of radiation being scattered by the particle, the scattering coefficient $k_{\text{sca}} [m^{-1}]$ can be computed by

$$k_{\text{sca}} = \rho_{\text{sca}} \sigma_{\text{sca}}. \quad (2.9)$$

Rayleigh scattering

For homogeneous, isotropic, spherical molecules/particles much smaller in comparison with the wavelength λ of the incident radiation, i.e. $x \ll 1$, scattering is described according to the Rayleigh theory [Strutt, 1871]. Forward and backward scattering are equal and the scattered intensity of the radiation is proportional to λ^{-4} . The phase function for Rayleigh scattering is

$$P(\cos\Theta) = \frac{3}{4}(1 + \cos^2\Theta). \quad (2.10)$$

Fig. 2.3 illustrates the scattering patterns for spherical particles of size $10^{-4} \mu m$, $0.1 \mu m$, and $1 \mu m$ illuminated by visible light with a wavelength of $0.5 \mu m$. Small

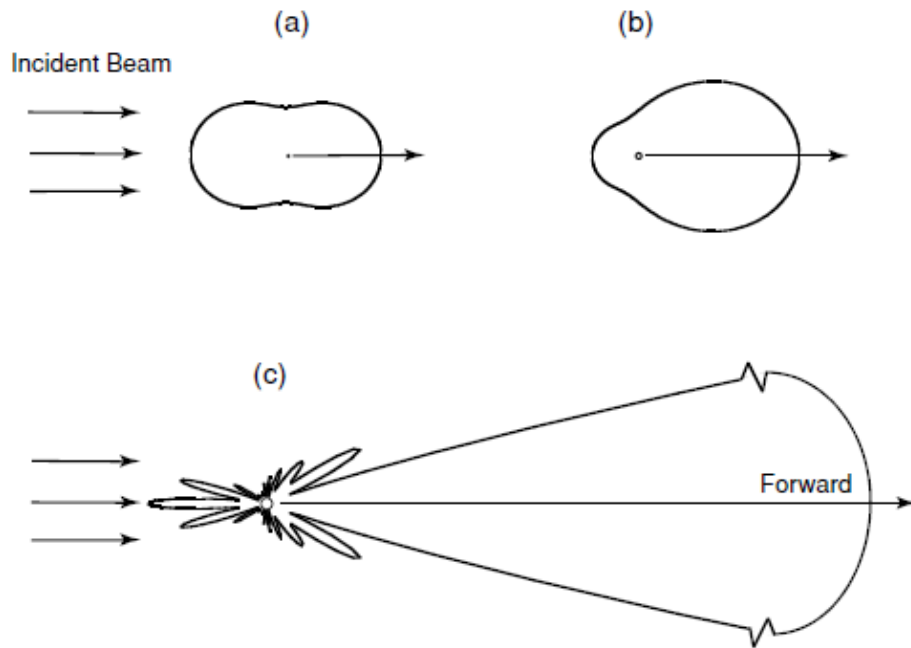


Figure 2.3: Demonstrative angular patterns of the scattered intensity from spherical particles of three sizes illuminated by the visible light of $0.5 \mu m$: (a) $10^{-4} \mu m$, (b) $0.1 \mu m$, and (c) $1 \mu m$. The forward scattering pattern for the $1 \mu m$ aerosol is extremely large and is scaled for presentation purposes, adapted from Liou [2002].

particles, i.e. $x \ll 1$, tend to scatter light equally in the forward and backward directions (Fig. 2.3 a).

Mie scattering

For particle sizes comparable to the wavelength, i.e. $x \geq 1$, the theory of Mie scattering applies [Mie, 1908]. It is based on the mathematical solution of Maxwell's equations using proper boundary conditions and describes the distribution of the scattered radiance $L(\Theta)$ for isotropic, homogeneous, spherical particles in dependence of the incoming radiance L_0 and the phase function $P(\Theta)$:

$$L(\Theta) = L_0 \left(\frac{\sigma_{\text{sca}}}{R^2} \right) \frac{P(\Theta)}{4\pi} \quad (2.11)$$

where R is the distance from the scatterer. With increasing particle size the intensity of forward scattering is rising. This effect can be seen in Fig. 2.3 b,c showing angular patterns of scatter intensity for particles of size $0.1 \mu m$ and $1 \mu m$. Note the with particle size increasing peak in the forward direction as well as the strongly asymmetric pattern for large particles ($1 \mu m$) compared to smaller

ones ($0.1 \mu m$).

2.2.3 Atmospheric extinction

The extinction coefficient k_{ext} [m^{-1}] is used to quantify the degree of attenuation of radiation:

$$k_{\text{ext}} = k_{\text{abs}} + k_{\text{sca}}, \quad (2.12)$$

with k_{abs} [m^{-1}] as the absorption coefficient and k_{sca} [m^{-1}] as the scattering coefficient. A measure for the ratio of absorption to scattering is the single scattering albedo ω_0 :

$$\omega_0 = \frac{k_{\text{sca}}}{k_{\text{ext}}}. \quad (2.13)$$

2.2.4 Lambert-Beer's law

The Lambert-Beer law describes the attenuation of electromagnetic radiation at a specific wavelength λ in a medium with the extinction coefficient $k_{\text{ext},\lambda}$ along a path from s_1 to s_2 :

$$L_\lambda(s_2) = L_\lambda(s_1) \exp\left[-\int_{s_1}^{s_2} k_{\text{ext},\lambda}(s) ds\right]. \quad (2.14)$$

The term in the exponent is defined as the optical thickness τ_λ at a specific wavelength λ :

$$\tau_\lambda(s_1, s_2) = \int_{s_1}^{s_2} k_{\text{ext},\lambda}(s) ds. \quad (2.15)$$

With the optical thickness the transmission T_λ can be calculated, which is a measure for the transmissivity of radiation through a medium:

$$T_\lambda(s_1, s_2) = e^{-\tau_\lambda(s_1, s_2)}. \quad (2.16)$$

2.2.5 Emission

In emission, a molecule undergoes a transition to a lower level of internal energy by releasing a photon. A "blackbody" (idealized physical body) absorbs all incoming radiation and re-emits in a characteristic, continuous spectrum that depends on temperature alone. According to Planck's law [Planck, 1901] the emitted spectral radiance $B_\lambda(T)$ [$W/m^2sr\mu m$] is related to the temperature T via the Planck function:

$$B_\lambda(T) = \frac{2hc^2}{\lambda^5} \frac{1}{\exp\left(\frac{hc}{k_B\lambda T}\right) - 1}, \quad (2.17)$$

with the Boltzmann constant $k_B = 1.381 * 10^{-23} JK^{-1}$ and the Planck constant $h = 6.62606957 * 10^{-34} Js$. The inversion of the Planck function gives the monochromatic brightness temperature T_b :

$$T_b = \frac{2hc}{k_B\lambda} \left(\ln \left(\frac{2hc^2}{\lambda^5 L_m} \right) + 1 \right), \quad (2.18)$$

T_B is the temperature a blackbody should have to produce the measured spectral radiance L_m at a wavelength λ and is an important quantity in passive remote sensing as it allows to translate the radiances measured by spaceborne radiometers into brightness temperatures.

The emissivity ϵ_λ describes the emission capability of a real body compared to a blackbody with the same temperature. According to Kirchhoff's law the relationship between absorptivity α_λ and emissivity ϵ_λ can be expressed as:

$$\alpha_\lambda = \epsilon_\lambda. \quad (2.19)$$

2.3 Radiative transfer equation

The spatial and temporal evolution of electromagnetic radiation, when passing through a small volume element of length ds , is described by the radiative transfer equation (RTE) [Chandrasekhar, 1950], a linear integro-differential equation for the radiance L :

$$\frac{dL}{k_{\text{ext}} * ds} = -L + \frac{\omega_0}{4\pi} \int_0^\pi \int_0^{2\pi} P(\Omega, \Omega') L(\Omega') d\Omega' + (1 - \omega_0) B_\lambda(T) \quad (2.20)$$

A horizontally homogeneous atmosphere is approximated, where the atmospheric

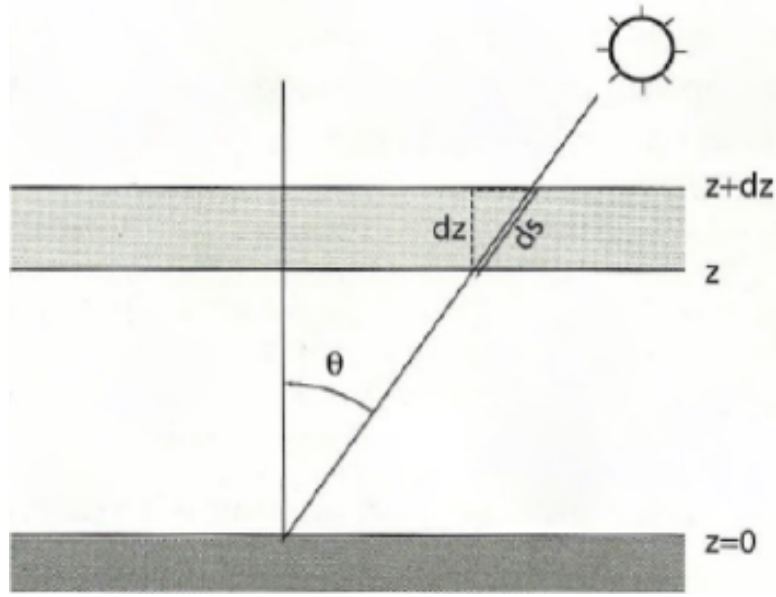


Figure 2.4: Relationship between slant path ds and vertical path dz of a plane-parallel atmosphere [Petty, 2006].

parameters are assumed to be functions of height only while horizontal variations are neglected. This plane-parallel approximation enables the determination of the atmospheric parameters in dependence of the height z (Fig. 2.4), whereby the path length element ds is computed as:

$$ds = \frac{dz}{\mu}, \text{ with } \mu = \cos\theta. \quad (2.21)$$

Upward and downward directed radiance is specified by $\mu > 0$ and $\mu < 0$, respectively. This plane-parallel assumption represents a good approximation of the atmosphere in many cases. Exceptions are radiative transfer calculations in case of solar positions near the horizon or finite clouds located over a heterogeneously reflecting ground. The first term in Eq. 2.20 describes the removal of radiation by scattering and absorption according to the Lambert-Beer law. The second and third term have a positive contribution, characterising the scattering and the emission in the path, respectively. Ω' indicates the incident direction of radiation being scattered into the direction Ω and $B_\lambda(T)$ (Sect. 2.2.5) denotes the intensity of radiation emitted by a black body of temperature T and thus quantifies the thermal source.

The radiative transfer equation can be expressed in dependence of the optical thickness $d\tau = k_{\text{ext}} * dz$ as:

$$\mu \frac{dL}{d\tau} = L - \frac{\omega_0}{4\pi} \int_0^\pi \int_0^{2\pi} P(\Omega, \Omega') L(\Omega') d\Omega' - (1 - \omega_0) B_\lambda(T). \quad (2.22)$$

Note the sign change compared to Eq. 2.20 due to replacing $\mu < 0$ (downward directed irradiance) by $-\mu$ ($\mu > 0$). The radiance L can be separated into the direct part L_{dir} (no interaction with matter in the atmosphere) and the diffuse part L_{dif} (interaction with matter in the atmosphere). The attenuation of the direct beam along its way through the layer is calculated according to Lambert-Beer's law (Sect. 2.2.4):

$$L_{\text{dir}}(\tau) = L_{\text{dir}}(0)e^{-\tau/\mu}. \quad (2.23)$$

2.4 Cloud properties

Clouds consist of liquid droplets and/or ice particles. The optical properties of liquid clouds are provided by the Mie theory, whereby the determination of the optical properties for ice particles is more complex due to their various shapes. For a typical size distribution of water droplets the optical properties of water clouds can be described by the effective radius r_{eff} [Hansen and Travis, 1974]:

$$r_{\text{eff}} = \frac{\int_0^\infty n(r)r^3 dr}{\int_0^\infty n(r)r^2 dr}, \quad (2.24)$$

with the droplet size distribution $n(r)$ and the droplet radius r . $n(r)dr$ describes the number of droplets per unit volume in the radius range $[r, r + dr]$. The reflected and transmitted radiation is dependent on the effective radius, whereas the detailed distribution of droplet sizes is of minor influence. For spherical droplets the liquid water content LWC is defined as the mass of cloud droplets per unit volume:

$$\text{LWC} = \frac{4}{3}\pi\rho_w \int_0^\infty r^3 n(r) dr, \quad (2.25)$$

with the density of water ρ_w .

Ice crystals are much more complicated than spherical water droplets with respect to their scattering and radiative properties. Schumann et al. [2011] defined a mean effective ice crystal radius r_{eff} to represent the ice crystal size distribution:

$$r_{\text{eff}} = \frac{3 \sum_i V_P(i)n_P(i)\Delta D_i}{4 \sum_i A_P(i)n_P(i)\Delta D_i} \quad (2.26)$$

where V_P and A_P are the mean particle volume and mean particle projected cross-sectional area for the size intervals D of width ΔD_i . The ice water content IWC for a given ice crystal size distribution is defined by

$$\text{IWC} = \rho_i \int V_P(D)n_P(D)dD, \quad (2.27)$$

with the density of ice ρ_i .

2.5 Aerosols

Aerosols are defined as a mixture of solid or liquid particles in the atmosphere. The interaction of aerosols with radiation in the atmosphere depends on aerosol type, size distribution and concentration. Typical aerosol types are continental, urban, maritime and biomass burning aerosol as well as dust and volcanic ash with particle sizes ranging from a few nm to more than $10 \mu\text{m}$.

Aerosols can strongly contribute to the attenuation of radiation in the atmosphere with a factor of 20–30% [Gueymard, 2012b, Nikitidou et al., 2014, Henzing et al., 2004, Jacovides et al., 2000]. One method to determine this reduction of radiation is by deriving Aerosol Optical Depth (AOD) as an input to Lambert-Beer’s law. AOD as well as other optical, microphysical and radiative properties for aerosols are available by the AERONET (AErosol RObotic NETwork) program (<http://aeronet.gsfc.nasa.gov/>), a federation of ground-based remote sensing aerosol networks.

2.6 Solar irradiance at TOA and the surface

The solar spectrum corresponds to the radiative spectrum of a blackbody with a temperature of 5900 K , roughly covering the range from 100 nm to $10 \mu\text{m}$ with a maximum at 480 nm (Fig. 2.5). The intensity of total solar radiation incident on top of the atmosphere is referred to as the solar constant E_0 . The International Astronomical Union (IAU) 2015 resolution B3 recommends the use of the solar constant with a value of $1361 \pm 0.5 \text{ W/m}^2$ [Prsa et al., 2016].

The solar irradiance at the surface is reduced due to absorption by air molecules and particles in the atmosphere. Fig. 2.5 shows the solar spectrum at sea level as well as the absorption bands of the gases (oxygen, ozone, water vapor and carbon dioxide). Next to gases also scattering by aerosols and clouds can reduce the solar irradiance at the surface.

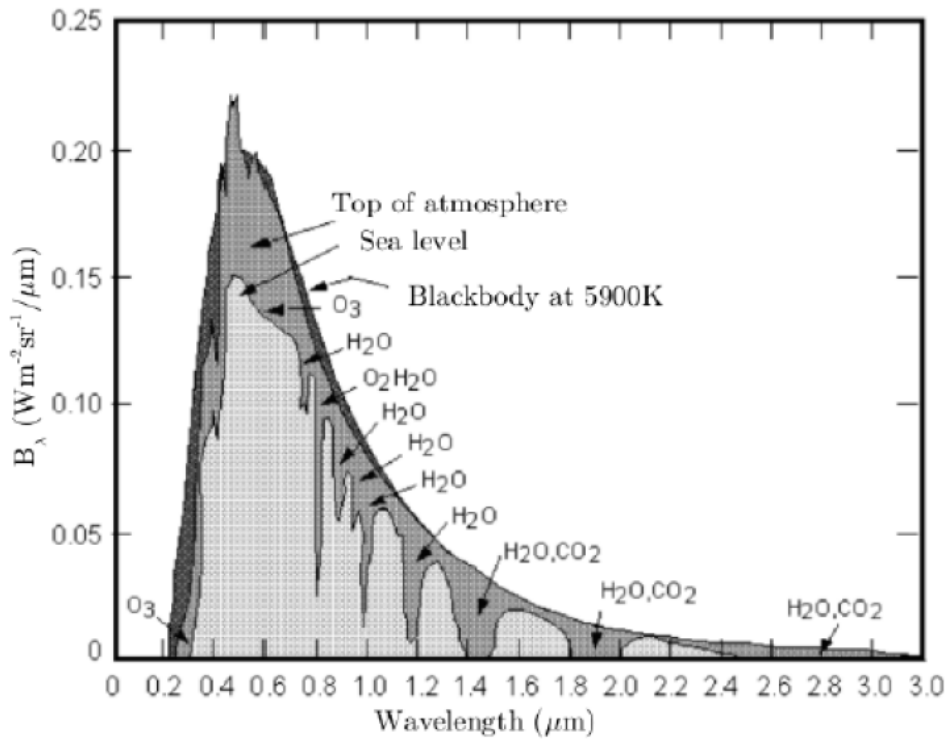


Figure 2.5: Solar spectrum at top of the atmosphere and at sea level compared to the black body spectrum calculated with the Planck function B_λ for $T = 5900K$ [Wallace and Hobbs, 1977].

2.7 Direct Normal Irradiance at the surface

According to the ISO-9488 standard [ISO-9488, 1999] Direct Normal Irradiance (DNI) is defined as the quotient of the radiant flux on a given plane receiver surface received from a small solid angle centred on the sun's disk to the area of that surface, which is perpendicular to the axis of the solid angle. Diffuse Horizontal Irradiance (DHI) is defined as the irradiance of diffuse solar radiation on a given horizontal plane receiver surface. The total solar irradiance, i.e. the sum of DNI and GHI, on a horizontal surface is called global horizontal irradiance (GHI).

The DNI used in this work considers only photons coming from the sun that do not interact with the atmosphere (see the “strict definition” of DNI for numerical modeling of radiative transfer in Blanc et al. [2014]). In particular, no circumsolar radiation, the diffuse part of the radiation coming from the circumsolar region close to the solar disk, is taken into account.

By integrating the solar constant E_0 and the optical thickness $\tau(\lambda)$ of the atmosphere (Eq. 2.23) over all wavelengths the DNI is calculated according to Lambert-Beer's law:

$$\text{DNI} = \int E_0(\lambda) * \exp(-\tau(\lambda) / \cos(\vartheta_0)) d\lambda, \quad (2.28)$$

with the solar zenith angle ϑ_0 . Thus, the amount of DNI reaching the surface strongly depends on latitude, season and time of day as a larger solar zenith angle causes a longer path through the atmosphere. Fig. 2.6 illustrates this effect by

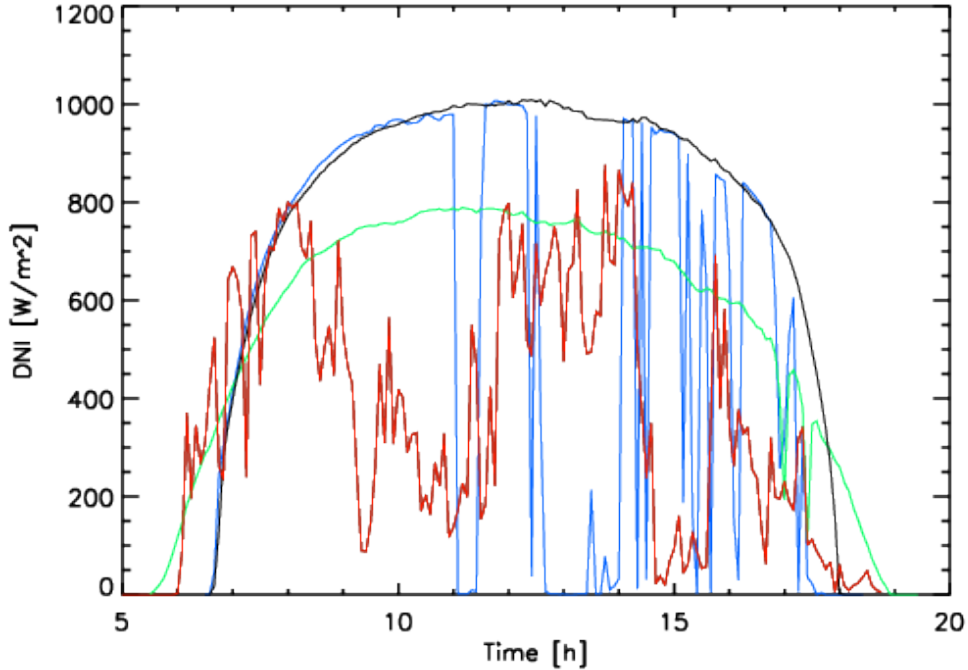


Figure 2.6: Diurnal cycle of DNI at the PSA for 8 March 2013 (black curve), 10 March 2013 (blue curve), 13 May 2013 (red curve) and 6 August 2013 (green curve).

showing the diurnal variation of DNI for four days at the Plataforma Solar de Almeria (PSA), the largest concentrating solar technology research development and test centre in Europe. The diurnal cycle for a clear-sky day, e.g. 8 March 2013 (black curve), shows only small variation of DNI due to the variability of aerosols or atmospheric gases, e.g. water vapor. One characteristic feature for a diurnal cycle of DNI is the steep increase/decrease at sunrise/sunset. On cloudy days the variability is very high and DNI can be attenuated completely in case of thick clouds, e.g. 10 March 2013 (blue curve), or reduced to a still usable level by thin cirrus clouds, e.g. 13 May 2013 (red curve). The effect of high aerosol load ($\tau_{aer,550nm} \cong 0.25$) is visible on 6 August 2013 (green curve), where DNI is reduced by over 20%.

As the definitions used for DNI nowcasting may differ from other fields of nowcasting a short summary of forecast terminology is given here with some typical examples. Nowcasting is typically understood as the forecast within the upcoming 6 hours. The frequency with which the predicted values are updated is called refresh rate, e.g. forecast start every 15 min, and the temporal resolution defines the length of the time interval between the predicted values - for a temporal resolution of 5 min the predicted values are given for forecasts of 5 min, 10 min, 15 min, etc. The forecast lead time is the time between the start of the forecast

and the occurrence of a forecasted value with the forecast horizon as the maximum forecast lead time, e.g. 6 hours.

DNI is the fuel for CSP plants, where the incoming DNI is concentrated by means of mirrors, heating a fluid (oil, water/steam or molten salt) and driving a heat engine. The used technologies are parabolic trough, solar power tower, Fresnel reflectors and dish Stirling. CSP capacities are highest in Spain and the USA, i.e. California, as well as in northern Africa, i.e. Morocco. The efficiency of CSP plants depends on the used technology and the temperature.

2.8 Passive remote sensing

Passive remote sensing is based on the theory of electromagnetic radiation. In order to retrieve information about the actual atmospheric condition from a measured radiative quantity the theory of radiative transfer needs to be applied. For satellite channels in the thermal infrared the observed radiances are transformed to equivalent brightness temperatures (Sect. 2.2.5), a quantity, whose interpretation is easier. For the solar channels the observed radiances are transformed to reflectivities, which are defined as the fraction of incoming radiation that is reflected in the atmosphere. In this spectral range most of the radiation is reflected on atmospheric constituents, i.e. on clouds. Due to the high reflectivity of thick clouds compared to the ground solar channels are often used for cloud detection. For the observation of the atmosphere with satellites the radiation in certain spectral ranges is determined. The observed spectral range depends on the application. In so-called window channels, spectral ranges with low absorption of the atmosphere, the whole atmospheric column as well as the ground can be examined. In order to observe the properties of particular atmospheric constituents, e.g. water vapor, ozone, carbon dioxide etc., selected spectral ranges are examined, where radiation interacts with these components.

Chapter 3

Instrumentation and Methods

This chapter provides a brief overview of the instruments and methods used in this work. After a short introduction to MSG/SEVIRI the algorithms for the detection of clouds and their optical cloud properties are described (Sect. 3.1). In Sect. 3.2) technical details and the calibration of all-sky imagers as well as their usage for cloud detection are presented. Pyrheliometers are described in Sect. 3.3 followed by a explanation of the optical flow method (Sect. 3.4), which is used for the forecast. In Sect. 3.5 two satellite based-nowcasting methods are presented, which are used for comparison. Sect. 3.1 and 3.4 are adapted from Sirch et al. [2017].

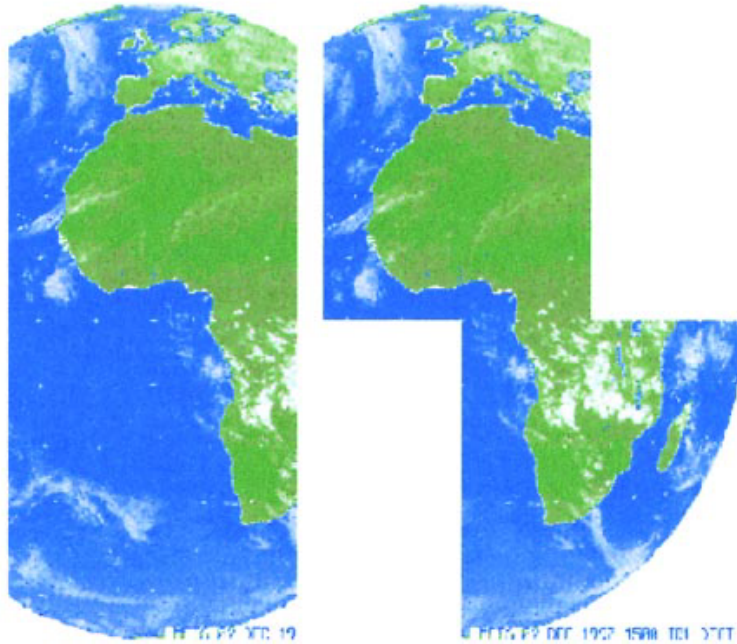
3.1 Cloud remote sensing with MSG/SEVIRI

3.1.1 Instrument

Meteosat Second Generation (MSG) is a series of European geostationary satellites operated by EUMETSAT, Darmstadt, Germany. Their primary mission is the observation of weather phenomena on the earth's full disk. For this purpose, the 12-channel passive imager SEVIRI (Spinning Enhanced Visible and Infrared Imager) has been developed. Table 3.1 shows its spectral channel characteristics consisting of two channels in the visible, one in the near infrared and eight in the infrared spectral range with a sampling distance of 3 km at the sub-satellite point [Schmetz et al., 2002], which increases for growing viewing zenith angle. SEVIRI covers the whole earth disk from 80°N to 80°S latitude and 80°W to 80°E longitude. Additionally to these low resolution channels, a broadband high resolution visible (HRV) channel is available, which covers half of the earth's full disk in the east-west direction with a higher spatial resolution of 1 km at the sub-satellite point (Fig. 3.1). The usual repetition rate of 15 min is reduced to

Table 3.1: SEVIRI spectral channels characteristics [Schmetz et al., 2002].

Channel	λ_{central}	λ_{min}	λ_{max}	Sampling Distance
	μm	μm	μm	km
VIS006	0.635	0.56	0.71	3
VIS008	0.81	0.74	0.88	3
IR_016	1.64	1.50	1.78	3
IR_039	3.90	3.48	4.36	3
WV_062	6.25	5.35	7.15	3
WV_073	7.35	6.85	7.85	3
IR_087	8.70	8.30	9.10	3
IR_097	9.66	9.38	9.94	3
IR_108	10.80	9.80	11.80	3
IR_120	12.00	11.00	13.00	3
IR_134	13.40	12.40	14.40	3
HRV	Broadband (about 0.4–1.1)			1

**Figure 3.1:** The HRV aboard MSG/SEVIRI covers only half of the earth in the E-W direction with $11\,136 \times 5568$ pixels; however, the area of imaging can be selected [Schmetz et al., 2002].

5 min in rapid-scan-mode for the upper third of the disk.

The geolocation and the inter-channel registration of MSG/SEVIRI is not exact so that the single pixels are not congruent for all channels, which could lead to

uncertainties when working with the LRES channels and the HRV. As a synergistic use of the high and low resolution data is examined in this work (Sect. 5) these uncertainties must be considered. With a method for image coregistration, Deneke and Roebeling [2010] were able to detect and correct for shifts of the HRES images relative to the LRES images, which is not limited to integer multiples of the pixel resolution. Fig. 3.2 shows histograms of the individual shift found, with a mean value of 0.06 ± 0.10 km in southward and 0.36 ± 0.11 km in eastward direction. These values indicate the coregistration accuracy of the satellite images is sufficient in most cases and it can thus be argued that the additional complexity of coregistering the images is not worth the extra effort. Therefore, no coregistering is applied in this work.

In order to reasonably compare the results derived in high and low resolution (see Sect. 5) the spatial response of the SEVIRI detectors [EUMETSAT, 2006] must be considered. Fig. 3.3 shows the point spread function (PSF) of the SEVIRI detectors, a commonly used quantity to characterize the spatial resolution of optical systems. A perfect step response shows a normalized spatial response of 1 up to a HRES and LRES sampling distance of 0.5 and 1.5 km, respectively (Fig. 3.3, grey). The actual PSF decreases with increasing distance to the pixel center with contributions to the spatial response up to a HRES and LRES distance of ~ 1.5 and ~ 4 km, respectively. Hence, contributions of surrounding pixels influence the observed reflectivities in each pixel.

3.1.2 Ice cloud detection (COCS)

For the detection of thin ice clouds, the "Cirrus Optical properties derived from CALIOP and SEVIRI during day and night" (COCS, Kox et al. [2014]) algorithm is used. It is a backpropagation neural network, which is trained with collocated products of the depolarisation-lidar CALIOP (Cloud-Aerosol Lidar with Orthogonal Polarization, Winker et al. [2009, 2010]) aboard the Cloud-Aerosol Lidar and Infrared Pathfinder Satellite Observations (CALIPSO) and brightness temperatures as well as brightness temperature differences of MSG/SEVIRI (see above). The COCS algorithm provides cloud coverage, optical thickness and cloud top height for ice clouds. In a validation study against airborne High Spectral Resolution Lidar measurements [Kox et al., 2014], COCS detected 80% of the cirrus clouds with optical thickness 0.2 and its detection efficiency increased for higher optical thicknesses. For optical thickness 0.1 COCS detected still 50% of the cirrus clouds observed by CALIPSO. The false alarm ratio amounted to 2.6% for all measured cirrus clouds. It is very robust for small optical thicknesses above 0.1 up to a maximum of 2.5. Clouds with larger optical thickness cannot be penetrated by CALIOP. COCS provides information only about the highest ice cloud layer. As COCS works with the thermal SEVIRI channels it can be applied during day and night.

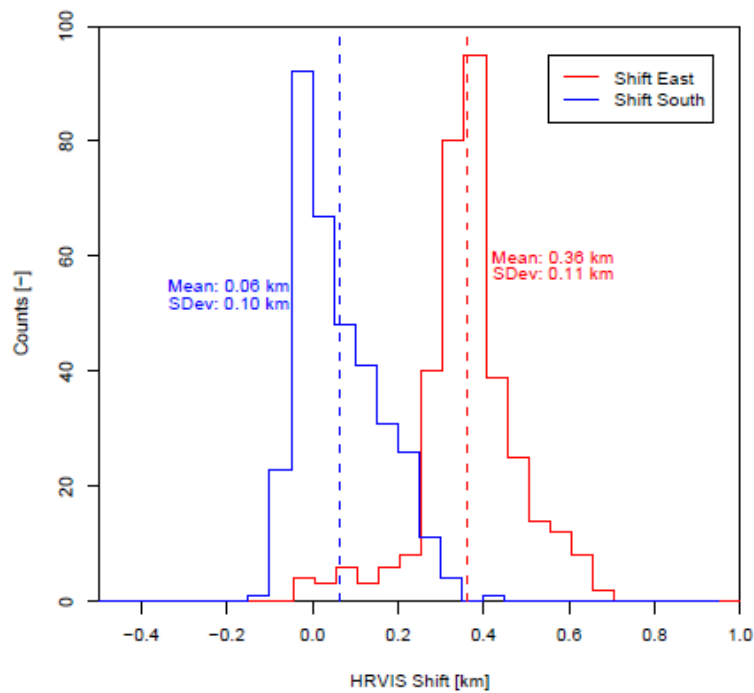


Figure 3.2: Histogram of the shifts of the HRV image relative to the 0.6 and 0.8 μm channel in Northern and Eastern direction, obtained for 345 Meteosat-9 scenes from 2008 [Deneke and Roebeling, 2010]. The shift of the images is expressed as distance at the nadir point of the satellite in kilometers (km).

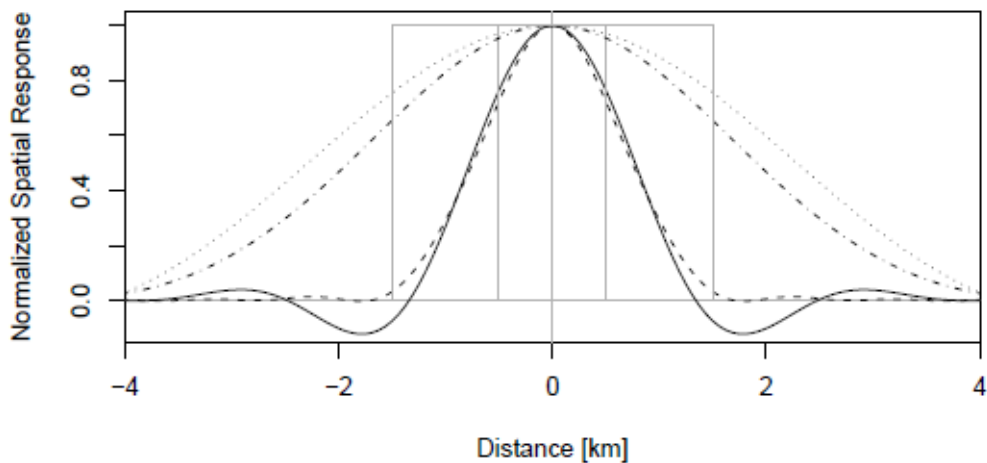


Figure 3.3: Point spread function (PSF) of the SEVIRI detectors of the LRES 0.6 and 0.8 μm channels and the HRES channel for Meteosat-9 in North-South (NS) and East-West (EW) directions, as a function of distance from the pixel center [Deneke and Roebeling, 2010]. The PSF has been reconstructed from the modulation transfer function by the inverse Fourier transform [EUMETSAT, 2006]. In grey, a perfect step response at LRES and HRES sampling resolution is also shown.

3.1.3 Water and ice cloud optical properties (APICS)

In addition to COCS, APICS ("Algorithm for the Physical Investigation of Clouds with SEVIRI", Bugliaro et al. [2011]) is applied for the detection of liquid water clouds and thick cirrus. The APICS cloud detection is based on Kriebel et al. [2003] and consists of two groups of threshold tests comprising reflectivity tests and spatial coherence tests applied to the solar SEVIRI channels. The first group detects a cloud if it is bright enough compared to the cloud-free reflectivity. The second is applied over sea and detects a cloud if the variability of the signal is higher than that of the cloud-free background (the sea surface reflectivity is supposed to be spatially homogeneous). A pixel is cloudy if at least one test gives a positive result.

The APICS algorithm provides cloud coverage and cloud optical thickness as well as effective radius. For this SEVIRI channels centred at 0.6 and 1.6 μm are used based on the method described by Nakajima and King [1990], Nakajima and Nakajima [1995]: in the first spectral range clouds mainly scatter radiation, while in the second channel clouds both absorb and scatter the incoming solar radiation. Since absorption is a function of effective radius while scattering depends mainly on optical thickness, a simultaneous retrieval of optical thickness and effective radius can be performed by minimizing the difference between measured and computed reflectivities. The look-up tables required for this application have been computed with the radiative transfer model libRadtran [Mayer and Kylling, 2005, Emde et al., 2016], which can be used to compute radiances, irradiances and actinic fluxes in the solar and terrestrial part of the spectrum. It includes a number of different radiative transfer equation solvers, e.g. DISORT [Stamnes et al., 2000] or twostr [Kylling et al., 1995], for varying geometries, spectral resolutions and different classes of atmospheric constituents depending on the application. The look-up tables for APICS have been calculated with libRadtran using a mid-latitude standard atmosphere [Anderson et al., 1986], a typical continental aerosol load (a rural type aerosol in the boundary layer, background aerosol above 2 km, spring-summer conditions and a visibility of 50 km, Shettle [1989]). Surface albedo is taken from the temporally appropriate white sky MODIS albedo product MCD43C1 [Schaaf et al., 2002]. For liquid water clouds, Mie cloud optical properties are assumed (spherical particles), while for ice clouds the parameterisation by Baum et al. [2005] is used (a mixture of ice cloud habits as a function of ice crystal size). The optical thickness derived this way ranges from 0 to 100 and refers to the entire atmospheric column.

3.1.4 Detection of convective clouds (Cb-TRAM)

For the detection of convective clouds, methods of the Cb-TRAM algorithm (Cumulonimbus TRacking And Monitoring, Zinner et al. [2008, 2013]) have been examined and exploited in this work. Cb-TRAM divides convection into three

stages:

- convection initiation (stage 1)
- rapid cooling (stage 2)
- mature thunderstorm cells (stage 3).

The detection of convection initiation (stage 1, Merk and Zinner [2013]) uses the evolution of reflectance in the HRV and cooling rate in the thermal spectral range. Stage 2 is issued for rapid vertical developments detectable in the water vapour channels at $6.2\ \mu\text{m}$. The detection of mature thunderstorm cells (stage 3) is limited to areas with a strong spatial roughness of the HRV, determined by the local standard deviation, combined with the brightness temperature difference of $6.2\ \mu\text{m}$ and $10.8\ \mu\text{m}$. This is only valid for daytime. During night the HRV is replaced by a similar measure for the brightness temperature at $6.2\ \mu\text{m}$ which is less successful at confining the detection to the active updraft, but includes large parts of the surrounding anvil and is independent of sunlight conditions, i.e. it produces smooth results in particular at sunrise, when the forecast is started. As these thinner clouds are most interesting for the derivation of DNI, the latter detection is used in the following (Sect 4.2.4).

3.2 Ground observation of clouds with all-sky imagers

Ground-based all-sky imagers, i.e. $170\text{-}180^\circ$ field-of-view cameras observing the upper hemisphere, are used for various purposes ranging from the determination of clear-sky intensity distribution [Chauvin et al., 2015] over cloud base height estimation [Kassianov et al., 2005] to cloud detection [Cazorla et al., 2015, Ghonima et al., 2012, Yang et al., 2015, 2016] and classification [Calbo and Sabburg, 2008, Heinle et al., 2010, Kazantzidis et al., 2012]. Another goal is the forecast of solar irradiance [Bernecker et al., 2014, Yang et al., 2014, Schmidt et al., 2016], e.g. DNI [Chu et al., 2013, Quesada-Ruiz et al., 2014]. In this study we use four all sky imagers at the sites DISS, METAS, LECE and KONTAS, which are located at the PSA. Fig. 3.4 shows the distribution of the cameras and additional instruments, e.g. pyrhelimeters.

3.2.1 Camera

The cameras installed at the PSA are of the type Mobotix Q24M, which consist of a high-resolution image sensor and a fisheye lens to capture a 180° -hemispheric

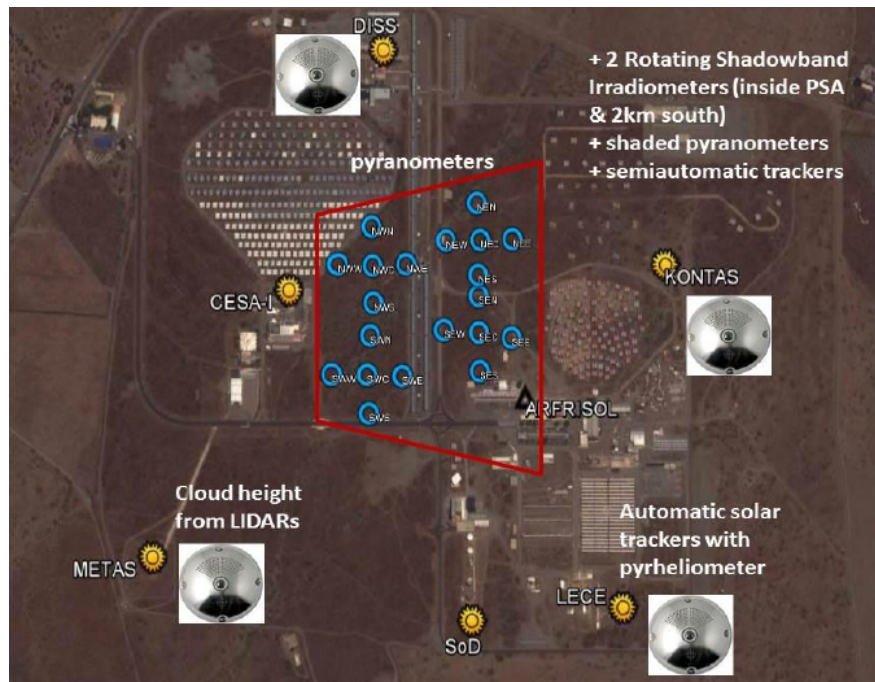


Figure 3.4: Distribution of the instrumentation at the PSA.

image of the sky [Mobotix, 2013]. With the exposure times (ET) of 320 ms, 640 ms and 1280 ms images are created every 30 seconds with an image size of 2048×1536 pixels and an angular resolution of $0.1\text{-}0.15^\circ$. The result is a fisheye image in JPEG format (Fig. 3.5, left), which is composed of the contributions of three colours: red (R), green (G) and blue (B). Fig. 3.6 shows the corresponding intensities of red (left), green (middle) and blue (right) with values ranging from 0 to 255. For clear sky the intensity of blue is highest due to the stronger scattering on air molecules, whereas the intensity of red is highest in case of clouds. These effects enable a detection of clouds with all-sky imagers. Due to the low costs - no radiometric calibration - the field of application for such kind of cameras is wide, ranging from the operation in surveillance activities to the use in research.

3.2.2 Calibration

In order to determine the internal parameters of each single camera an intrinsic calibration is performed characterising the focal plane, the focal and optical distortions. By the acquisition of several hemispherical images of checkerboard pattern on a flat support with different orientations and covering different parts of the field of view key points for the intrinsic calibration are derived. An example of checkerboard pattern is shown in Fig. 3.7 (left). With the OcamCalib toolbox [Scaramuzza et al., 2006, Scaramuzza, 2008] the intrinsic calibration of the camera is performed.

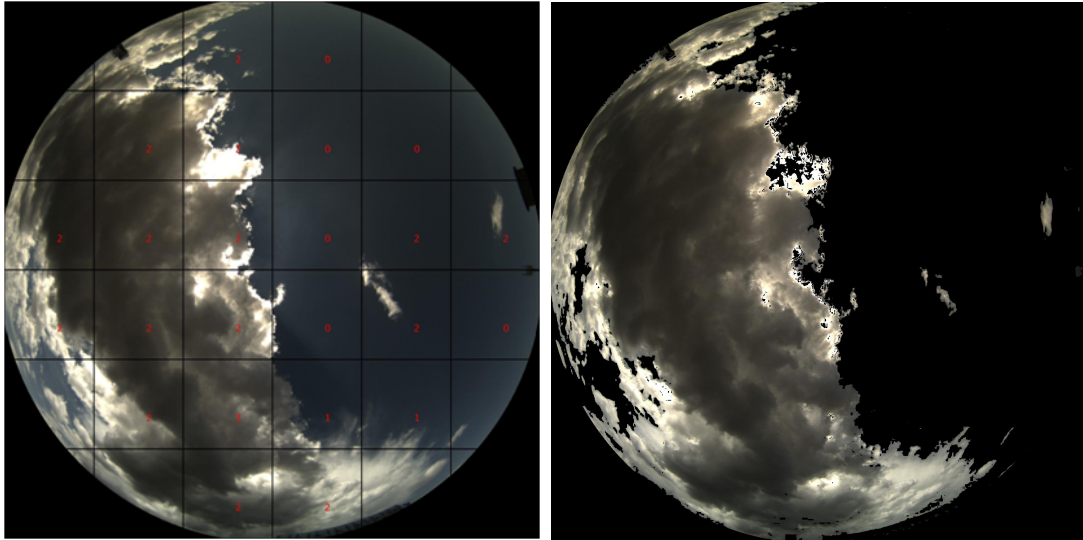


Figure 3.5: Fisheye image for 24 June 2014, 14:30 UTC, created by the sky imager at the KONTAS site at the PSA (left). The numbers in the grid elements denote the characterisation of cloudiness: 0 for no cloud, 1 for thin clouds and 2 for thick cloud. (right) The corresponding clear-sky mask for this scene (RGB values for the cloudy pixels).

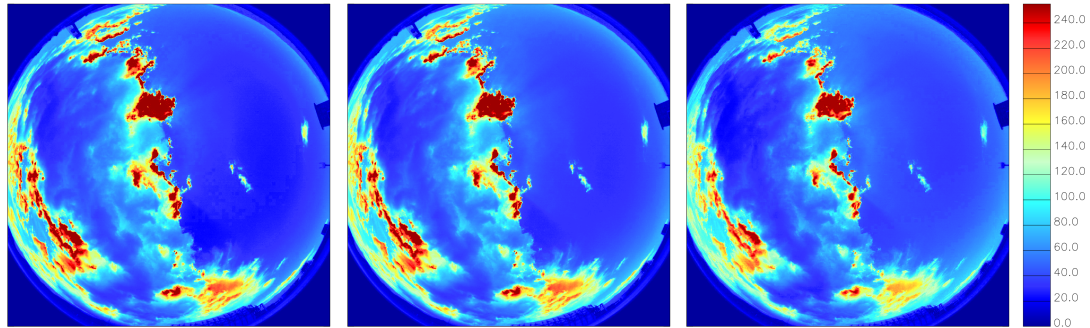


Figure 3.6: The intensity of red (left), green (middle) and blue (right) for 24 June 2014, 14:30 UTC, created by the sky imager at the KONTAS site.

In order to determine the orientation of the camera in the local reference frame an extrinsic calibration with automatic sun pixel detection is performed. For this, the theoretical angular position of the sun is compared to the centre of the sun detected in the time series of hemispherical images acquired during clear-sky days. Fig. 3.7 (right) shows the four cardinal directions for the camera at the Kontas site, where the centre of the cross indicates the zenith.

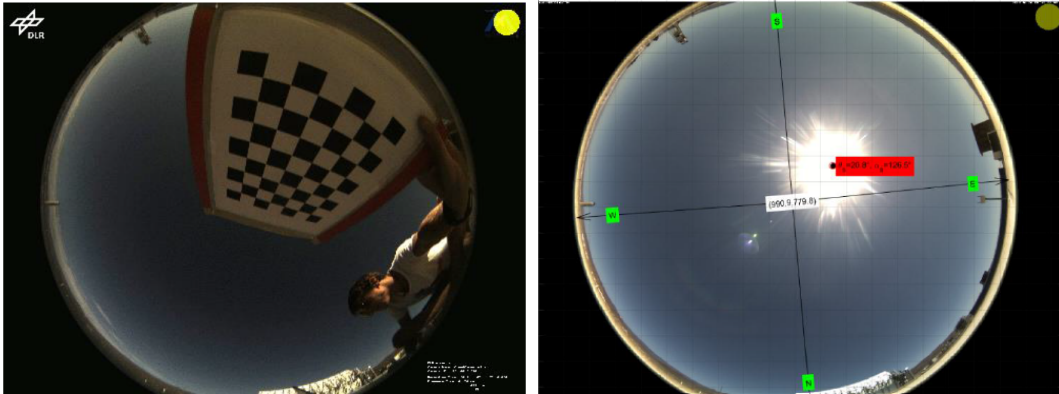


Figure 3.7: (left) Example of a hemispherical image of the checkerboard pattern used for the intrinsic calibration [Blanc et al., 2016] and (right) the representation of the four cardinal directions for the camera at the KONTAS site.

3.2.3 Cloud mask

In order to make forecasts with all-sky imagers a separation between cloudy and clear-sky pixels is necessary. For this, absolute values, differences and/or ratios of the red (R), green (G) and blue (B) intensities are examined. The determination of the cloud mask is done according to the method described in Kazantzidis et al. [2012] and shortly reported here.

In case the sun is not obstructed, images with an exposure time (ET) of 320 ms are used for the circumsolar region. Otherwise images with ET of 640 ms are applied. In special cases, i.e. a high saturation level of images with ET of 640 ms caused by clouds close to the sun and/or high aerosol loads, images with ET of 320 ms are used.

A clear-sky pixel for images with ET of 640 ms is detected if:

- $(B < 16) \ \& \ B - G < 5$
- $(B > 16) \ \& \ (B > G) \ \& \ (B > R)$
- $(B > 16) \ \& \ (G > B + 2) \ \& \ (B > R)$

A clear-sky pixel for images with ET of 320 ms is detected if:

- $(B < 16) \ \& \ B - G < 5$
- $(B > 16) \ \& \ (B > G) \ \& \ (B > R)$
- $(B > 16) \ \& \ (G > B + 2) \ \& \ (B > R)$
- $(B > 16) \ \& \ (B < 60) \ \& \ (G < 60) \ \& \ (R < 60)$

An example for a clear-sky mask (RGB values for the cloudy pixels) is shown in Fig. 3.5 (right).

Based on statistical colour and textural features [Kazantzidis et al., 2012] a k-nearest neighbour (KNN) cloud classification algorithm enables the distinction of five cloud types:

- Clear Sky (Cloud Cover < 10%)
- Cumulus
- Cirrus - Cirrostratus
- Cirrocumulus - Altocumulus
- Stratocumulus - Stratus

By the implementation of this classification technique the dominant cloud type in the whole image and per grid element in the image is determined (Fig. 3.5, left). Additionally, a second classification method provides a characterisation between no clouds, thin clouds and thick clouds in a grid element.

3.3 DNI measurements with pyrheliometers

For ground measurements of DNI at DLR's radiometric station at the PSA first class pyrheliometers of the type Kipp & Zonen CHP1 [Kipp & Zonen, 2008] are used (Fig. 3.8). By means of different apertures, the radiation from the sun and circumsolar radiation is measured, thus overestimating the actual DNI. With a viewing angle of $5^\circ \pm 0.2^\circ$ they comply with the current recommendation of the World Meteorological Organisation (WMO) for the half-angle aperture of pyrheliometers measuring DNI [WMO, 2014]. Also, the recommended 95% uncertainty confidence interval for radiant exposure is achieved. The instrument covers the solar spectrum from 200 to 4000 nm.

3.4 Cloud motion analysis using scale dependent image matching

The forecast of clouds from MSG/SEVIRI data rests upon an optical flow method determining a motion vector field from two consecutive images which is part of Cb-TRAM (Sect. 3.1.4). Unlike feature based approaches, often used for the determination of atmospheric motion vectors [e.g. Schmetz et al., 1993], this



Figure 3.8: Pyrheliometer of the type Kipp & Zonen CHP1 at the PSA.

method is pixel-based: instead of vectors only for interesting cloud patterns a disparity vector field \vec{V} defined at each pixel position P is derived.

Movements in the atmosphere take place on different scales reaching from micro-scale (few cm) to global scale (10000 km). These large-scale flows overlay the small-scale movements so that the determination of the disparity vector field for all scales is challenging. In order to take this into account the disparity vector fields are successively derived on different scales, starting from low resolution down to high resolution – a pyramidal scheme.

The procedure is described by means of an example for two images A and B (Fig. 3.9 a,b) with a size of $nx = 100 \times ny = 100$ pixels displaying two squares (10×10 pixels). Similar structures in the images A and B are identified iteratively at different spatial scales, i.e. for all sub-sampling levels l of the pyramidal approach with M levels, starting with the topmost level with the roughest resolution:

- 1) select the number of sub-sampling levels N (e.g. $N = 2$ for a pyramid with $M = N + 1 = 3$ levels): this number depends on the size of the shifts that are expected.
- 2) define the images $A_M = A$ and $B_M = B$, set $l = M - 1$.
- 3) start the iterative process:
 - 3.1) calculate the dimensions $nx_l = nx/2^l$ and $ny_l = ny/2^l$ of the given sub-sampling level l ($nx_l \times ny_l = 25 \times 25$ pixels for the topmost level, $nx_l \times ny_l = 50 \times 50$ pixels for the second sub-level).
 - 3.2) resample the start images A_{l+1} and B_{l+1} to $nx_l \times ny_l$ to obtain A_l and B_l .
 - 3.3) determine comparison images $A_{l,s}$ by shifting every pixel P in image A_l to $A_{l,s} = A_l(P + \Delta \vec{K}_{i,j})$ by $\Delta \vec{K}_{i,j} = (i, j)$, $i, j \in [-2, 2]$, in both dimensions.

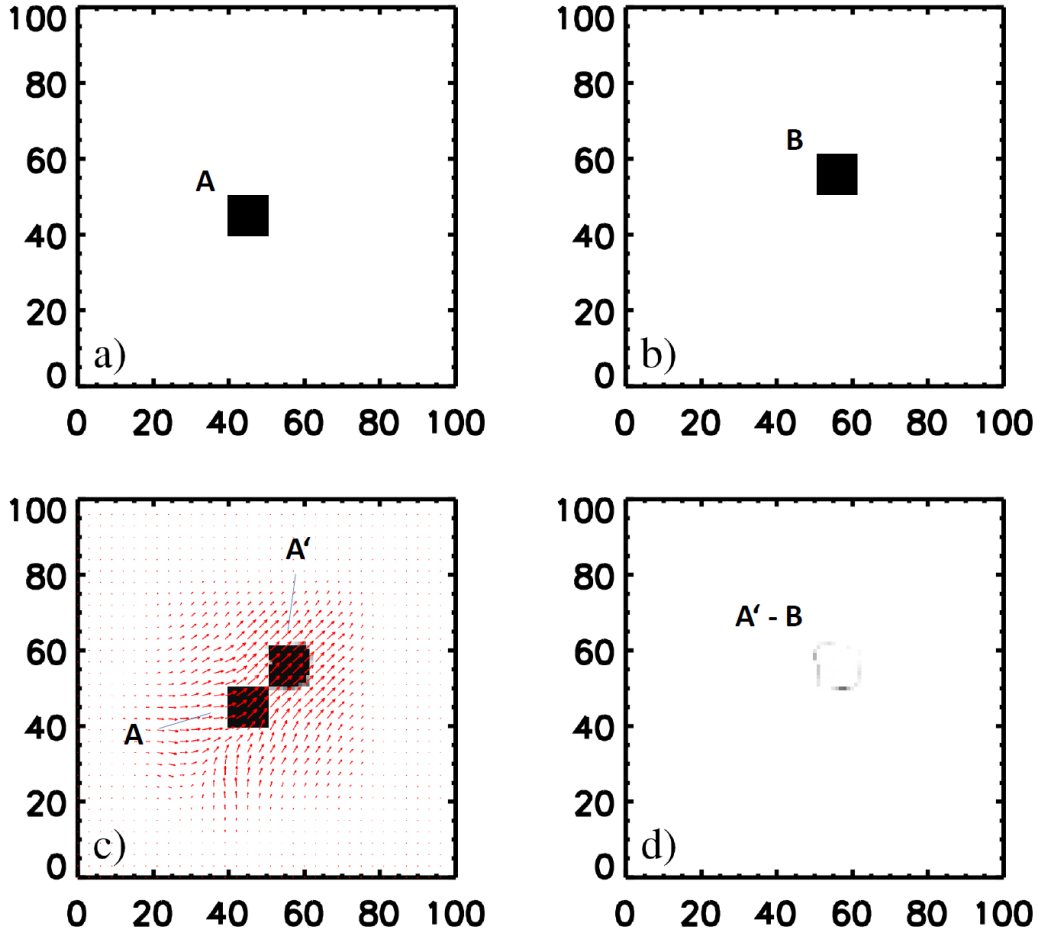


Figure 3.9: a) Start image A. b) Start image B. A and B are squares that have to be matched by the pyramidal matcher. c) The final disparity vector field \vec{V} is plotted on the start image A and $A'(P) = A(P - \vec{V}(P))$ with d) the remaining difference field $A' - B$ after processing on all pyramid levels.

3.4) identify the best fit between all possible $A_{l,s}$ and the target image B_l through minimisation of the squared difference d_{loc} of the intensities of $A_{l,s}$ and B_l in a surrounding of each pixel: $d_{loc} = (A_{l,s} - B_l)^2 \otimes Ke$ with Ke being the Gaussian Kernel. This results in the disparity vector field \vec{V}_l with dimensions $n x_l \times n y_l$. To mitigate the impact of singular incorrect motion derivations and ensure physically realistic local flow fields, these initially integer displacements \vec{V}_l are smoothed over the local neighbourhood of each pixel with Ke .

3.5) blow up the resolution of \vec{V}_l to the original one $n x \times n y$ to obtain $\vec{V}_{l,original}$.

3.6) add the motion vectors obtained so far to $\vec{V} = \sum_{i=l}^N \vec{V}_{i,original}$.

3.7) warp the image A with the disparity vector field \vec{V} to

$$A_l(P) = A(P - \vec{V}(P)) , \quad (3.1)$$

for every pixel position P . Notice that this equation implies that pixels P in A are not shifted with \vec{V} into A_l , but for every pixel P in the forecast image A_l a value from the starting image A is assigned which can be found there at position $P - \vec{V}(P)$. So every pixel is allocated to a value and no information gaps (i.e. no "holes" in the image A_l) occur in the forecast. However, since \vec{V} contains floating point values due to the smoothing in step 3.5, bilinear interpolation of A in x and y is applied when performing Eq. 3.1. Thus, the warped image is only a "remapping" of the start image.

3.8) reduce the value of l by 1 and go back to step 3.1 if $l \geq 0$.

- 4) End of the iterative procedure: The refined disparity vector field \vec{V} that has been obtained through successive addition of the results of all pyramidal levels provides the final disparity vector field $\vec{V}_{A \rightarrow B}$ in full resolution and its application to Eq. 3.1 yields the final warped image $A'(P) = A_{l=0}(P) = A(P - \vec{V}(P))$.

The refined disparity vector field $\vec{V}_{A \rightarrow B}$ in full resolution is shown in Fig. 3.9 c. Notice that it is different from zero not only over the area defined by the initial image A but also in the direct neighbourhood. Due to that, disparity vectors are not always pointing from A to B but, outside of image A and B , also in other directions. Figure 3.9 c also shows the final warped image A' . The displacement of image A onto B shows good results as the final remaining difference field (Fig. 3.9 d) $A' - B$ exhibits only small differences at the edges of the squares caused by the relaxation of the disparity analysis by smoothing.

For more details, technicalities and an additional example please see Zinner et al. [2008].

3.5 Satellite-based nowcasting methods

In Sect. 4 a new nowcasting method is presented, which will be compared to two satellite-based nowcasting algorithms (Sect. 4.5). These methods have been applied and refined in the EU project DNICast (www.dnicastproject.org) and are described below.

Meteotest method

In the nowcasting algorithm developed by the private weather company Meteotest the cloud detection is based on the MSG/SEVIRI HRV channel (during daytime) and the channels centred at $1.6\ \mu\text{m}$ and $10.8\ \mu\text{m}$ [Müller and Remund, 2016]. By using the Heliosat-2 method [Rigollier et al., 2004] a clearness index CI is derived:

$$CI = Gh/Gc, \quad (3.2)$$

with the amount of the clear-sky radiation (Gc) arriving at ground level and the global horizontal radiation (Gh). Thus, CI has values between 0 and 1. The conversion of CI to DNI is done following the formulation of Hammer et al. [2009].

For the calculation of cloud trajectories, the wind vector components U and V from the mesoscale numerical weather model WRF (www.wrf-model.org) are used. The wind information is taken at a fixed height of 4000 m above sea level with a temporal resolution of 5 minutes. As a clear-sky model the European Solar Radiation Atlas ESRA [Rigollier et al., 2000] is applied and the AOD is taken from an aerosol climatology based on satellite measurements from MODIS and MISR as well as ground measurements from AERONET [Müller and Remund, 2013].

Also, a post processing is done by comparing onsite measurements of DNI from the previous hour to all of the DNI values derived from the satellite image of the previous hour, which are the forecast starting points at horizon zero minutes to account for biases due to wrong inputs, e.g. aerosol load.

DFD method

The nowcasting algorithm developed by the German Remote Sensing Data Center (DFD) at DLR is based on MSG/SEVIRI and the AVHRR Processing scheme Over cLOUDs Land and Ocean (APOLLO), which has been adapted to SEVIRI. The physical properties, i.e. cloud optical thickness, are derived for four groups called cloud-free, fully cloudy, partially cloudy and snow/ice-contaminated [Saunders and Kriebel, 1988, Kriebel et al., 1989, Gesell, 1989, Kriebel et al., 2003] and for three layers according to their top temperature (low, medium, high). Further, each fully cloudy pixel is checked to see whether it is a thick (treated as a water cloud) or thin (treated as an ice cloud) cloud.

The so-called receptor model looks for the movement of a cloud towards the power plant using two separate cloud masks - one consists of thin ice phase clouds, the other of water or mixed phase clouds. It performs the following steps:

- 1) Remapping pixels in a 29×29 pixel neighbourhood from a latitude-longitude grid into a x-y kilometer polar coordinate system with the location of interest in the centre

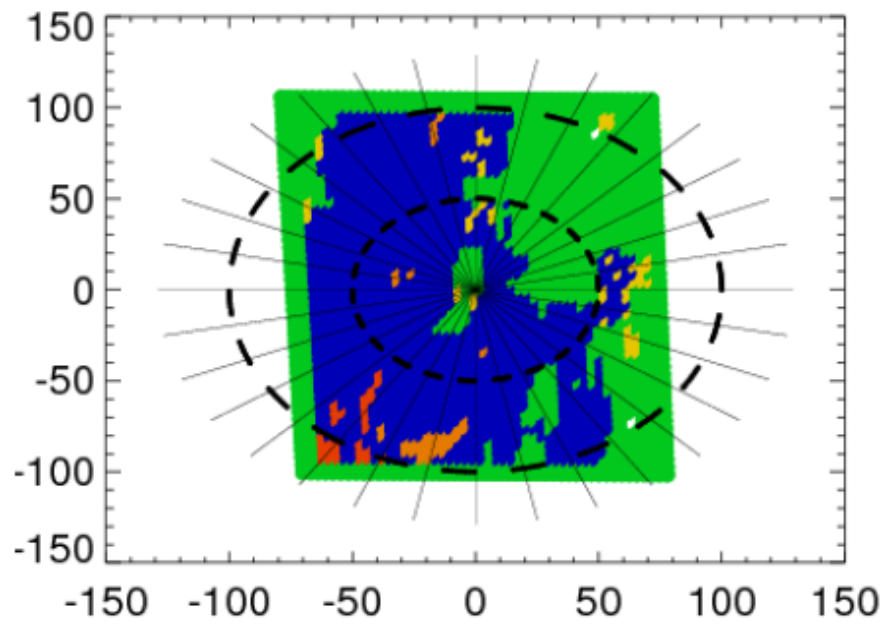


Figure 3.10: Sectoral approach with a cloud mask (blue, orange, red depending on cloud height) and cloud-free areas (green) distributed over an area of 150×150 km.

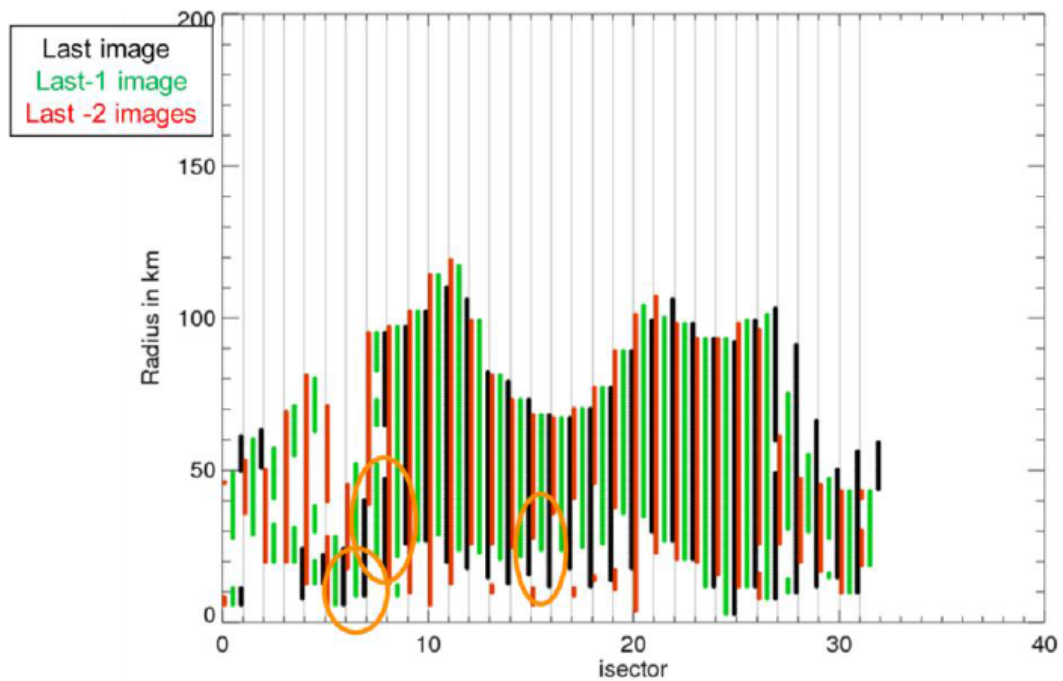


Figure 3.11: Evaluation of all sectors - colour lines show the existence of clouds along the sector lines. Relevant sectors - with motion vectors towards the plant - are marked with orange circles.

- 2) Performing a low pass filter of the cloud mask to omit small clouds. If there are less than 5 cloudy pixels in a 5×5 pixel area the central pixel is set from cloudy to cloud-free in the cloud mask
- 3) Tracking of clouds and cloud gaps moving towards the power plant within each sector (32 sectors in total, see Fig. 3.10) over 3 time slots of satellite imagery (Fig. 3.11). By mapping all pixels in the sector onto the central bisecting line the more detailed structure inside the two-dimensional sector is reduced to a one-dimensional vector of cloud mask values (cloudy, cloud-free).
- 4) Monitoring the cloud movement towards and away from the central pixel. Only if a sign change is found between all images this sector is used for a cloud movement vector derivation and a movement vector is calculated along the bisection line and for each sign change. According to the vector length, the time of reaching the central pixel is marked in the nowcasting vector describing the cloud mask situation at the central pixel as evolution over time.

Four cases are therefore tracked separately: Arrival of a thin cirrus or thick water/mixed phase cloud and end of such a cloud period. By that a vector of upcoming thin and thick cloud situations over time is created.

The mean optical thickness from all pixels in a sector is used to calculate the DNI according to Qu et al. [2016]:

$$\text{DNI} = \text{DNI}_{\text{clearsky}} * K_{\text{cB}}, \quad (3.3)$$

with the clear-sky index for beam horizontal irradiance K_{cB} , which is determined by

$$K_{\text{cB}} = \exp[-F * \tau_{\text{cloud}} / \cos(\vartheta_0)] \quad (3.4)$$

with F as an empirical factor of 0.5, the cloud optical depth τ_{cloud} and sun zenith angle ϑ_0 . $\text{DNI}_{\text{clearsky}}$ is derived by the clear-sky model McClear [Lefevre et al., 2013].

Chapter 4

Forecast of clouds and DNI with low resolution MSG/SEVIRI data

For the optimized operation of concentrating solar power (CSP) systems the knowledge and prediction of direct normal irradiance (DNI) is essential. For this, a satellite based forecast algorithm has been developed using low resolution channels of MSG/SEVIRI. It exploits the methods introduced in the previous section. First, a more advanced cloud classification is presented that distinguishes two overlapping classes of clouds (Sect. 4.1). Then, the pixel-based disparity vector field is determined for both cloud classes (Sect. 4.2.1). Cloud objects are formed, based on optical thickness, and motion vectors are derived for these objects (Sect. 4.2.2). After the assignment of motion vectors to cloud-free areas, clouds are warped to their new position with this motion vector field (Sect. 4.2.3). Fundamental work to Sect. 4.2.2 and 4.2.3 has been performed by Möhrlein [2013]. An optical thickness correction is applied for rapidly thinning convective clouds (Sect. 4.2.4) as in case of thin clouds DNI is reduced to a still usable level. In a last step the DNI is calculated from the optical thickness (Sect. 4.2.5). For verification purposes the forecasts are compared to observations from MSG/SEVIRI (Sect. 4.3) illustrated by case studies for different meteorological situations (Sect. 4.4). Additionally, a systematic validation with surface DNI is shown together with a comparison to two satellite-based forecasting methods (Sect. 4.5). All forecasts are performed with data from the MSG satellite operating in rapid-scan-mode (located at 9.5° East) in order to use the higher repetition rate. Sect. 4.1 - 4.3 have been published in Sirch et al. [2017].

4.1 Cloud classification

In the following clouds are classified in MSG/SEVIRI images according to two criteria: The first one considers the cloud top phase and the vertical structure of clouds (Sect. 4.1.1), the second identifies a type of convective clouds particularly relevant for our application, dissipating convective clouds with a thinning anvil (Sect. 4.1.2).

4.1.1 Cloud optical properties

Low level and high level clouds are often observed to move in different directions at different velocities due to complex wind profiles in the atmosphere. In order to take this aspect into account, we aim at the separation of low and high level clouds and the generation of two forecasts, one for low level and one for high level clouds. However, using APICS and COCS applied to MSG/SEVIRI satellite data according to Sect. 3.1.2, this is only possible to some extent. A high ice cloud layer as detected by COCS might occur in the same pixel as a low level liquid water cloud, which is not detected by COCS. Optical thickness of the cirrus cloud is then well accounted for by the COCS result, while APICS provides an approximation of the total optical thickness of the upper ice cloud and the lower water cloud together. Inaccuracies are due to the fact that cloud optical thickness is always derived by APICS according to the given cloud top phase, when the atmospheric column consists of both liquid water and ice this assumption fails and the resulting optical thickness is only an approximation to the correct total optical thickness. Furthermore, the ice layer detected by COCS might be the upper layer of a vertically and optically much thicker cloud like a Cb (Cumulonimbus). In this case, the total optical thickness of the cloud is most likely much larger than the COCS maximum value of 2.5, and APICS can much better capture this aspect since its optical thickness is based on the reflectivity of the entire atmospheric column.

In general, the discrimination among all these cases and the determination of optical properties for all cloud layers is challenging using only passive satellite observations. Several approaches have been proposed, for instance [Joiner et al., 2010, Gonzalez et al., 2003, Huang et al., 2005, Baum et al., 1995]. In this work, we want to forecast surface DNI, which becomes one per mill of the original value for a slant optical thickness of 7. To this end, all liquid water clouds usually reduce DNI to values far below the range interesting for CSP production due to their high optical thickness. Thus, accuracy in this range is not crucial. In case of thin cirrus, however, surface DNI is not zero and the accuracy of the ice cloud optical thickness is important as CSP is shut down when $\text{DNI} < 200 \text{ W/m}^2$, which corresponds to a vertical optical thickness of less than 2.

We exploit the differences between the APICS and COCS results for ice and li-

Table 4.1: Assignment of cloud optical thickness to two cloud classes called upper clouds and lower clouds. $\tau_{\text{APICS,liq}}$ is the APICS optical thickness for clouds with liquid cloud top phase, $\tau_{\text{APICS,ice}}$ is the APICS optical thickness for clouds with ice cloud top phase, τ_{COCS} is the COCS ice optical thickness, τ_{low} is the optical thickness assigned to the lower clouds, τ_{up} is the optical thickness assigned to the upper clouds [Sirch et al., 2017].

Liquid water cloud, no ice cloud above		
$\tau_{\text{APICS,liq}} > 0 \wedge \tau_{\text{COCS}} = 0$	\longrightarrow	$\tau_{\text{low}} = \tau_{\text{APICS,liq}} \quad \tau_{\text{up}} = 0$
Thin cirrus cloud, no water cloud below		
$\tau_{\text{APICS,ice}} \leq 2.5 \wedge \tau_{\text{COCS}} > 0$	\longrightarrow	$\tau_{\text{low}} = 0 \quad \tau_{\text{up}} = \tau_{\text{COCS}}$
Thick cirrus cloud, no water cloud below		
$\tau_{\text{APICS,ice}} > 2.5 \wedge (\tau_{\text{APICS,ice}} - \tau_{\text{COCS}}) \leq 2.3$	\longrightarrow	$\tau_{\text{low}} = 0 \quad \tau_{\text{up}} = \tau_{\text{COCS}}$
Multi-layer cloud		
$\tau_{\text{APICS,ice}} > 2.5 \wedge (\tau_{\text{APICS,ice}} - \tau_{\text{COCS}}) > 2.3$	\longrightarrow	$\tau_{\text{low}} = \tau_{\text{APICS,ice}} \quad \tau_{\text{up}} = \tau_{\text{COCS}}$

liquid water optical thickness to define two classes of clouds called upper clouds and lower clouds. These two cloud classes can overlap. The classification is performed following Table 4.1. Liquid water clouds identified following Sect. 3.1.2 are assigned to the lower cloud layer and their optical thickness is the APICS optical thickness. If APICS and COCS indicate a thin ice cloud ($\tau_{\text{APICS,ice}} \leq 2.5$), the presence of an ice cloud without lower liquid cloud layers is assumed and optical thickness of COCS is assigned to the upper cloud layer (because COCS is assumed to be more accurate than APICS for thin cirrus clouds). For a cloud with ice top and APICS ice optical thickness larger than 2.5, the difference between the APICS ice optical thickness and the COCS optical thickness is investigated. If their difference is smaller than 2.3 ($\tau_{\text{APICS,ice}} - \tau_{\text{COCS}} \leq 2.3$), this is interpreted as possible deviation between two different methods providing results for the same cloud. Please notice that if $\tau_{\text{APICS,ice}}$ is smaller than τ_{COCS} then this condition is always fulfilled, while an upper limit to $\tau_{\text{APICS,ice}}$ is set here as $\tau_{\text{COCS}} + 2.3$, i.e. $\tau_{\text{APICS,ice}}$ can be at most approximately twice as large as τ_{COCS} . Even if the situation of a thin liquid water cloud (included in APICS and not captured by COCS) cannot be excluded a priori, we assume that this is not the case here because there is no clear indication for this in the data. Since COCS is supposed to be more accurate than APICS for thin cirrus (and for the sake of a “consistent” treatment of thin ice clouds in this work) COCS optical thickness is selected for the upper cloud while the lower cloud optical thickness is set to zero. The threshold value of 2.3 has been determined empirically based on visual inspection of false colour composites like the one shown in Fig. 4.1 created by a combination of two visible channels centred at 600 nm and 800 nm and an infrared channel centred at 10.8 μm . The principal use of false colour composites is to aid in human visualisation and interpretation of gray scale events in an image. In this case the vertical structure of the clouds is suggested by the colours: a

yellow component is always associated with low (warm) clouds (i.e. a small blue component for which the inverted IR_{108} channel is used), while bluish or violet clouds are produced by low temperatures (i.e. high blue contributions).

When in contrast APICS retrieves an ice optical thickness larger than 2.5 (the upper limit of COCS) and the difference between APICS and COCS is larger than 2.3 ($\tau_{\text{APICS,ice}} - \tau_{\text{COCS}} > 2.3$), this difference is assumed to have physical reasons due to the presence of a lower cloud layer. The situation encountered here is thus either a thin ice cloud on top of a water cloud, or a vertically extended cloud with ice, liquid or mixed-phase microphysics below the upper ice layer.

In all cases the cloud is thick enough that DNI at the surface is diminished to below 10% of its TOA value. The correct optical thickness distribution between lower and upper cloud cannot be determined. This problem is solved in the following way: The optical thickness of the lower cloud is set to $\tau_{\text{APICS,ice}}$ and that of the upper cloud is set to τ_{COCS} . This ensures that the upper cloud is considered correctly in case of a thin cirrus on top of a low liquid water cloud. Then, when the upper and the lower clouds are moving in different directions and the sun can shine through the thin cirrus to the ground, the most appropriate ice cloud optical thickness is used. A high accuracy of the liquid water optical thickness cannot be achieved: it would require a retrieval exploiting solar channels with two cloud layers, a liquid water cloud below and an ice cloud above, i.e. with four unknown variables, optical thickness and effective radius of both layers, or at least three unknown variables if the ice cloud optical thickness derived by COCS using thermal channels is taken for granted and inserted into this imaginary solar retrieval. However, liquid cloud optical thickness is not important because it is usually so high that DNI is reduced to zero. This decision provides an arbitrary ice optical thickness assignment with respect to the upper and lower layers in the case of a vertically extended, Cb-like cloud. Nevertheless, this is again not crucial for our application since the cloud usually moves as a whole (i.e. lower and upper layer continue to overlap) and its total optical thickness is so high that DNI at the surface is always zero. The case where $\tau_{\text{APICS,liq}} > 0$, $\tau_{\text{APICS,ice}} = 0$ und $\tau_{\text{COCS}} > 0$ cannot occur since it is not foreseen in the cloud top phase mask described above which builds the starting point of the present classification.

For this classification, the threshold value of 2.3 used above has been determined empirically based on visual inspection of false colour composites since the real vertical structure of the clouds and the real optical thickness of the cloud layers cannot be derived quantitatively from MSG/SEVIRI observations. However, qualitative indications contained in the false colour composites could be exploited to provide a reasonable differentiation between one layer and two layer cloud situations as the yellow component is always associated with low (warm) clouds, while bluish or violet clouds are produced by high (cold) clouds. The value of 2.3 ensures that when the COCS optical thickness is close to its upper limit of 2.5 the APICS optical thickness must be almost twice as large in order to indicate a multi-layer cloud situation. This classification does not claim to be exhaustive and could be further optimised e.g. by the use of CALIPSO/CALIOP

lidar data [Winker et al., 2009]. However, it has the advantage of being computationally fast since it does not require to apply an additional cloud optical thickness retrieval in the case of multi-layer clouds and enables to take care at least partially of the cases when a thin ice cloud is found on top of low level clouds that often move into different directions such that the extrapolation has the possibility to account for this.

Summarising, the cloud classification presented above provides two possibly overlapping cloud layers: the lower cloud layer with an optical thickness between 0 and 100 and the upper cloud layer with an optical thickness between 0.1 and 2.5. Even if this method is not perfectly accurate, at least, it enables the detection of liquid water clouds below thin ice clouds and the discrimination between thin and thick ice clouds with a theoretical positive impact on the accuracy of DNI. The fact that lower water clouds can be observed simultaneously to ice clouds represents a great advantage for the tracking of low clouds. It is now possible to follow such a cloud when it is shaded by the advection of a thin cirrus cloud as long as the cirrus is thin enough.

For clarification an example is depicted in Fig. 4.1 for 7 April 2013. On this day a frontal zone is crossing the Iberian Peninsula. The different cloud types are illustrated by a SEVIRI false colour composite (Fig. 4.1 a). The yellow coloured cloud of the frontal zone consists of low, warm water clouds as shown by the blue coloured region in the cloud phase mask shown in Fig. 4.1 b. In other regions these clouds are overlaid by high thin ice clouds (blueish colours in Fig. 4.1 a), detected as multi-phase clouds in the cloud mask (red color). The green areas in Fig. 4.1 b denote single-layer ice clouds. Cloud free areas are depicted in white. Fig. 4.1 c and Fig. 4.1 d show the corresponding optical thickness for the upper and lower cloud layer derived by COCS and APICS according to the procedure described above and in Tab. 4.1.

4.1.2 Convective clouds

The focus of the presented forecast method is the accurate prediction of thin ice clouds since they modulate surface DNI in the relevant range. Often ice clouds are formed by convection. In contrast to most ice clouds that are mainly characterised by horizontal advection, convective clouds show a strong local vertical development. While during growth and maturity of convective cells large optical thickness values dominate and DNI at surface is negligible, anvil ice clouds formed during maturity can live much longer than the thunderstorm cloud itself during the decaying stage [Byers and Braham, 1948]. Thus, they can lead to large but isolated cirrus clouds that are indeed interesting for the DNI forecast at the surface. Considering that convection is stronger and more important at low latitudes, where the solar power potential is high too, the specific consideration of decaying convective clouds represents an important aspect.

For this reason, a third class of clouds is defined: we single out mature convect-

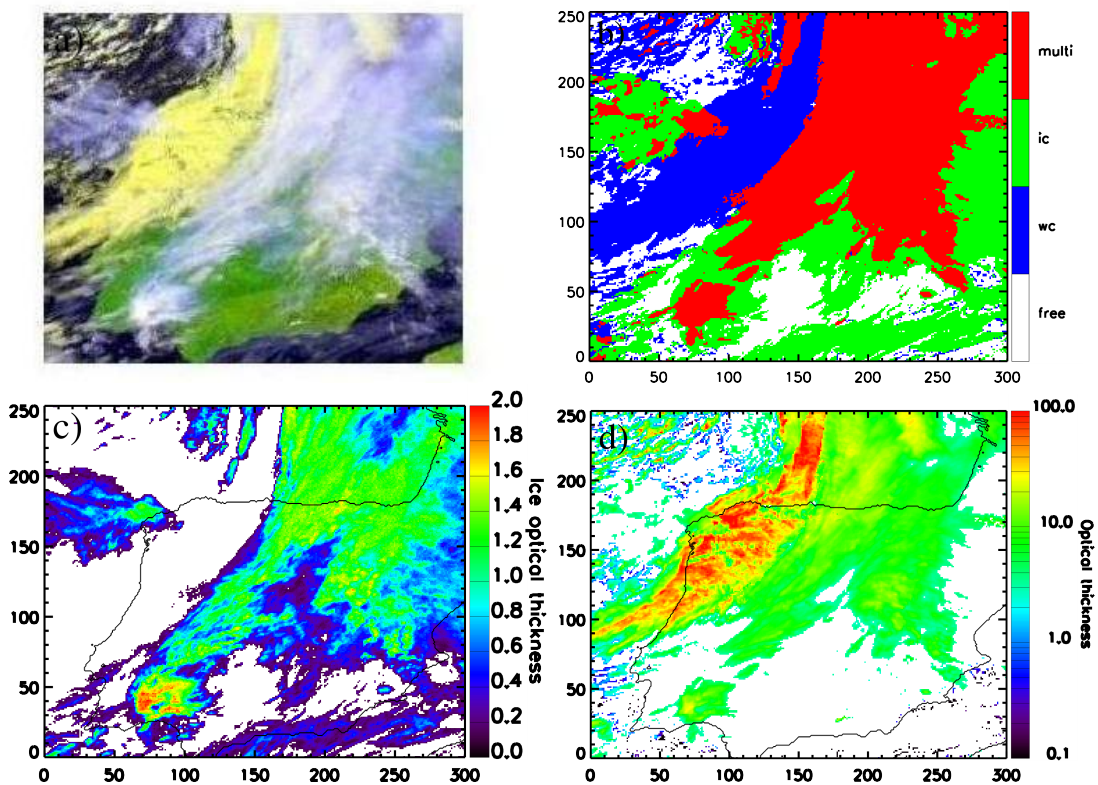


Figure 4.1: (a) False colour composite (VIS006, VIS008, IR_108) for 7 April 2013, 13:15 UTC, for the Iberian Peninsula. (b) The cloud mask for this scene with ice clouds in green, water clouds in blue, multi-phase clouds in red and cloud free areas in black and the optical thickness for upper (c) and lower (d) clouds [Sirch et al., 2017].

ive clouds using the stage 3 detection of the Cb-TRAM algorithm as discussed in Sect. 3.1.4. This classification is independent of the previous classification in lower and upper cloud layers (Sect. 4.1.1), but due to the nature of the convective life-cycle Cb-TRAM stage 3 detections turn out to always belong to the upper cloud layer.

4.2 Forecast algorithm

Once clouds have been classified and cloud optical thickness has been determined (Sect. 4.1), lower and upper clouds can be considered separately, i.e. two forecasts are implemented, one for lower and one for upper clouds. This separation is necessary since motion vectors of low and high clouds differ in most cases because of the different dynamics in these atmospheric layers. In particular, the wind speed in the troposphere usually exhibits very strong variations with altitude. Thus, we proceed in the following way: First, the optical flow method described in Sect. 3.4 (often referred to as the matcher) is applied separately to lower

and upper clouds producing two independent “pixel-based” motion vector fields (Sect. 4.2.1). Second, for reasons that will become evident below, these two motion vector fields are averaged over specific cloud subsets (Sect. 4.2.2). Finally, motion vectors are provided for the cloud free areas (Sect. 4.2.3).

4.2.1 Pixel-based motion vectors

In this first stage motion vector fields are derived for the optical thickness of lower clouds and upper clouds separately. Since convective clouds as defined in Sect. 4.1.2 are a subset of the upper clouds, they are not mentioned explicitly here since they do not play any role at this point. Optical thickness of lower clouds attains values from 0 to 100. For upper clouds the range is [0.1, 2.5]. Note that in order to avoid edge effects one should match areas larger than the given region of interest: the area used should be as large as to allow the observations of all clouds that will enter the region of interest during the time span needed for the forecast, in this case 120 min.

There are two reasons for the use of the optical thickness as input parameter for the matcher: first, it is the quantity which is needed for the calculation of DNI (see Sect. 4.2.5). Second, the matcher works best if only objects that are actually moving are matched against each other - in this case the cloud objects.

Forecasts are produced in forecast steps of $\Delta t_f = 5$ min up to a forecast horizon of 120 min. First, the disparity vector field $\vec{V}_{A \rightarrow B}$ between the initial images A and B separated by a time interval $\Delta t = 15$ min is determined by the pyramidal matcher with $N = 3$ pyramidal sampling levels (see Sect. 3.4). Accordingly, the possible “search radius” is given by at least $2^{(N+2)} = 32$ pixels, corresponding to an atmospheric motion of more than 360 km/h at mid-latitudes for the operational MSG/SEVIRI scan mode with 15 min repetition time (see also Zinner et al. [2008]). Then, a disparity vector field $\vec{V}_{5 \text{ min}}$ according to the length of the time step $\Delta t_f = 5$ min is computed by multiplication of the disparity vector field $\vec{V}_{A \rightarrow B}$ by

$$d = \Delta t_f / \Delta t , \quad (4.1)$$

i.e. by multiplication with the factor $d = 1/3$:

$$\vec{V}_{5 \text{ min}} = d \cdot \vec{V}_{A \rightarrow B} . \quad (4.2)$$

The forecast image $F_{5 \text{ min}}$ for the lead time of 5 min is then produced according to Eq. 3.1 with the corresponding disparity vector field $\vec{V}_{5 \text{ min}}$ applied to the later initial image B :

$$F_{5 \text{ min}}(P) = B(P - \vec{V}_{5 \text{ min}}(P)) \text{ for all pixels } P. \quad (4.3)$$

Forecasts with longer lead times can be performed as well. For the next forecast step of 10 min the two-dimensional disparity vector field $\vec{V}_{5 \text{ min}} = (u_{5 \text{ min}}, v_{5 \text{ min}})$ is shifted with itself. Thereby, the components of the motion vector are advected according to the cloud/air motion:

$$u_{5 \text{ min, shifted}}(P) = u_{5 \text{ min}}(P - \vec{V}_{5 \text{ min}}(P)) \quad (4.4)$$

$$v_{5 \text{ min, shifted}}(P) = v_{5 \text{ min}}(P - \vec{V}_{5 \text{ min}}(P)). \quad (4.5)$$

The shifted disparity vector field $\vec{V}_{5 \text{ min, shifted}} = (u_{5 \text{ min, shifted}}, v_{5 \text{ min, shifted}})$ provides the information about the disparity vector field at the position where the pixels will be located according to the atmospheric flow after 5 min. This vector is then added to $\vec{V}_{5 \text{ min}}$ to produce $\vec{V}_{10 \text{ min}}$

$$\vec{V}_{10 \text{ min}}(P) = \vec{V}_{5 \text{ min}}(P) + \vec{V}_{5 \text{ min}}(P - \vec{V}_{5 \text{ min}}(P)) \quad (4.6)$$

$$= \vec{V}_{5 \text{ min}}(P) + \vec{s}^{(1)}(P). \quad (4.7)$$

The first term on the right-hand side represents the displacement during the first 5 min, while the second term

$$\vec{s}^{(1)}(P) := \vec{V}_{5 \text{ min}}(P - \vec{V}_{5 \text{ min}}(P)) = \vec{V}_{5 \text{ min, shifted}}(P) \quad (4.8)$$

describes the displacement during the 5 min after the initial 5 min time step. The forecast image $F_{10 \text{ min}}$ for the lead time of 10 min is thus

$$F_{10 \text{ min}}(P) = B(P - \vec{V}_{10 \text{ min}}(P)) \text{ for all pixels } P. \quad (4.9)$$

The disparity vector field for 15 min can be expressed as

$$\vec{V}_{15 \text{ min}}(P) = \vec{V}_{10 \text{ min}}(P) + \vec{s}^{(2)}(P - \vec{s}^{(2)}(P)), \quad (4.10)$$

where $\vec{s}^{(2)}(P) = \vec{s}^{(1)}(P - \vec{s}^{(1)}(P))$ describes the displacement in the 5 min after the first two time steps, i.e. after the initial 10 min. This procedure is iterated for further time steps according to the general formula

$$\begin{aligned}\vec{V}_{n \cdot 5 \text{ min}}(P) &= \vec{V}_{(n-1) \cdot 5 \text{ min}}(P) + \vec{s}^{(n-1)}(P - \vec{s}^{(n-1)}(P)) \\ F_{n \cdot 5 \text{ min}}(P) &= B(P - \vec{V}_{n \cdot 5 \text{ min}}(P)), \quad n \geq 2,\end{aligned}\tag{4.11}$$

where any $\vec{s}^{(n)}$ is determined recursively as

$$\vec{s}^{(n)}(P) = \vec{s}^{(n-1)}(P - \vec{s}^{(n-1)})\tag{4.12}$$

$$\vec{s}^{(1)}(P) := \vec{V}_{5 \text{ min}}(P - \vec{V}_{5 \text{ min}}(P)).\tag{4.13}$$

Physically, this approach means that the motion vector field $\vec{V}_{5 \text{ min}}$ is supposed to describe the atmospheric flow as it can be determined from the two initial images. The forecast procedure, Eq. 4.11, follows the atmospheric flow in steps of 5 min by evaluating $\vec{s}^{(n)}$ at the different positions a cloud/air parcel runs through with time.

To illustrate the result of this forecast procedure we consider the upper cloud layer from the example in Fig. 4.1. The optical thickness of these clouds is depicted in Fig. 4.2 for 13:00 UTC (a) and 13:15 UTC (c). The disparity vector field $\vec{V} = \vec{V}_{A \rightarrow B}$ obtained from these two images is also displayed in Fig. 4.2 c using small arrows. For clarity only one out of ten vectors is shown. Nonetheless already this way a very large motion vector variability is visible, especially inside cloud regions and close to them. The large cloud field in the eastern part of the Iberian Peninsula is generally shifted towards east or northeast. However, motion vectors abruptly vary from one pixel to the next. The full motion vector field is applied to the 13:15 UTC image (using Eq. 4.11) to produce a 1 h forecast (Fig. 4.2 d). This forecast shows several deficiencies compared to the real cloud optical thickness observed at this time (Fig. 4.2 b) for the following reason: The pyramidal matcher provides a detailed motion field representative only for changes during a (short) 15 min time period. Small scale turbulence and changes produce a very variable disparity vector field (in direction and absolute value) not representative for a longer time period. As a consequence, cloud patterns dissolve into small patches within a short period of time, which does not correspond to reality as only the average larger scale motions stay stable over longer periods.

4.2.2 Object-based cloud motion vectors

For the reason discussed above, an averaging procedure for the pixel-based cloud motion vectors is implemented. To this end, neighbouring pixels with similar cloud characteristics (here optical thickness) are combined to objects. This procedure is called object classification and is applied separately to upper and lower

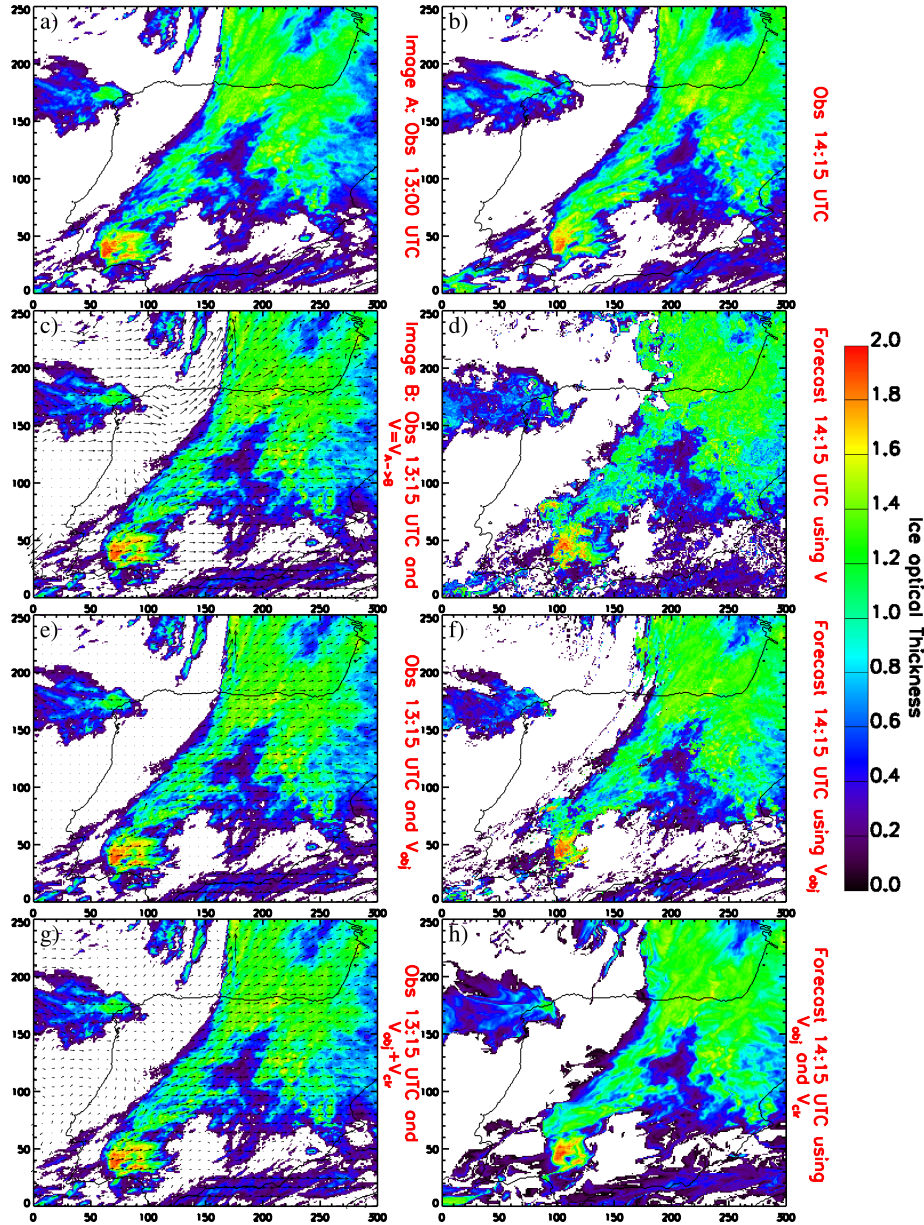


Figure 4.2: Illustration of the forecast of optical thickness for upper clouds for 7 April 2013 (a)+(c) Initial images A (13:00 UTC) and B (13:15 UTC) with the calculated pixel-based disparity vector field on top. (b) Upper cloud optical thickness at 14:15 UTC. (d) Pixel-based 1 h forecast (i.e. for 14:15 UTC) of upper cloud optical thickness. (e) Upper cloud optical thickness at 13:15 UTC with the calculated object-based disparity vector field \vec{V}_{obj} on top. (f) Object-based 1 h forecast for 14:15 UTC of upper cloud optical thickness. (g) Upper cloud optical thickness at 13:15 UTC with the calculated object-based disparity vector field on top for cloudy areas \vec{V}_{obj} and cloud free areas \vec{V}_{chr} . (h) Object-based 1 h forecast for 14:15 UTC of upper cloud optical thickness including cloud-free motion vectors [Sirch et al., 2017].

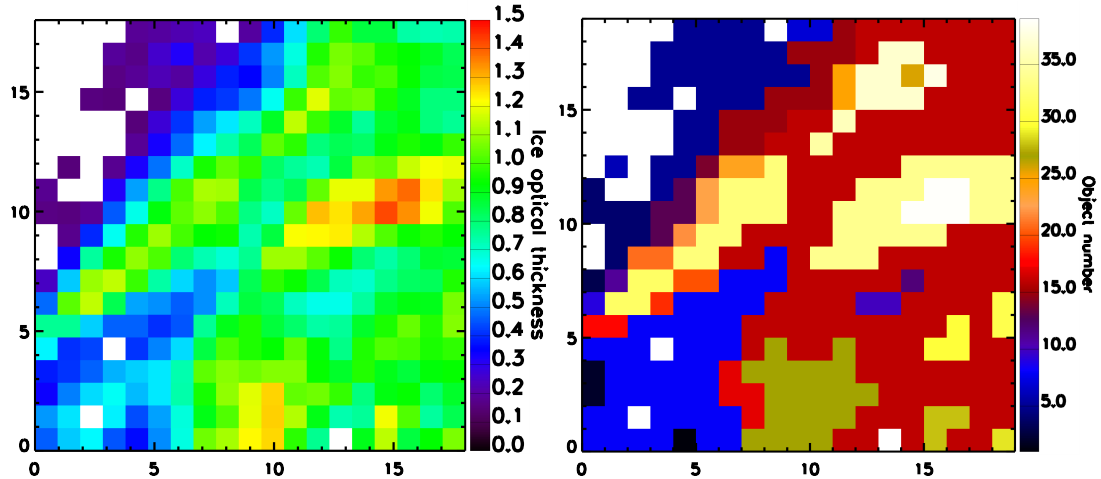


Figure 4.3: (Left) Upper cloud layer optical thickness extracted from the lower left part of Fig. 4.2 c. (Right) Corresponding classification into 39 objects: Pixels with the same colour belong to the same object [Sirch et al., 2017].

cloud layers since they are forecasted separately. At this step, convective clouds are treated separately. This averaging procedure removes small-scale variability which is realistic at the moment of derivation, but makes the forecast unstable. For upper clouds, first each convective cell (Sect. 3.1.4) is classified as an individual object as prerequisite for the application of a specific procedure presented further down (Sect. 4.2.4). For the remaining part of the upper cloud layer, the optical thickness range $[0.1, 2.5]$ is divided into eight classes with a bin size of 0.3 to create objects. An example for this object classification is depicted in Fig. 4.3. The upper cloud layer (left panel in Fig. 4.3), that does not contain any convective cell in this case, is separated into 39 objects (right panel in Fig. 4.3). Each object consists of all contiguous pixels belonging to the same of the eight optical thickness classes. The size of the single objects varies strongly from 1 pixel to 50 pixels or more. For the lower clouds the object classification is performed in a similar way: optical thickness in the range $[0, 100]$ is divided into 10 intervals with a width of 10.

Next, a mean motion vector is calculated for each object and this vector is assigned to every pixel in the object, i.e. the object will move as a whole during the forecasting procedure. The forecast image produced this way is called object-based forecast and an example is shown in Fig. 4.2 e,f for upper clouds. Fig. 4.2 e shows the upper cloud optical thickness of the 13:15 UTC image used to produce the disparity vector field together with the corresponding object-based disparity vector field \vec{V}_{obj} on top. Fig. 4.2 f shows the object-based forecast of upper cloud optical thickness for a lead time of 1 h. One can observe that the object-based cloud motion vector field is much smoother and points mainly to the east in the southern part and to the northeast in the northern part. The front position is well captured by the object-based forecast when compared to the observation. Comparing the object-based forecast (Fig. 4.2 f) to the pixel-based (Fig. 4.2 d), it

can be seen that the front line stays much more stable in the object-based forecast and the isolated cloud to the west (pixel position between 0 and 150 in x and between 150 and 200 in y) is moving as a whole and compares very well to the observation. However, e.g. the elongated cloud patches north of Spain (between pixel 100 and 150 in x and above pixel 200 in y) cannot be forecasted well and still the edge of the forecasted cloud layer looks too patchy.

4.2.3 Cloud-free background

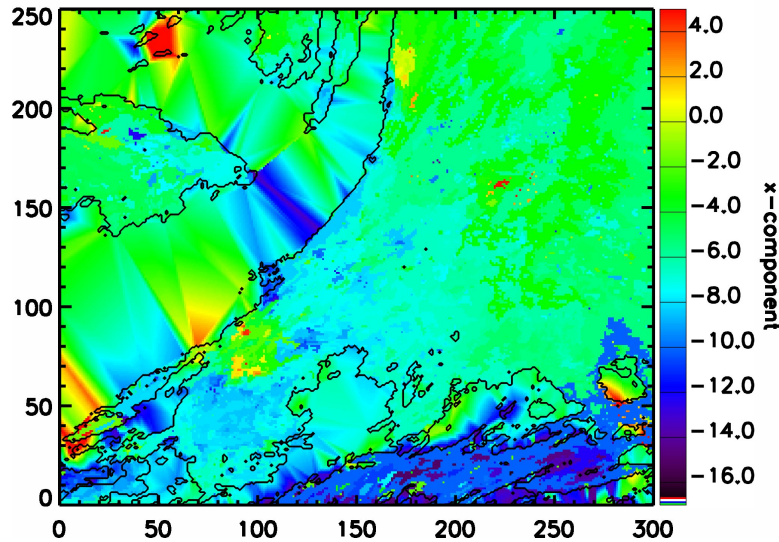


Figure 4.4: Delaunay triangulation for the x-component of the disparity vector field for upper clouds (black contours) returning a regular triangular grid of interpolated values between the clouds [Sirch et al., 2017].

As the motion vectors are derived from cloud optical thickness, the disparity vector field in the area between the clouds goes to zero (Fig. 4.2 e). In case those cloud objects move into these regions, they stop. The thin line left of the front line and the squeezed cloud in the lower left corner (between pixel 50 and 150 in x and between 0 and 100 in y) in Fig. 4.2 f show this effect. This is partially compensated through the mentioned advection of the disparity vector field before its use in the forecast. The remaining effect, for forecasts over extended lead times, is further minimized if the cloud-free areas are filled with sensible motion estimates.

The disparity vector field is divided into the object field for the clouds \vec{V}_{obj} and the field \vec{V}_{clr} for the clear-sky areas called background. A weighted triangular interpolation of the disparity vector field between clouds is applied. A Delaunay triangulation creates a triangle mesh for interpolation between single cloud object related vectors returning a regular grid of interpolated values. Delaunay triangulations avoid sliver triangles by maximizing the minimum angle of all the angles

in the triangulation. Therefore, a relatively uniform field can be created. Values inside the triangles issue from a smooth quintic interpolation of the wind field. The method used for the triangulation is the divide-and-conquer algorithm from Lee and Schachter [1980].

In Figure 4.4 a weighted interpolation for the x-component of the disparity vector field is shown. In cloudy areas (black contour) the derived disparity vector field is used, while the interpolated values for the background field are calculated between the clouds (triangular shape). For forecast applications the values of the background field are limited to a range between -25 and 25 to avoid high gradients. The resulting disparity vector field (Fig. 4.2 g) is significantly smoother than before (Fig. 4.2 c).

4.2.4 Optical thickness correction for quickly thinning convective clouds

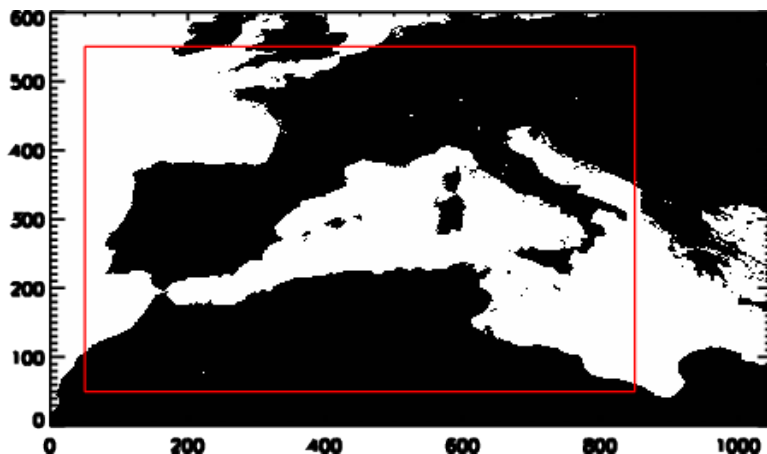


Figure 4.5: Domain used for the classification of decaying cells and for the validation presented in Sect. 4.3 (red square), from Sirch et al. [2017].

The pyramidal matcher (Sect. 3.4) can only predict the movement of the features in the images, i.e. rearrangement of values including divergence and convergence, but cannot create values in a given local area which could not be found, roughly speaking, within the “search radius” defined by the typical local wind/disparity vector (apart from the bilinear interpolation implemented in Eq. 3.1). That means local development of values of optical thickness is very limited in our case since the matcher is rather thought to detect object displacement and distortion. Neither in-situ formation of cirrus clouds, which are particularly important for DNI, nor the time and place of convective initiation can be predicted. Once a cloud is observed its future evolution can be forecasted by continuation of the observed development: e.g. an increase in optical thickness in a cloud patch can be forecasted through disparity vectors, as far as it can be represented by pure growth of areas with values of optical thickness present in the source image.

Values larger than the ones found in the local surrounding around the cloud patch in the source image cannot be provided in the forecast.

As mentioned before, the decaying stage of convective cells is of much interest for the purpose of DNI forecasting as thinning cirrus might allow an earlier recovery to DNI levels useful for CSP production (usually $\text{DNI} > 200 \text{ W m}^{-2}$). In contrast to the growing stage where, by no means, a nowcast of convective cell positions for the future two hours is possible, for the decaying stage at least some useable initial information on the convective cloud is available. It was found that in this particular case, when convective cells start to decay, leaving behind a thinning anvil cirrus layer, the temporal evolution of the cloud optical thickness can be reasonably well forecasted or at least improved with respect to the output of the matcher.

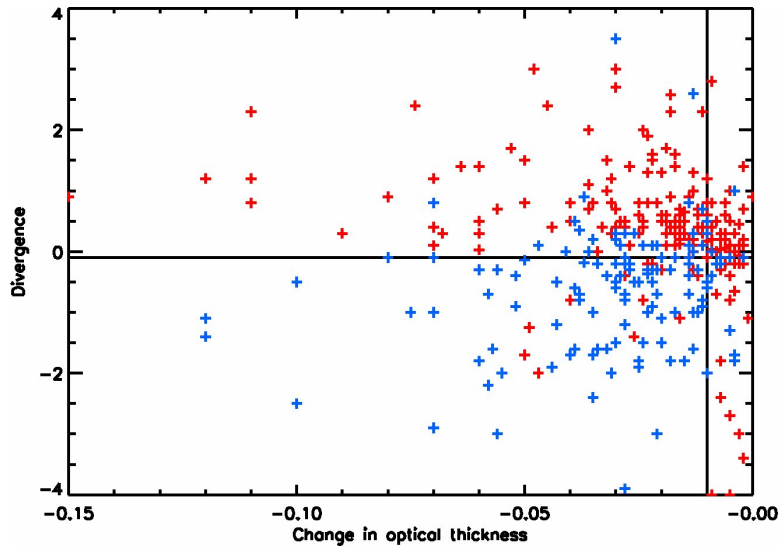


Figure 4.6: Distribution of the change in ice optical thickness in relation to the divergence with blue crosses denoting the decaying cells and red for the not decaying cells [Sirch et al., 2017].

To this end, quickly thinning convective clouds are first identified in satellite data and the successive evolution of their optical thickness, as far as it can be forecasted through disparity vectors, is then corrected to follow typical temporal patterns. Both the identification of these clouds and the determination of typical values for the temporal evolution have been developed based on 300 cells detected by Cb-TRAM (stage 3, mature cells, according to the classification presented in Sect. 4.1.2). They have been investigated manually in an area covering Central and Southern Europe including the western part of Mediterranean Africa with a size of 1050×600 pixels (Fig. 4.5) and for the time period April-June 2013. Cells were classified as decaying cells in cases where a decrease in optical thickness and a convergence of the anvil could be observed for the next time steps (temporal

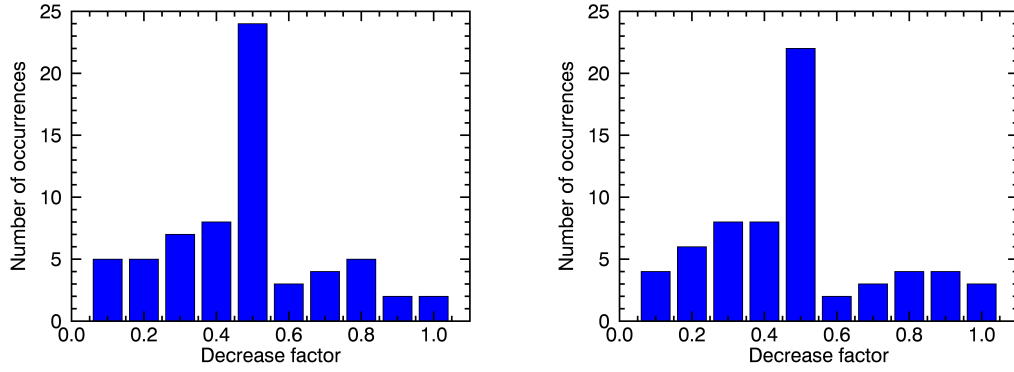


Figure 4.7: Distribution of the decrease factor $\Delta\tau/\Delta\tau_{\text{initial}}$ used to approximate the optical thickness decrease of a decaying cell (see text for details) for the 70 observed decaying cells for a forecast of 15 min (left) and 45 min (right), from Sirch et al. [2017].

resolution 15 min). The “divergence” $div(\vec{V})$ is derived from the motion vector field $\vec{V} = (u, v)$ for each pixel:

$$div(\vec{V}) = (u_{\text{right}} - u_{\text{left}}) + (v_{\text{above}} - v_{\text{below}}) \quad (4.14)$$

with the motion vector components (u and v) of the four neighbouring pixels above, below, right and left of the pixel under investigation: a positive value denotes a divergence, while a negative value indicates a convergence.

Figure 4.6 shows the distribution of the change in upper cloud layer optical thickness from one time step to the next averaged over an entire convective cell in relation to the average divergence of the given cell. The blue crosses denote cells which were found to be in decaying stage by eye and red ones for non-decaying cells. Obviously most blue crosses concentrate in a region with divergence smaller than -0.1 (horizontal line) and below a change in optical thickness of -0.01 (vertical line). As only a few red crosses for the apparently non-decaying cells lie in this area, these object averaged parameters can be used in an automated procedure for identification of quickly thinning upper clouds:

- mean change in optical thickness from one time to the next is smaller than -0.01;
- mean divergence div (Eq. 4.14) of the motion vector field is smaller than -0.1.

Thus, a decrease in optical thickness and a slight converging movement indicate a decaying cell.

To determine a typical correction term for the temporal evolution of upper cloud

optical thickness after the decaying phase has started, the subset of all 70 decaying cells has been investigated closer. An empirical modification derived from them is imposed onto the optical thickness of the convective objects forecasted through the disparity vectors. Before the application of disparity vectors as described in Sect. 4.2.2, optical thickness $\tau(P)$ of each pixel P inside the convective object is decreased by $f * \Delta\tau$. f is the number of time steps after the forecast starts and $\Delta\tau$ is an empirical average optical thickness step found using the mentioned 70 cases:

$$\tau_{\text{corr}}(P) = \tau(P) + \Delta\tau * f . \quad (4.15)$$

On its turn, the typical step $\Delta\tau$ is parameterised as a function of the observed mean optical thickness decrease $\Delta\tau_{\text{initial}}$ of the convective object's optical thickness between the two initial images.

This information $\Delta\tau_{\text{initial}}$ is selected because it depends on the convective cell

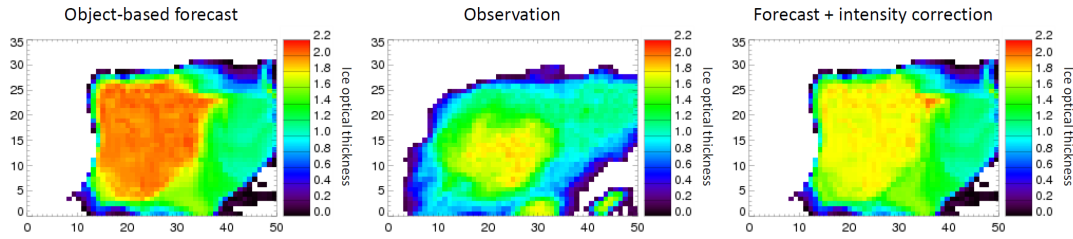


Figure 4.8: Upper cloud optical thickness for 9 June 2013, 17:00 UTC, for the real situation (middle) compared to the object-based forecast for 30 min (left) and the forecast with optical thickness correction (right), from Sirch et al. [2017].

under observation and because it is representative to the given atmospheric and physical conditions encountered. For application within the forecast procedure, the occurrence of $\Delta\tau/\Delta\tau_{\text{initial}}$ in the range $[0, 1]$ in bins of size 0.1 is investigated and shown in Figure 4.7 for a forecast of 15 min (left) and 45 min (right), where $\Delta\tau$ is the mean observed cell optical thickness decrease. It turns out that the mean initial optical thickness decrease of the convective cell is the strongest one and that the most typical decrease corresponds to half this value for all forecast lead times up to 1 h. Therefore, forecasts for all decaying cells are implemented using a decrease $\Delta\tau = 0.5 * \Delta\tau_{\text{initial}}$ in Eq. 4.15. This method is not reasonable for a forecast of more than one hour for the following reasons: 1) the remnants of the cells merge with other clouds and are not detectable anymore; 2) the forecast and the observation of the cell differ strongly in shape, size and position. Thus, for a forecast of more than 1 h no further decrease in optical thickness is applied. One example of a decaying cell is shown in Fig. 4.8. The object-based forecast for 30 min without optical thickness correction (left) predicts a larger ice optical thickness for the cell than it is in reality (middle). Fig. 4.8 (right) depicts the effect of the optical thickness correction. The upper cloud optical thickness

predicted by application of this optical thickness correction is lower and more realistic than for the original forecast (left).

4.2.5 DNI parameterisation

As mentioned in Sect. 2.7 DNI computed in this work considers only photons coming from the Sun that do not interact with the atmosphere (see the “strict definition” of DNI for numerical modeling of radiative transfer in Blanc et al. [2014]). In particular, neither circumsolar radiation nor 3-D radiative effects are taken into account. Thus,

$$\text{DNI} = \int E_0(\lambda) * \exp(-\tau(\lambda)/\cos(\vartheta_0)) d\lambda, \quad (4.16)$$

according to Lambert-Beer’s law (Sect. 2.2.4). Here, the integral over wavelength λ extends over the entire solar spectrum, $E_0(\lambda)$ represents the incoming solar radiation spectrum at top of atmosphere, ϑ_0 the solar zenith angle and $\tau(\lambda)$ the optical thickness of the atmosphere, including clouds, aerosols and (trace) gases. Eq. 4.16 shows again that DNI only depends on the optical thickness of the atmosphere and solar zenith angle ϑ_0 . However, integration must consider the spectral dependency of all atmospheric constituents (gases, aerosol and clouds). As far as gas absorption is concerned, water vapour is the main contributor, while other trace gases play a minor role. In particular, ozone variability influences irradiance at the surface by « 1% [Lohmann, 2006]. Nevertheless, water vapour absorption takes places in well-defined spectral intervals with a given intensity that must be considered when Eq. 4.16 is applied. In radiative transfer, methods like correlated-k [Lacis and Oinas, 1991] are usually deployed to this end.

Various aerosol types are present in the atmosphere, but desert dust is the most abundant constituent by mass. The information about aerosol type and optical thickness is not available from MSG/SEVIRI data in our context, thus it must be obtained from other sources, unless either a “standard” aerosol mixture with a typical optical thickness is used or the aerosol is neglected. Furthermore, the spectral dependence of optical thickness varies from aerosol type to aerosol type, even when the material is the same (aerosol shape can vary), making it difficult to account for it.

For clouds, the spectral dependence of optical thickness can be assumed as known for liquid water cloud (Mie theory can be used here), although this cloud type is usually not very relevant for DNI. For ice clouds, optical properties depend on ice crystal shape and various parameterisations are commonly used, e.g. Baran [2004], Baum et al. [2005, 2011]. Thus, in general the application of Eq. 4.16 requires the use of a radiative transfer model. For our application, however, where a large amount of pixels (~ 375000 per image [Sirch et al., 2017]) should be evaluated, both in the observation as well as in the forecast (usually in 5 min

steps for a forecast horizon of 2 h or even longer), we decided to parameterise Eq. 4.16 in order to speed up the computations. Thus, we write Eq. 4.16 as

$$\text{DNI} = E_0 * T_{bb}(\tau_{\text{aer},550}, \tau_{\text{gas},550}, \tau_{\text{cld},550}, \vartheta_0) \quad (4.17)$$

with the broadband solar constant $E_0 = \int E_0(\lambda)d\lambda$ (Sect. 2.6). T_{bb} represents the broadband transmission from TOA to the surface as a function of the aerosol optical thickness at 550 nm $\tau_{\text{aer},550}$, the gas optical thickness at 550 nm $\tau_{\text{gas},550}$, and the cloud optical thickness at 550 nm $\tau_{\text{cld},550}$. The dependence of transmission on solar zenith angle ϑ_0 is also indicated. The function T_{bb} is further expressed as the product of three transmissions for the three constituents (please note that strictly speaking this is only true for a single wavelength):

$$T_{bb} = T_{bb,\text{aer}}(\tau_{\text{aer},550}, \vartheta_0) * T_{bb,\text{gas}}(\tau_{\text{gas},550}, \vartheta_0) * T_{bb,\text{cld}}(\tau_{\text{cld},550}, \vartheta_0) \quad (4.18)$$

and every transmission function is further expressed as an exponential function, mimicking Lambert-Beer's law

$$T_{bb,\text{aer}}(\tau_{\text{aer},550}, \vartheta_0) = \exp(-g_{\text{aer}}(\tau_{\text{aer},550}, \vartheta_0)) \quad (4.19)$$

$$T_{bb,\text{gas}}(\tau_{\text{gas},550}, \vartheta_0) = \exp(-g_{\text{gas}}(\tau_{\text{gas},550}, \vartheta_0)) \quad (4.20)$$

$$T_{bb,\text{cld}}(\tau_{\text{cld},550}, \vartheta_0) = \exp(-g_{\text{cld}}(\tau_{\text{cld},550}, \vartheta_0)) . \quad (4.21)$$

The functions g_{aer} , g_{gas} and g_{cld} are tabulated by means of radiative transfer calculations with the radiative transfer model libRadtran [Mayer and Kylling, 2005, Emde et al., 2016]. Gas absorption is considered using the correlated-k approach by Kato et al. [1999] using the standard mid-latitude water vapour profile from Anderson et al. [1986] and varying the total precipitable water from 1 to 98 kg m⁻². Dependence on solar zenith angle is accounted for from $\vartheta_0 = 0^\circ$ up to $\vartheta_0 = 80^\circ$ with the sdisort [Dahlback and Stamnes, 1991] pseudospherical disort code. In order to account for high solar zenith angles, where DNI is still remarkably high but the usual plane parallel assumption fails, we avoided the usage of the $\cos(\vartheta_0)$ term in Eq. 4.17. For aerosol, we selected the maritime clean aerosol type and varied the optical thickness at 550 nm from 0 to 3.8. The aerosol optical thickness at 550 nm $\tau_{\text{aer},550}$ is available by the AERONET (AErosol RObotic NETwork) program at selected sites, in particular at the PSA (see Sect. 2.5). However, for the investigation of DNI over large areas, see Sect. 4.3, a single value of $\tau_{\text{aer},550}$ for the whole domain is assumed. For clouds, we only considered ice clouds according to Baum et al. [2011]. Thus, with these tables it is sufficient to read the input parameter and, using linear interpolation, apply Eq. 4.17 to estimate (observed and forecasted) DNI directly after the determination of cloud optical thickness (Sect. 4.1) without any call to the (external) radiative transfer model.

The PSA is located at an altitude of ~ 500 m above sea level. Therefore, the atmospheric column above the station is thinner than above a station at sea level resulting into a reduced optical thickness of the atmosphere τ_g . In order to take this into account LUTs with libRadtran have been calculated. Input data

are total optical thickness of the atmosphere, total column water vapour from ECMWF, a mid-latitude standard atmosphere and the altitude of the station. Fig. 4.9 depicts the total cloud optical thickness provided by adding up lower and upper layer's values (left) for the same scene as in Fig. 4.2 and the computed DNI (right). The values range from $0 W/m^2$ for areas with thick clouds (black) to around $900 W/m^2$ for cloud free areas. Thin clouds reduce the DNI according to Eq. 4.17 as can be seen in the lower right corner.

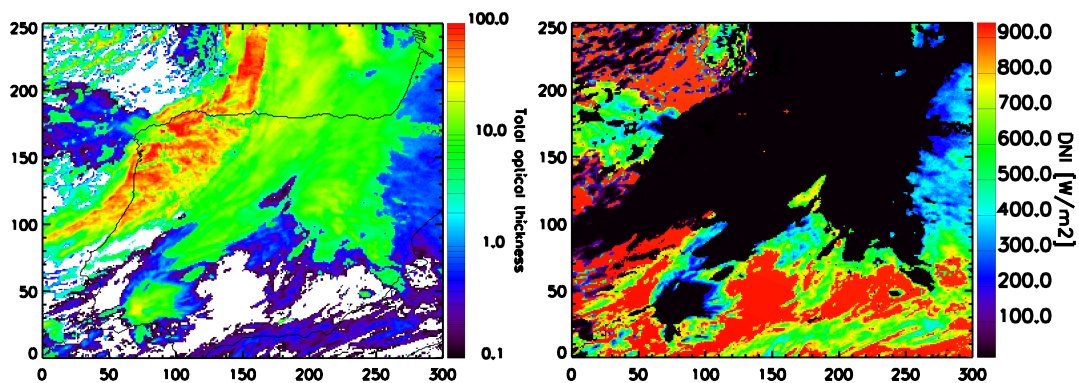


Figure 4.9: Optical thickness for upper and lower clouds together for 7 April 2013, 13:15 UTC (left) and the calculated direct normal irradiance in W/m^2 (right), from Sirch et al. [2017].

4.3 Cloud forecast verification

For a validation of cloud and DNI forecasts, two time periods, 4.3.2013 – 31.3.2013 and 1.7.2013 – 31.7.2013, were examined. These two months were chosen due to the appearance of different cloud types. The domain considered is the central part (marked in red) of the area investigated in Sect. 4.2.4 with a size of 751×501 pixels (Fig. 4.5). For March primarily advective clouds are present in this domain with an increasing amount of convective clouds in July. During daytime (solar zenith angle less than 80°) a forecast is started each full hour with a forecast horizon of 2h and a temporal resolution of 5 min. Forecasts are compared to observations from MSG/SEVIRI. They represent the best result that a forecast algorithm based on such data can achieve. However, this is not an absolute validation of cloud cover and DNI, but takes into account that the forecast can only be as good as the input quantities are.

4.3.1 Cloud masks

In order to quantitatively assess the performance of the forecast algorithm, we evaluate the capability of the algorithm to predict clouds and cloud-free pixels by

Table 4.2: Contingency table.

		Observation		
		Cloudy	Cloud-free	Total
Forecast	Cloudy	a	b	a+b
	Cloud free	c	d	c+d
Total		a+c	b+d	$N=a+b+c+d$

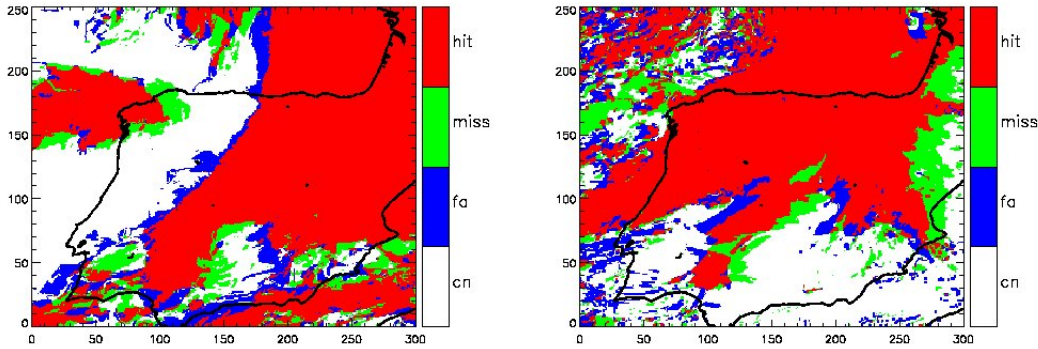


Figure 4.10: Illustration of the elements of the contingency table for upper (left) and lower (right) clouds with regard to the 1 h forecast for 7 April 2013, 14:15 UTC: hits in red, false alarms (fa) in blue, misses in green and correct negatives (cn) in white [Sirch et al., 2017].

examining the errors of the forecast cloud masks against observed cloud masks from MSG/SEVIRI. Observations and forecasts are connected through the contingency table (Table 4.2). Its four elements are the hits a , misses c , false alarms b and correct negative events d . Hits represent the number of pixels that are correctly forecasted as cloudy. Misses are the number of pixels that have been falsely predicted as cloud free although the observation is cloudy. False alarms are the number of pixels that are falsely predicted as cloudy although observations classify them as cloud free. Correct negatives are the number of pixels that are correctly forecasted as cloud free. Fig. 4.10 shows the four elements (hits in red, false alarms (fa) in green, misses in blue and correct negatives (cn) in white) for upper (left) and lower (right) cloud layers. Errors, especially for lower clouds, mainly occur at cloud edges or due to new developments or dissipating clouds. The calculated parameters of the contingency table for all start times are averaged for every forecast time step up to 2 h (see beginning of Sect. 4.3 for the illustration of the forecast data set evaluated here). In Fig. 4.11 (left) the forecast errors (misses plus false alarms) for March (triangles) and July (crosses) are shown in percent with respect to the total number of pixels in the scene for upper (red) and lower (blue) clouds. For the upper cloud layer (but not for the lower clouds, see below) errors for persistence (the cloud distribution at the forecast starting point is assumed to stay unchanged) are plotted for comparison. This compar-

ison illustrates the benefit of the developed forecast algorithm. Forecasts errors are significantly lower compared to persistence with the smallest values for the 5 min forecasts (errors below 5% for upper cloud layer). At this time, persistence is still close to the observation, because clouds change only slightly during this time step. Afterwards, forecast errors increase smoothly with every time step to a maximum after 2 h. The difference between persistence and forecast increases also with time. For instance, for the upper cloud layer errors reached by persistence after about 1 h are reached by the forecast only after 2 h for March and July. Compared to persistence, the forecast at least doubles the lead time at a certain quality level. Most noticeable are the differences between the two cloud layers. The performance of the algorithm for the upper clouds shows much better results than for lower clouds. The reasons are: 1) the difficulty of a retrieval for lower clouds below thick upper clouds, which leads to errors in the forecast when not all clouds are detected in the initial images, a low cloud layer disappears below a high one, or low clouds evolve into high clouds. 2) larger small scale variability for lower clouds, which cannot be resolved by SEVIRI [Wolters et al., 2010, Koren et al., 2008]. 3) sub-pixel inhomogeneity, i.e. broken cumulus cloud fields and rapidly changing small-scale convective cloud fields with very short time scales but low advection speeds [Bley et al., 2016]. 4) formation of new lower clouds that cannot be forecasted.

Errors are smaller in July compared to March, because of the low cloud cover of 22.1% on average (62.7% in March) during this month (errors are relative to satellite scene size). For water clouds, detection and forecast are hindered by the presence of upper clouds such that even a correct forecast might be incorrectly classified. Thus, it is difficult to assess the real accuracy of water cloud forecasts. For this reason, persistence for water clouds has not been evaluated. In

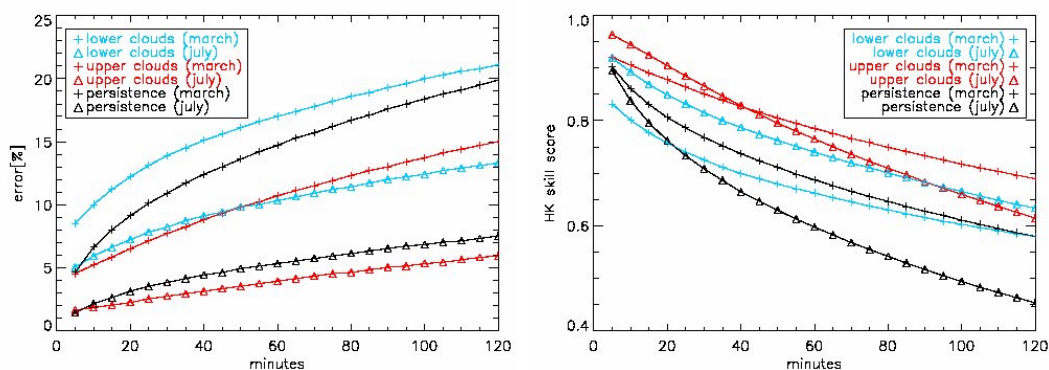


Figure 4.11: (a) Forecast errors (misses plus false alarms) and (b) the Hanssen-Kuiper skill score for March (triangles) and July (crosses) in percent for upper (red) and lower (blue) cloud layers and persistence for upper clouds (black), from Sirch et al. [2017].

addition to the evaluation of the errors as shown above, we apply the Hanssen-Kuiper (HK) skill score [Hanssen and Kuipers, 1965] to our data set. This score has been widely used for the evaluation of meteorological fields since many years [Woodcock, 1976]. It has been applied in particular to precipitation forecasts [e.g.

Stephenson, 2000, Accadia et al., 2003, Tartaglione, 2010, Gsella et al., 2014, Fekri and Yau, 2016] against observations but also to cloud retrieval algorithms [Reuter et al., 2009, Bugliaro et al., 2011, Reuter and Fischer, 2014].

The Hanssen-Kuiper skill score (henceforth referred to as HK), also called Hanssen-Kuiper discriminant, Peirce skill score [Peirce, 1884], or true skill score [Flueck, 1987], combines the four elements of the contingency table (Table 4.2) in the following way:

$$\begin{aligned} HK &= \frac{ad - bc}{(a + c)(b + d)} \\ &= \frac{a}{a + c} + \frac{d}{b + d} - 1 \end{aligned} \quad (4.22)$$

$$= \frac{a}{a + c} - \frac{b}{b + d}. \quad (4.23)$$

It can be expressed as the sum of the accuracy for events, i.e. the accuracy of forecasted clouds, (first term in Eq. 4.22, $\frac{a}{a+c}$, also called hit rate, H , or probability of detection, POD) and the accuracy for non-events, i.e. the accuracy of forecasted cloud-free pixels, (second term in Eq. 4.22, $\frac{d}{b+d}$). The subtraction of 1 in the end ensures that $-1 < HK < 1$. The HK can also be expressed as the difference between the hit rate $H = \frac{a}{a+c}$ (first term in Eq. 4.23) and the false alarm rate, $F = \frac{b}{b+d}$, or probability of false detection, $PODF$, (second term in Eq. 4.23). Thus, HK is a measure of the hit rate relative to the false alarm rate and remains positive as long as H is larger than F , i.e. indicates the ability of the forecast algorithm to produce correct cloud forecasts as well as to avoid false alarms.

A skill score of 1 denotes a perfect match (all detected clouds have been forecasted, misses c and false alarms b are zero), a score equal to -1 is related to a forecast not matching at all (hits a and correct negatives d are zero). Negative values are related to “inverse” forecasts and could be turned into positive values by interchanging forecasted events and non-events. A score of 0 is produced, e.g. by a forecast of a fully cloudy or fully cloud-free scene, or by a “random” forecast, i.e. when H and F are equal. In this sense, the HK represents the accuracy of the forecast in predicting the correct category with respect to the ability of a random selection. Furthermore, HK is independent of the relative frequency of the observations and also works with asymmetrical distributions, i.e. when more cloudy than cloud-free pixels are present or vice versa. This is an important feature of this skill score since different geographical areas, different seasons and different times of the day are characterised by different cloud amounts that can vary considerably. In fact, if the cloud cover is low, i.e. if clear-sky cover ($b + d$) is large ($a + c \ll b + d$), it is easy to correctly forecast (d) the largest part of it, as errors can only arise from small edge areas of small cloud cover (the forecast procedure does not account for cloud formation but rather shifts and modifies

the shape of existing clouds). Thus, the second term in Eq. 4.22 is large, i.e. the second term in Eq. 4.23 is small (few false alarms). This tendency to large HK score contributions due to high non-event accuracy (high accuracy of cloud free pixels) is balanced by the first term of the HK skill score both in Eq. 4.22 and Eq. 4.23. There the same error potential (misplaced cloud edges) leads to large cloud errors (a) compared to the small cloud cover ($a + b$). A low score contribution from events, i.e. a low hit rate, is the result. This way the direct effect of cloud cover on the skill score is minimised.

The resulting Hanssen-Kuiper (HK) skill score (Fig. 4.11, right) has been determined for upper (red) and lower (blue) clouds for both months with high values above 0.9 for the first time steps except for lower clouds in March (0.8) and a decrease to 0.6-0.7 after 2 h. As shown before the forecasts for upper clouds perform better than for lower clouds. The HK skill score for persistence for the upper clouds (black lines) is significantly lower than the respective forecasts (red lines) especially for July (black triangles vs. red triangles). Here, persistence already shows a lower skill for a 5 min forecast. This is mainly due to the lower hit rate of the persistence method with respect to the forecast in a situation where few clouds are present in the area under study (July has low cloud cover, see above): already a small displacement of the clouds can lead to significantly lower hit rates H in this situation (see discussion of the HK presented above). Differences of the accuracy of persistence for upper clouds between March and July are evident: the two black lines in Fig. 4.11 (right) diverge with time, a hint that upper clouds forecasts for July are more difficult than for March due to the predominately convective nature of clouds in July and to the inability of the matcher to forecast convective initiation and phase transition from liquid to solid during the convective process. However, the red curves in Fig. 4.11 (right) show that the HK skill score of the upper cloud forecast becomes lower for July than for March for lead times larger than 40 min. The faster score decrease in July is due to the newly developing convective clouds for which the forecast becomes inaccurate within a short period of time. The resulting larger cloud errors lead to lower values for July in the first term in Eq. 4.22 while the second term shows constantly high values due to the low cloud cover. The higher values in July for the first 40 min in the HK skill score originate from the score contributions due to high cloud-free pixels (non-events) accuracy (first term in Eq. 4.22). Nevertheless, the benefit in skill of the forecast compared to persistence can again be expressed as more than a doubling of lead times for a given score level.

For the lower cloud layer (blue curves in Fig. 4.11, right) the performance is better in July (blue triangles) than in March (blue crosses). This arises from the combination of: 1) a higher hit rate in March than in July, due to the larger lower cloud extent in March than in July and to the usually larger lower cloud sizes in March than in July (think of the frequent appearance of scattered cumuli in July) that makes it easier to forecast lower clouds in March, and 2) a higher false alarm rate in March than in July mainly due to the higher upper cloud coverage in March and the associated lower detection accuracy of lower clouds.

The second effect outweighs the first one such that lower cloud forecasts in July are more accurate than in March.

4.3.2 Cloud optical thickness

In order to test the performance of the algorithm with regard to the optical thickness a comparison of the forecasted optical thickness with the optical thickness observed from MSG/SEVIRI is done via a two-dimensional histogram separated into upper (Fig. 4.12) and lower cloud layers (Fig. 4.13). The colourbar denotes the total number of occurrences. We selected the forecast starting at 13:00 UTC on each day in March (Fig. 4.12 and Fig. 4.13 a,b,c) and July (Fig. 4.12 and Fig. 4.13 d,e,f) and compared forecast steps with the actual SEVIRI data measured. Comparisons of optical thickness for a 15 min, 1 h, and 2 h forecast with observed optical thickness are shown separately in Fig. 4.12 for the higher and in Fig. 4.13 for the lower cloud layer.

For the upper cloud layer, the algorithm shows an overall good performance with only small differences for most of the pixels for the 15 min forecast (Fig. 4.12 a,d) and an increase of spread for the 1 h forecast (Fig. 4.12 b,e) and 2 h forecast (Fig. 4.12 c,f), which is illustrated by the 90% percentile (white contour line). The fact that the COCS algorithm produces results of either 0 or the range $[0.1 - 2.5]$ creates the narrow line without values between 0 and 0.1. Larger deviations mainly occur for observed or forecasted optical thickness equal to zero, where clouds have been forecasted but not observed and vice versa (false alarms and misses). Remarkable is the existence of two maxima in good agreement for small optical thickness around 0.25 and large values around 1.5. These reflect the essentially two types of high clouds mostly occurring: thin cirrus clouds and optical thick upper parts of deep clouds. The corresponding correlation coefficients are also shown and they confirm the good performance of the algorithm with high values over 0.9 for the upper clouds for the first forecast time steps. In analogy to the analysis of the *HK* skill score, the correlation coefficients show higher values in March than in July, in particular for later time steps. This is most likely a consequence of the high frequency of convective clouds in July.

For the lower cloud layer (Fig. 4.13) the distribution is broader, due to the mentioned limitations of detection of lower clouds below higher ones. This is particularly true for March (Fig. 4.13 a,b,c) and obvious in the mismatch for observed optical thickness at the largest values of optical thickness (forecasted and observed optical thickness of 100). This seems to be more difficult for March than for July, most likely because of multi-layered clouds around frontal systems. The corresponding correlation coefficients show high values above 0.74 for the first time steps despite the lack in skill for cloud detection of lower clouds. Its deteriorating influence is apparent in the sharp decrease of the correlation coefficients for the 1 h and 2 h forecast.

To judge the quality of the forecast algorithm, histograms of the persistence

method for the upper cloud layer are shown in Fig. 4.14. Compared to forecasts in Figure 4.12, deviation distributions are much broader and correlation coefficients significantly lower.

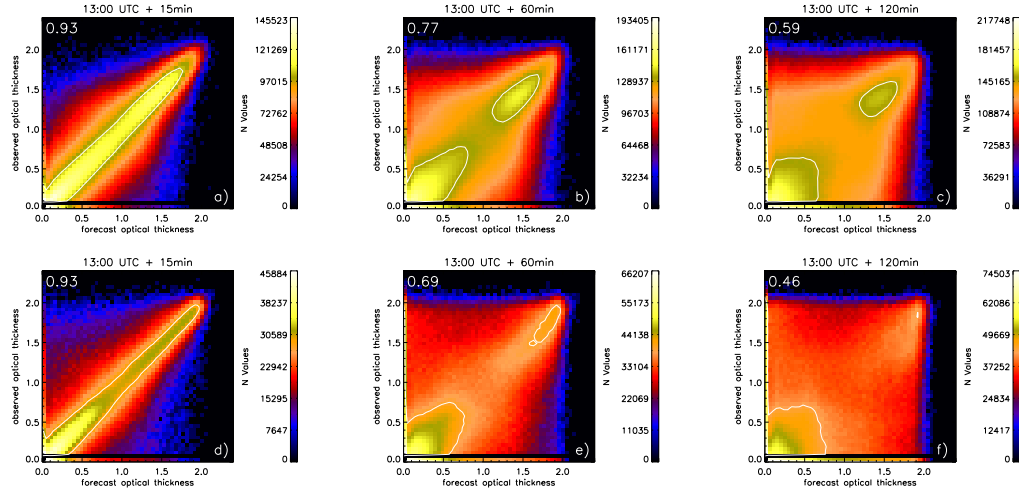


Figure 4.12: 2D histogram of the forecasted optical thickness of the upper cloud layer compared to the real optical thickness with forecasts starting at 13:00 UTC every day: for a 15min forecast (a) 1 h forecast (b) and 2 h forecast (c) in March and July respectively (d,e,f). Colours denote the total number of occurrences. The number in the upper left corner of all images is the correlation coefficient. The white contour line denotes the 90% percentile, [Sirch et al., 2017].

4.3.3 Direct Normal Irradiance

Fig. 4.15 illustrates the comparison of forecasted and observed Direct Normal Irradiance (DNI, Sect. 4.2.5) analogous to Fig. 4.12 and Fig. 4.13. DNI was calculated according to Eq. 4.17 with total cloud optical thickness from both cloud layers, aerosol and the atmosphere. Two maxima can be observed: 1) for low DNI in case of thick clouds and 2) for high DNI around $800 W/m^2$ for March (Fig. 4.15 a,b,c) and $900 W/m^2$ for July (Fig. 4.15 d,e,f) for cloud-free cases with varying solar zenith angle. In analogy to the comparison of optical thickness, high deviations arise from cloud cover false alarms and misses and because of the difficulties of detecting multi-layer clouds. Remarkable is the sharply defined region at high DNI values ($> 600 W/m^2$) showing a clear deficit of cases close to the 1:1 line. This is due to the fact that COCS does not provide measured values of optical thickness below 0.1. Thus large DNI values are missing in the “observation”, while the forecast can produce these optical thickness and DNI values.

The correlation coefficients for DNI are mostly higher than the values of both cloud types, especially for long forecasts, with lower values in July. This is due to

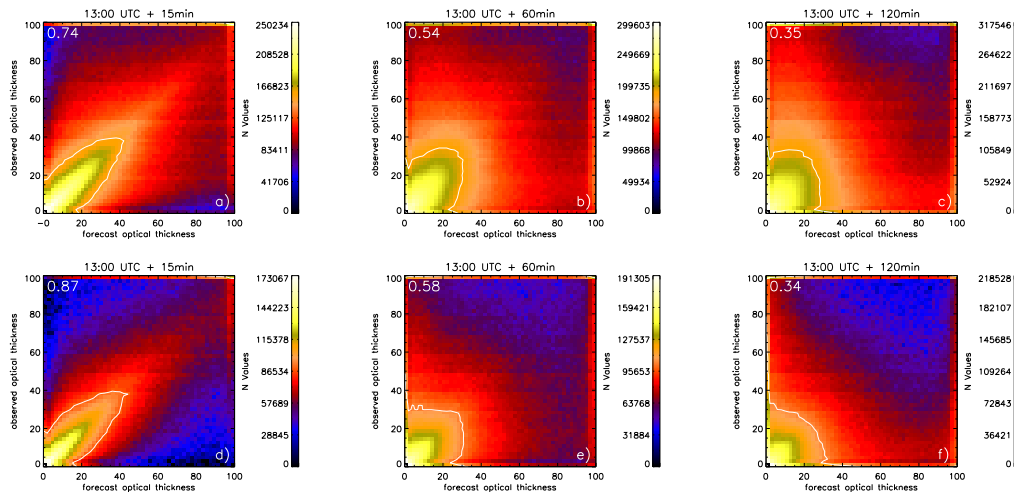


Figure 4.13: 2D histogram of the forecasted optical thickness for the lower cloud layer compared to the real optical thickness with forecasts starting at 13:00 UTC every day: for a 15min forecast (a), 1 h forecast (b) and 2 h forecast (c) in March and July respectively (d,e,f). Colours denote the total number of occurrences. The number in the upper left corner of all images is the correlation coefficient. The white contour line denotes the 90% percentile [Sirch et al., 2017].

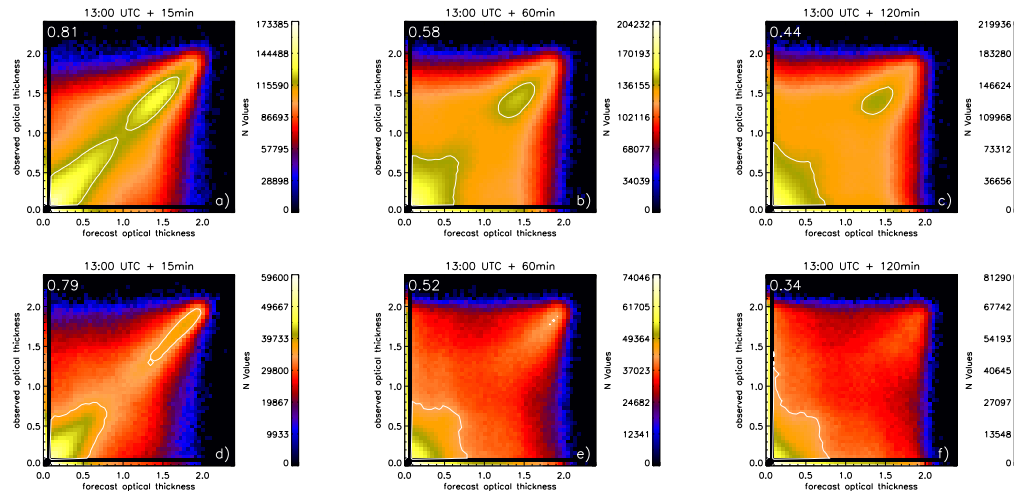


Figure 4.14: 2D histogram of the observed optical thickness of the upper cloud layer compared to the persistence optical thickness for a time difference of 15min (a), 1 h (b) and 2 h (c) in March and July respectively (d,e,f). Colours denote the total number of occurrences. The white contour line denotes the 90% percentile [Sirch et al., 2017].

the fact that forecasts are better for cloud areas with small optical thickness values than for optically thick clouds. Derivation of DNI emphasizes the relevance of these thin clouds for DNI predictions, while errors in the forecast of thick opaque clouds (e.g. new convective developments) are less detrimental.

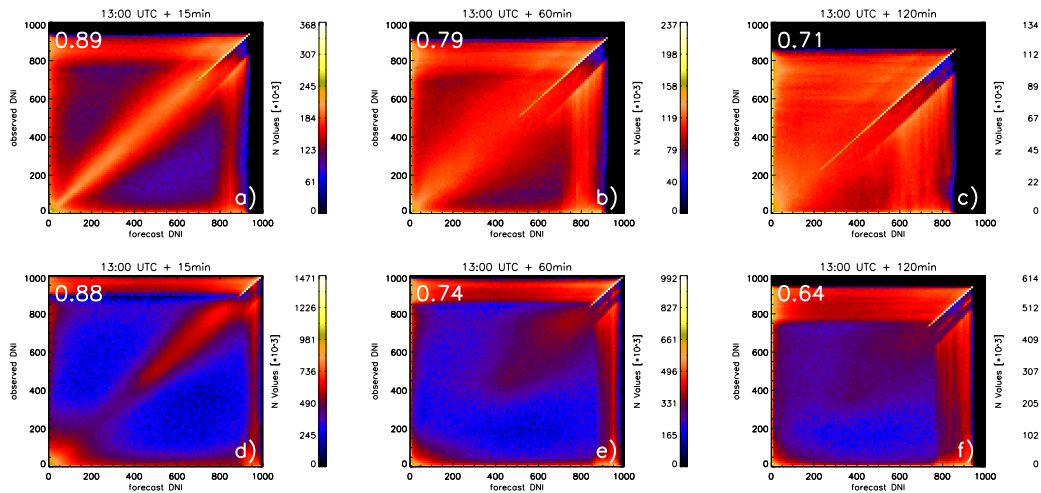


Figure 4.15: 2D histogram of the forecasted DNI compared to the observed DNI with forecasts starting at 13:00 UTC every day: for a 15min forecast (a), 1 h forecast (b) and 2 h forecast (c) in March and July respectively (d,e,f). Colours denote the total number of occurrences [Sirch et al., 2017].

4.4 Case studies

In order to illustrate the performance but also the limitations of the forecast algorithm case studies for different meteorological situations are shown in this chapter and the derived DNI is compared to ground-based DNI measurements by pyrheliometers (Sect. 3.3) for these cases. Thus, an advective and two convective cases, differing in cloud size and variability, have been selected.

In all case studies the time interval Δt between the initial images is 15 min and the forecast is performed with a temporal resolution of 5 min. Aerosol load and total column water vapor, which are required to calculate the DNI (Sect. 4.2.5), are derived by AERONET and ECMWF, respectively. To enable a correct comparison a collocation of the cloud position as observed by the satellite and by surface measurements is necessary. For this, a parallax correction has to be applied to the satellite images, which is presented in the following section.

4.4.1 Parallax correction

In satellite applications parallax is the apparent shift in an object's position, i.e. clouds and its shadow, as a result of viewing angle and sun geometry. Thus, this effect increases with increasing distance to the sub-satellite point and cloud height. Due to sun and satellite geometry the real location of a cloud above ground and its shadow is not consistent with the view of the satellite. To correct this error an exact knowledge of the position of the satellite, the cloud boundaries and the sun as well as the geographical location of the measuring instrument on

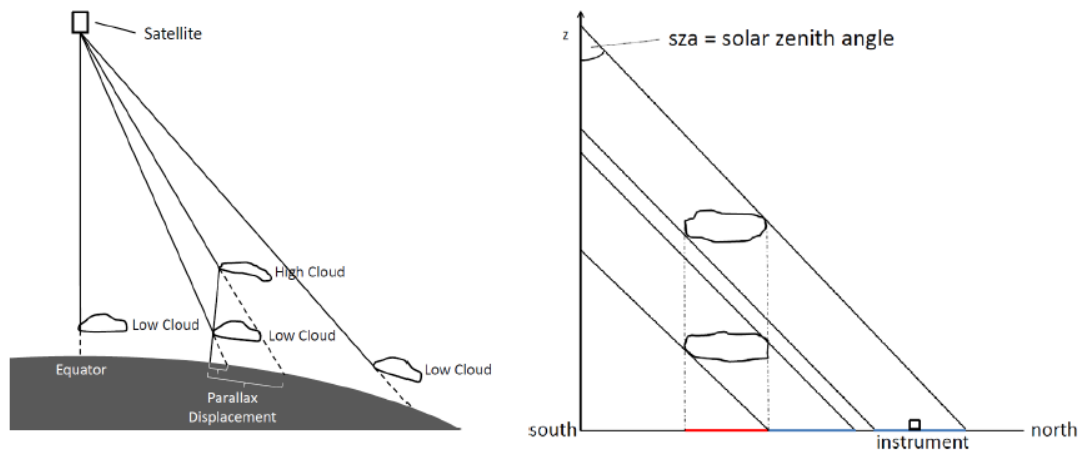


Figure 4.16: Illustration of the parallax displacement by satellites (left) and the sun (right). High clouds are displaced further than low clouds.

the earth is required.

Fig. 4.16 (left) illustrates the parallax displacement Δy in north-south direction - positive values to the north - for a high and low cloud and the dependency of Δy on cloud height and distance to sub-satellite point. For higher clouds the distance between the actual cloud position above the ground and the position observed by the satellite is larger. For this, a preferably accurate knowledge of the cloud base height (CBH) and cloud top height (CTH) is necessary - a challenging task as no exact two-dimensional measurement is available. In order to calculate the parallax displacement Δx in east-west direction - positive values to the east - also cloud height and distance to sub-satellite point must be known. By combining the displacements Δx and Δy the position of the cloud above ground is determined.

To take into account the parallax displacement due to sun position an exact knowledge of the sun geometry throughout the day as well as the cloud height is required. Fig. 4.16 (right) shows the displacements Δy for a high and low cloud for a solar zenith angle. In this case the shadow of the high cloud reduces the irradiance at the location of the measuring instrument, whereas the shadow of the low cloud is located further south. Thus, the displacements Δy and Δx are dependent on cloud height, geometrical thickness and solar geometry (zenith and azimuth angle). By applying the parallax correction due to sun and satellite geometry the clouds between sun and measuring instrument are determined and the attenuation of DNI caused by these clouds can be calculated from their optical thickness.

A prerequisite for the exact calculation of the parallax correction is, as mentioned, the knowledge of CTH and CBH. For ice clouds CTH is derived by COCS, though no information about CBH is available. To derive CBH ceilometer data are used, which are available for the PSA, but they are only useful for ice clouds above the station. As the parallax displacement can exhibit values of 20 km (or more

in case of high solar zenith angles) also clouds in a large distance from the PSA may have influence on the incoming radiation. For these clouds a geometrical thickness of 2 km is approximated according to typical spatial extensions of ice clouds [Sassen and Campbell, 2001, Mace et al., 2001, Nazaryan et al., 2008] and CBH is calculated by $CBH = CTH - 2 \text{ km}$.

In case of water clouds the CTH is derived by using the brightness temperature T_b (Sect. 2.2.5) of the SEVIRI channel centred at $10.8 \mu\text{m}$. T_b is compared to the temperature profile of a mid-latitude standard atmosphere [Anderson et al., 1986] to obtain CTH. For the CBH of water clouds again ceilometer data are used, if available. Otherwise a CBH of 2 km is approximated, a typical value for the height of the atmospheric boundary layer (according to ceilometer data) and thus a minimum for CBH as no clouds can form in the boundary layer due to the strong mixing. In case of multi-layer clouds, a continuous cloud is assumed and a separation of cloud layers is not considered. CTH is derived by COCS and for CBH the method used for water clouds is applied.

After applying the parallax correction the DNI is calculated according to Sect. 4.2.5 using the total cloud optical thickness. Therefore, no separation into upper and lower clouds is necessary, but can be performed if required.

4.4.2 24 June 2014

Predicting large temporal changes in radiation, e.g. due to cloud advection, is essential for an optimized operation of CSP systems. The exact time for shut-down and start-up processes maximizes electricity production, thus reducing operation costs, and prohibits possible damages to the collectors. As the change in radiation from maximum value (cloud free) to zero and vice versa can take place within minutes or less in case of sharp cloud edges a most accurate determination of these times is required.

On 24 June 2014 convective clouds develop during the afternoon. Between 13:30 UTC and 14:00 UTC a large cumulus cloud with a cloud base height of $\sim 2 \text{ km}$ according to ceilometer data is crossing the PSA eastwards reducing the incoming DNI from more than 900 W/m^2 to $\sim 0 \text{ W/m}^2$ within two minutes and vice versa half an hour later. In between the DNI is variable due to the varying optical thickness of the cloud. The false color composite (VIS006, VIS008, HRV, IR_108) in Fig. 4.17 a shows the area around the PSA (red star) and the above-mentioned cloud (yellowish cloud in the center) at 13:30 UTC together with the corresponding camera image for this time (Fig. 4.17 b). Please note the reversed north-south direction in the camera image (Sect 3.2). From the camera perspective the thunderstorm, which can be seen in the upper (northern) half of the false colour composite, is displayed in the lower edge.

The derived optical thickness for this scene (Sect 3.1.1), used to calculate the DNI according to Sect. 4.2.5, is depicted in Fig. 4.17 c together with the corresponding cloud phase mask in Fig. 4.17 d. The ground measurements of DNI (Fig. 4.18,

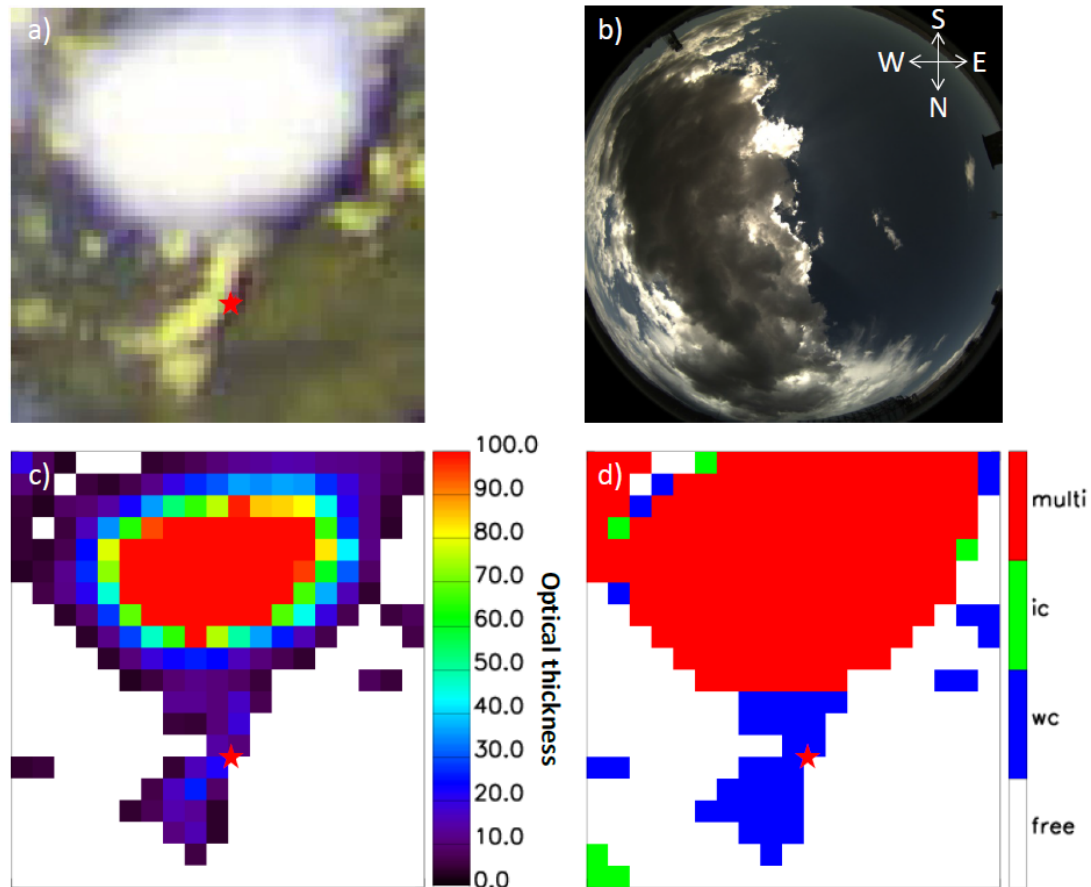


Figure 4.17: (a) MSG/SEVIRI false colour composite in high resolution, (b) camera image, (c) total optical thickness derived by APICS and COCS and (d) cloud phase mask for 24 June 2014, 13:30 UTC. The red star marks the position of the PSA.

black curve) for this time period (12:00 - 14:30 UTC) illustrate the sharp gradient caused by the cloud at 13:30 and 14:05 UTC, which is also apparent in the satellite observations (cyan curve), but with a shift of ~ 5 min caused by uncertainties in the parallax correction and the coarse resolution of the satellite. For this reason, the satellite is also not able to detect the variability of optical thickness in the cloud and a mean optical thickness for each pixel is derived. In case that a pixel is partially cloudy, it can only be classified as cloudy or cloud-free. Thus, the measured DNI values can vary whereas the satellite derived DNI is constant like in this case (13:30 - 14:05 UTC). Note the good performance of the DNI parameterisation in case of clear sky with small differences of $0 - 30 \text{ W/m}^2$ between ground measurements and satellite observations.

With the algorithm (Sect. 4.2) three forecasts with a temporal resolution of 5 min have been performed to show the accuracy for various forecast lead times. As forecasts with long lead times of several hours would not be reasonable due to the atmospheric variability on this day, the forecasts start at 11:15, 12:15 and 13:30 UTC (Fig. 4.18). The forecast with a short lead time which starts at 13:30

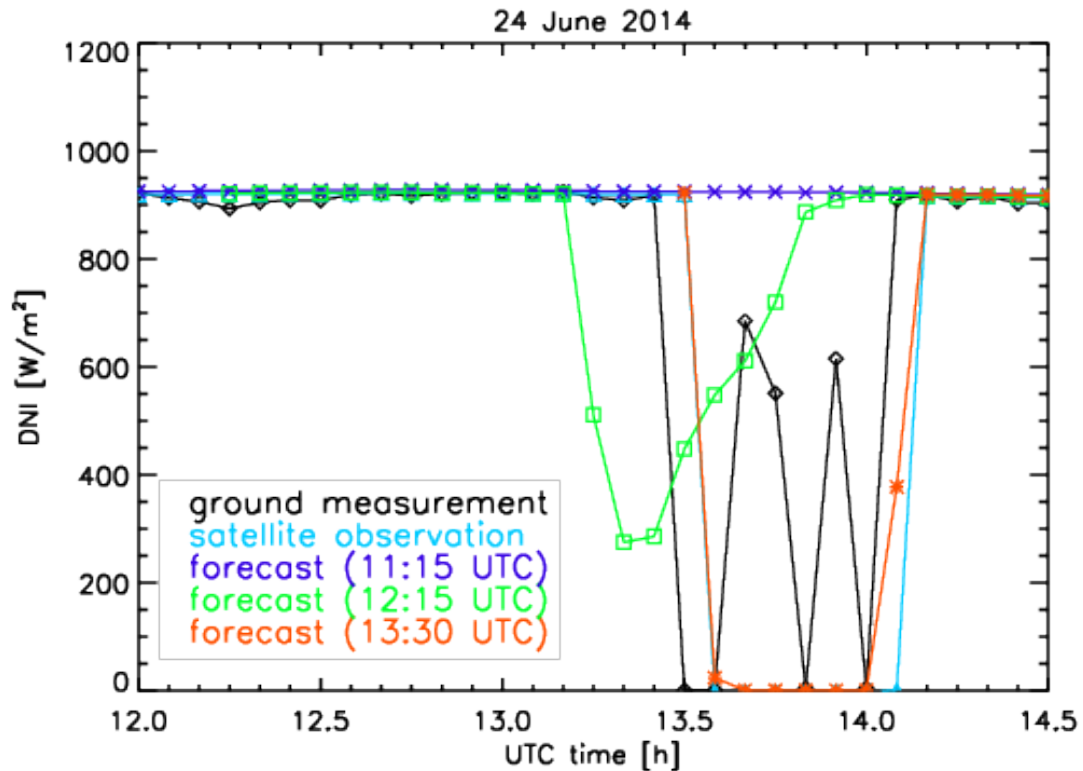


Figure 4.18: Measured (pyrheliometer, black curve) and satellite derived (MSG/SEVIRI, cyan curve) DNI values for 24 June 2014, 12:00-14:30 UTC. Three forecasts (with MSG/SEVIRI data), started at 11:15 UTC (blue curve), 12:15 UTC (green curve) and 13:30 UTC (red curve), have been performed to show the accuracy for various forecast lead times.

UTC (red curve) predicts the gradients in DNI at 13:30 and 14:05 UTC correctly (apart from the mentioned shift) and the forecasted DNI values are comparable to the observed values (differences of maximum $5 W/m^2$) for the next hour except at 14:05 UTC. With this information operators of CSP plants are able to respond to the upcoming period of low insolation. As the period is quite short (~ 30 min) it could have been bridged by the use of storage or fuel and the plant could have run through the event without to be shut down.

Regarding the forecast which starts at 12:15 UTC (green curve), the cloud is predicted to reach the PSA earlier than in reality and with a lower total optical thickness. Fig. 4.19 shows the optical thickness (a) and the cloud mask (b) of the satellite observation at 12:15 UTC. The water cloud in the red ellipse is going to cross the PSA at 13:30 UTC (Fig. 4.19 c,d) at its edges, which are optically thin, and thus the DNI is not reduced to zero, but the duration of this period with reduced DNI (~ 30 min) is predicted correctly. Although the forecast is not exact this information is still useful for the operators as they can prepare for an upcoming period of low insolation. The forecast with longer lead time (start at 11:15 UTC, blue curve) does not predict the crossing of the cloud over the PSA

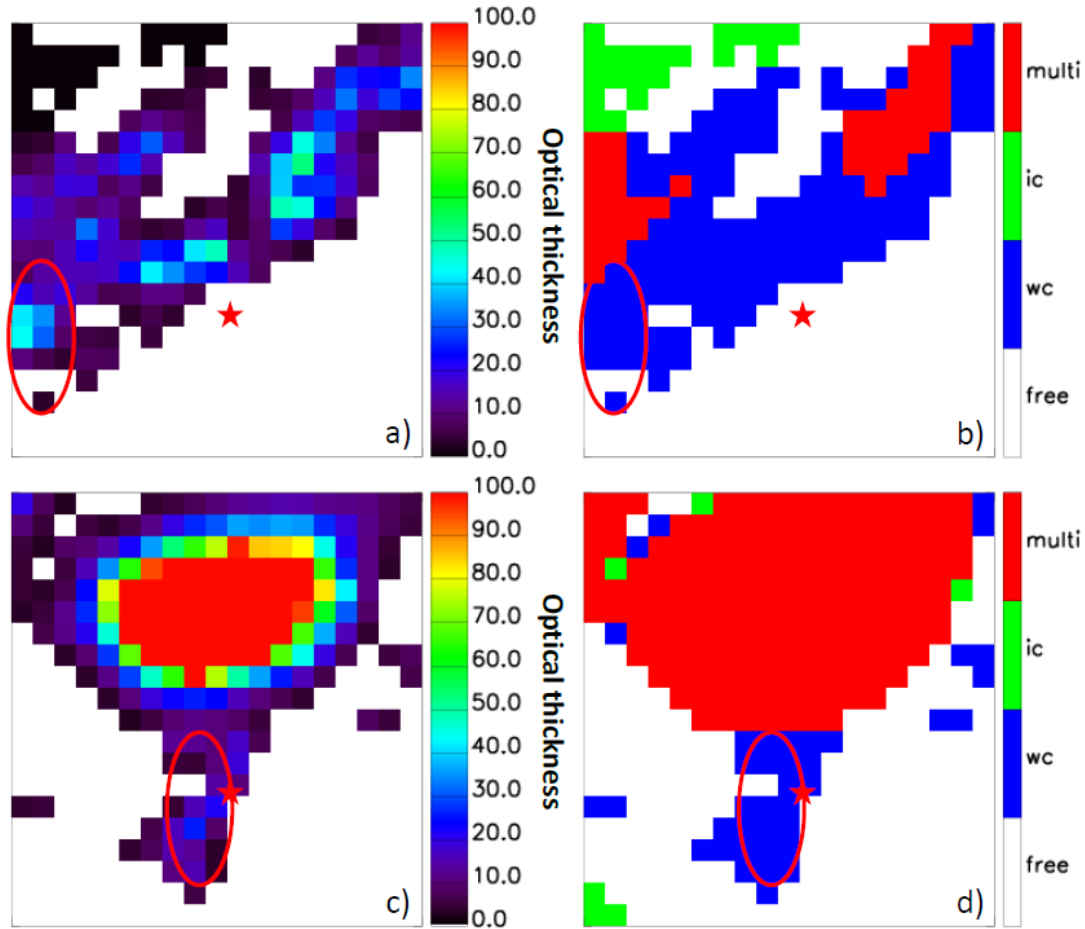


Figure 4.19: (a) Cloud optical thickness and (b) cloud mask for 24 June 2014, 12:15 UTC and (c)+(d) 13:30 UTC. The cloud crossing the PSA (red star) is circled in red.

at all as its formation takes place at a later time.

4.4.3 8 September 2014

In contrast to water/mixed phase clouds, thin ice clouds can reduce DNI to a still usable amount. CSP is shut down when $DNI < 200 W/m^2$, which corresponds to a vertical optical thickness of 2. Therefore, an exact knowledge of optical properties, i.e. ice optical thickness, is essential to predict if this limit is reached. The false colour composite and the camera image in Fig. 4.20 a,b show a inhomogeneous cirrus cloud crossing the PSA (red star) on 8 September 2014 with an optical thickness (Fig. 4.20 c) up to 7 and a cloud base height of ~ 8 km according to ceilometer data. In the cloud phase mask (Fig. 4.20 d) parts of the cloud are labeled as multi-layer clouds. That does not mean that there are water clouds below the cirrus but that the cirrus is optically thick and is thus classified as multi-layer cloud according to Sect 4.1.1. The corresponding DNI (Fig. 4.21)

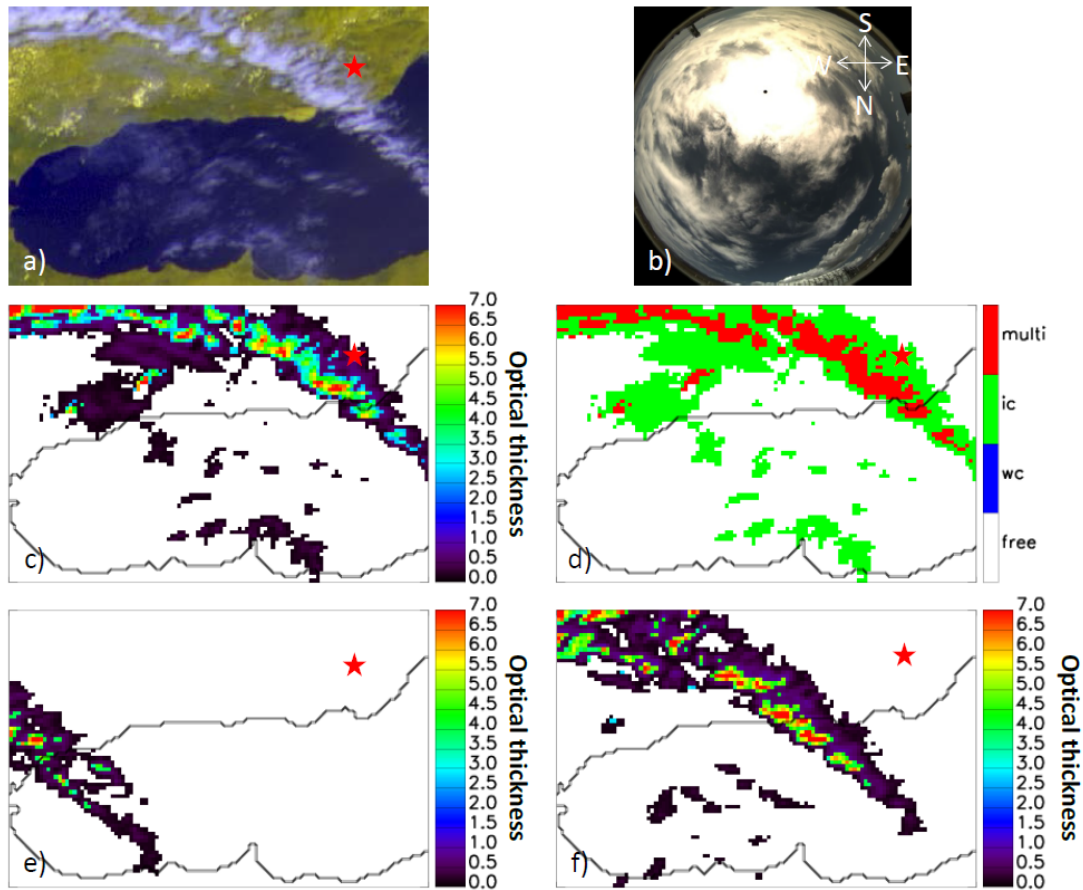


Figure 4.20: (a) MSG/SEVIRI false colour composite in high resolution, (b) camera image, (c) total optical thickness derived by APICS and COCS and (d) cloud phase mask for 8 September 2014, 12:15 UTC as well as total optical thickness derived by APICS and COCS for (e) 09:15 UTC and (f) 11:15 UTC. The red star marks the position of the PSA.

is reduced to values between $\sim 15 W/m^2$ and $\sim 700 W/m^2$ depending on the optical thickness of the cirrus. By comparing the ground measurements (black curve) with the satellite observations (cyan curve) a slight underestimation of DNI can be observed due to the inhomogeneity of the cirrus cloud. Having in mind that an exact retrieval of cloud optical properties is challenging the results show a good estimate of optical thickness.

Forecasts for various lead times have been performed starting at 09:15, 11:15 and 12:00 UTC. The DNI is overestimated for all forecasts except for 12:00 UTC - an indication that the optical thickness of the cloud has increased during the last hours, an effect that cannot be caught by the forecast algorithm. This assumption is confirmed by the increase in optical thickness and spatial growth (Fig. 4.20) for 09:15 UTC (e) and 11:15 UTC (f).

The time when the cirrus reaches the PSA is predicted correctly for all forecasts, which is an excellent result considering that these are forecasts with lead times

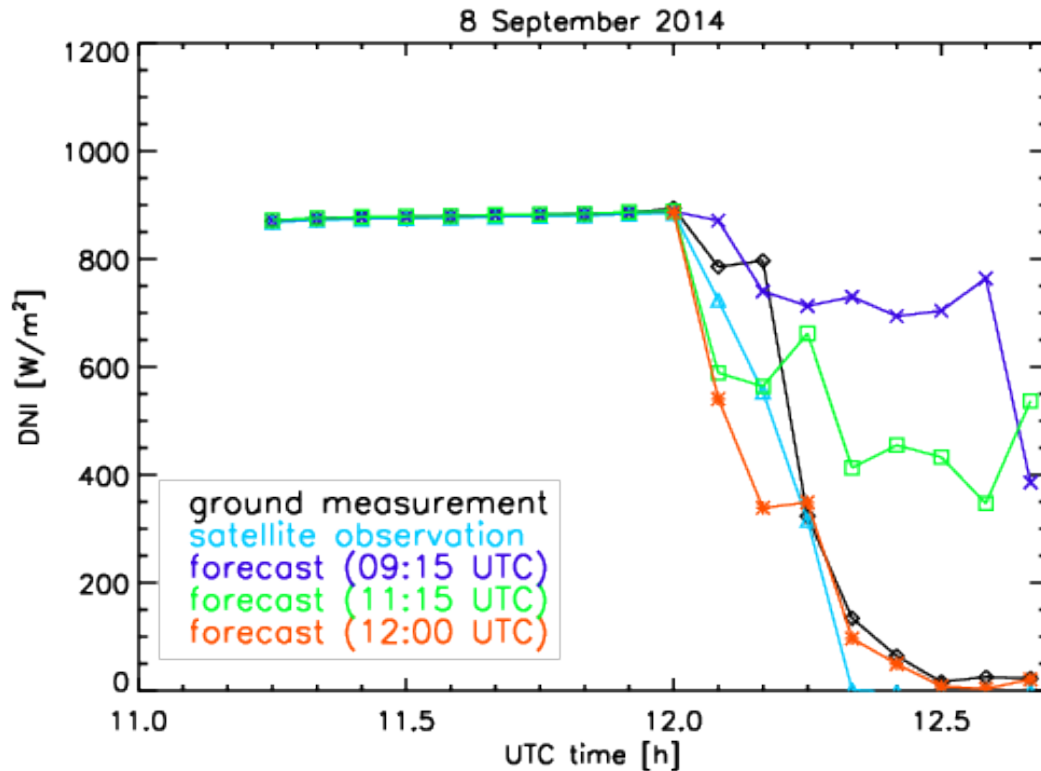


Figure 4.21: Measured (black curve) and satellite derived (cyan curve) DNI values for 8 September 2014, 11:15-12:40 UTC. Three Forecasts, started at 09:15 UTC (blue curve), 11:15 UTC (green curve) and 12:00 UTC (red curve), have been performed to show the accuracy for various forecast lead times.

up to 3 h.

For power plant operators following information is notable: 1) a thin cirrus cloud is reaching the PSA at approximately 12:05 UTC. 2) the forecasts for 09:15 and 11:15 UTC give the wrong indications that the amount of anticipated DNI is not reduced to less than 200 W/m^2 and can be still sufficient for an operation of the power plant without the use of storage or fuel.

4.4.4 25 June 2014

One great source of uncertainty in the forecast with satellites is the coarse resolution and thus the incapacity to detect small clouds or cloud holes. But the knowledge of this small-scale variability is essential for an optimized operation of CSP.

On 25 June 2014 small cumulus clouds develop during the day (Fig. 4.22) and are responsible for a high variability in DNI between 10:00 and 11:30 UTC - see DNI measurements in Fig. 4.23 (black curve). According to ceilometer data the cloud base height of these cumuli is around 2.1 km. With the satellite the single

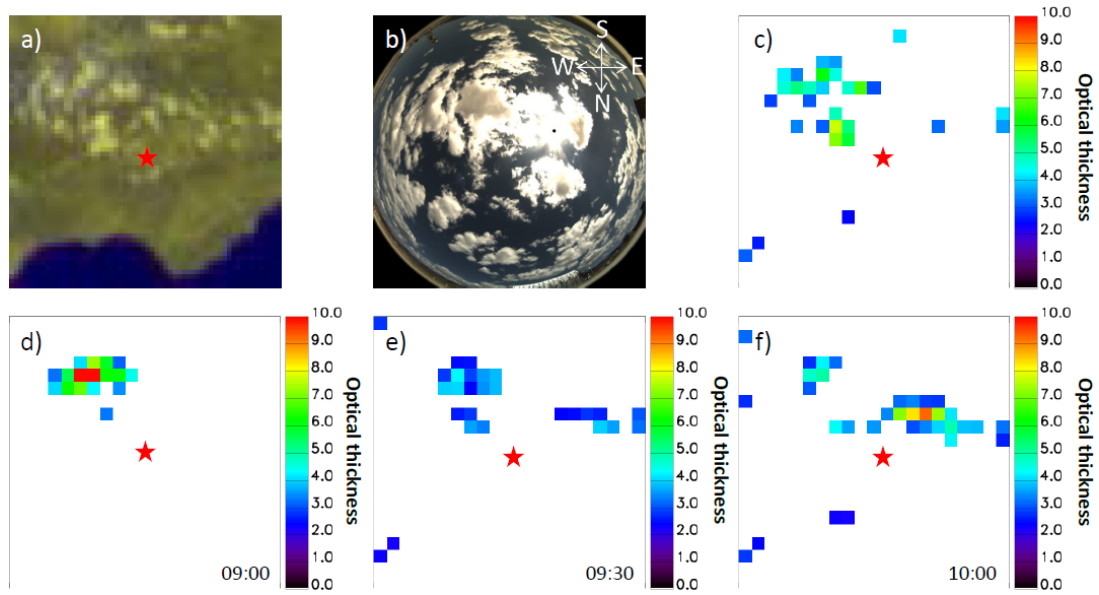


Figure 4.22: (a) False colour composite in high resolution, (b) camera image and total optical thickness derived by APICS and COCS for 25 June 2014, (c) 10:25 UTC, (d) 09:00 UTC, (e) 09:30 UTC and (f) 10:00 UTC. The red star marks the position of the PSA.

clouds cannot be distinguished because of the coarse resolution and a mean optical thickness for every pixel is derived. Furthermore, partial cloud cover makes cloud detection more difficult. Therefore, until 10:45 UTC no clouds are detected correctly, except at 10:15 UTC (Fig. 4.23, cyan curve), followed by a period of time with zero DNI until 11:20 UTC, when a thick cloud is observed by the satellite, but not measured by the pyrhelimeter. Afterwards a thick cloud is observed correctly until 11:45 UTC. There are indications of high variability, but not all clouds/cloud gaps can be observed by the satellite.

Next to spatial variability also atmospheric variability complicates the determination and forecast of DNI as constantly single clouds newly form or dissipate. Thus, all forecasts started at 09:00, 09:30 and 10:00 UTC are not able to predict the DNI variability between 10:00 and 10:30 UTC as these clouds, which cause the variability, have not developed yet, cannot be resolved due to their size or do not move (Fig. 4.22 d,e,f).

4.5 Systematic validation of DNI

Additionally to the verification of the nowcasting algorithm by examining the errors of the forecast against MSG/SEVIRI observations (Sect. 4.3), a validation against ground-based irradiance measurements and a comparison to two satellite-based nowcasting methods have been performed. These methods, like

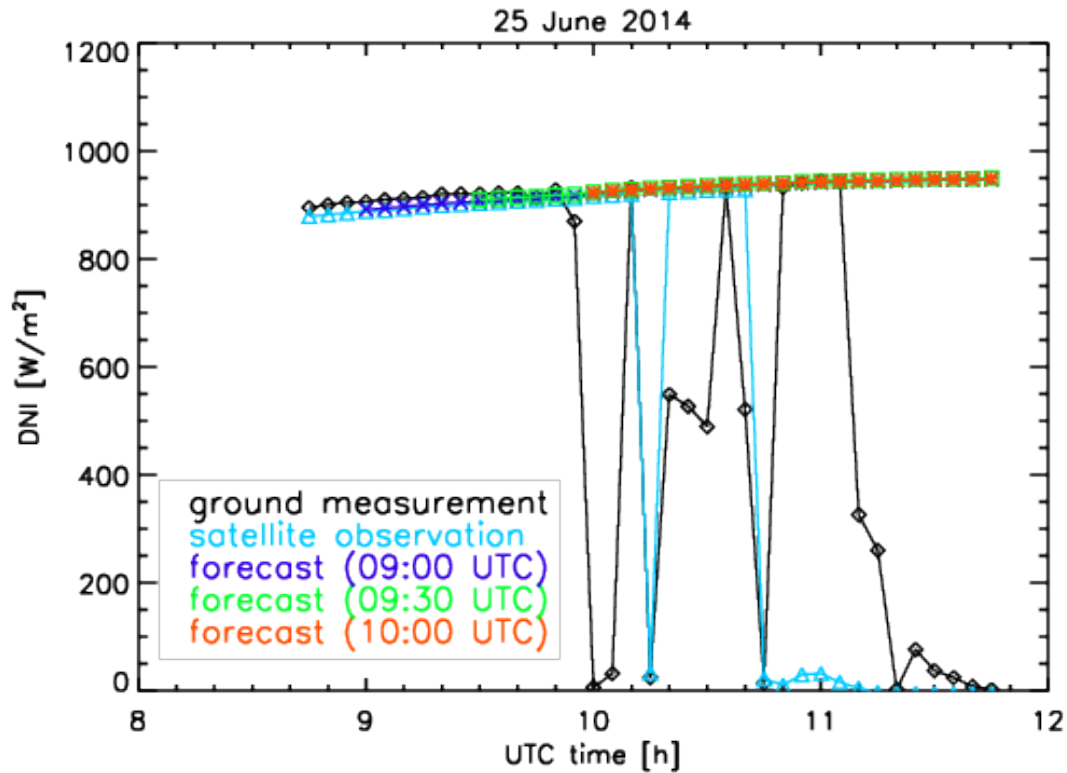


Figure 4.23: Measured (black curve) and observed (cyan curve) DNI for 25 June 2014, 08:45-11:45 UTC. Three forecasts, started at 09:00 UTC (blue curve), 09:30 UTC (red curve) and 10:00 UTC (green curve), have been performed to show the accuracy for various forecast lead times.

the presented algorithm (in the following referred to as PA), have been applied and refined in the EU project DNICast (www.dnicastproject.org) and have been described in Sect 3.5.

In order to examine the performance of each method the results of the forecasts are compared by means of selected cases (Sect. 4.5.1) and a statistical evaluation of all forecasts (Sect. 4.5.2). The ground measurements with a pyrheliometer (Sect. 3.3) at the PSA serve as reference value.

4.5.1 Selected cases

Fig. 4.24 shows the nowcasts for the DFD method (top), the MT method (middle) and the PA method (bottom) by means of a heatmap for 14 March 2013, a clear-sky day with a maximum DNI of $\sim 1050 W/m^2$. The ground measurements throughout the day are given as a horizontal bar at the top of the image with the colours representing the DNI values. The horizontal axis reflects the time of the day and the vertical axis the start of each forecast. Each horizontal bar represents a single forecast with increasing forecast lead time to the right and the forecast

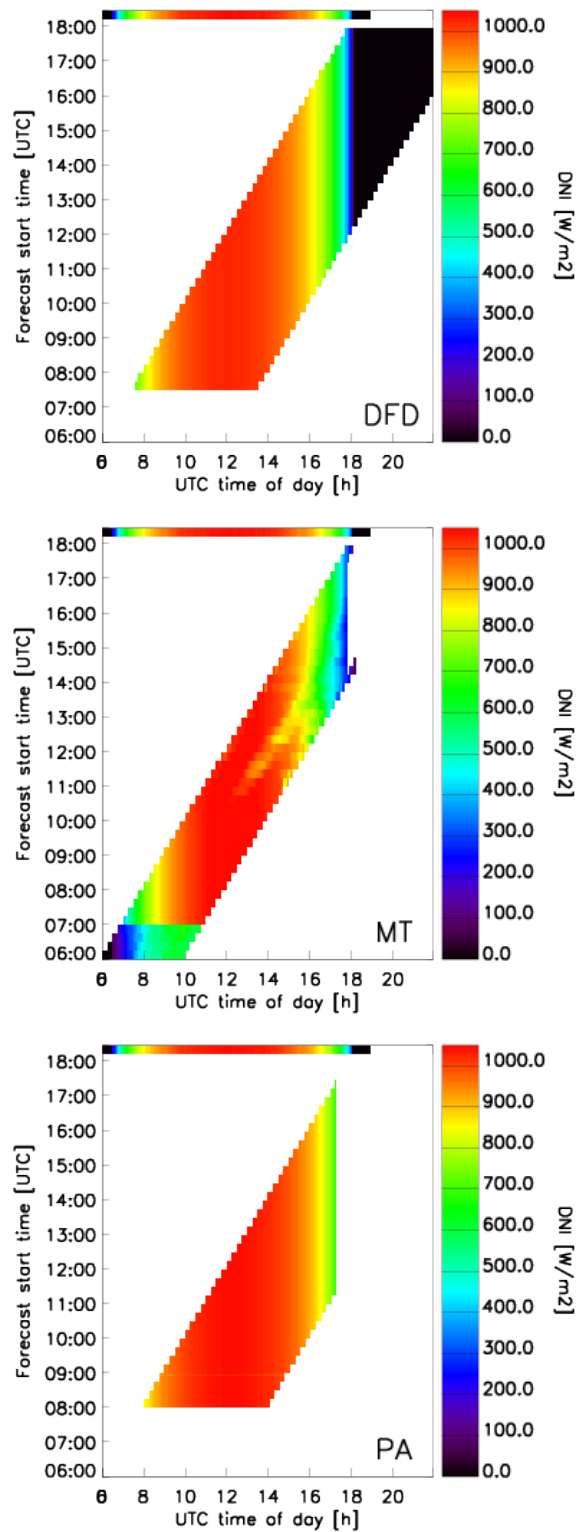


Figure 4.24: Nowcasts from DFD (top), MT (middle) and PA (bottom) for 14 March 2013. Ground measurements are given as the horizontal bar at the top of the image.

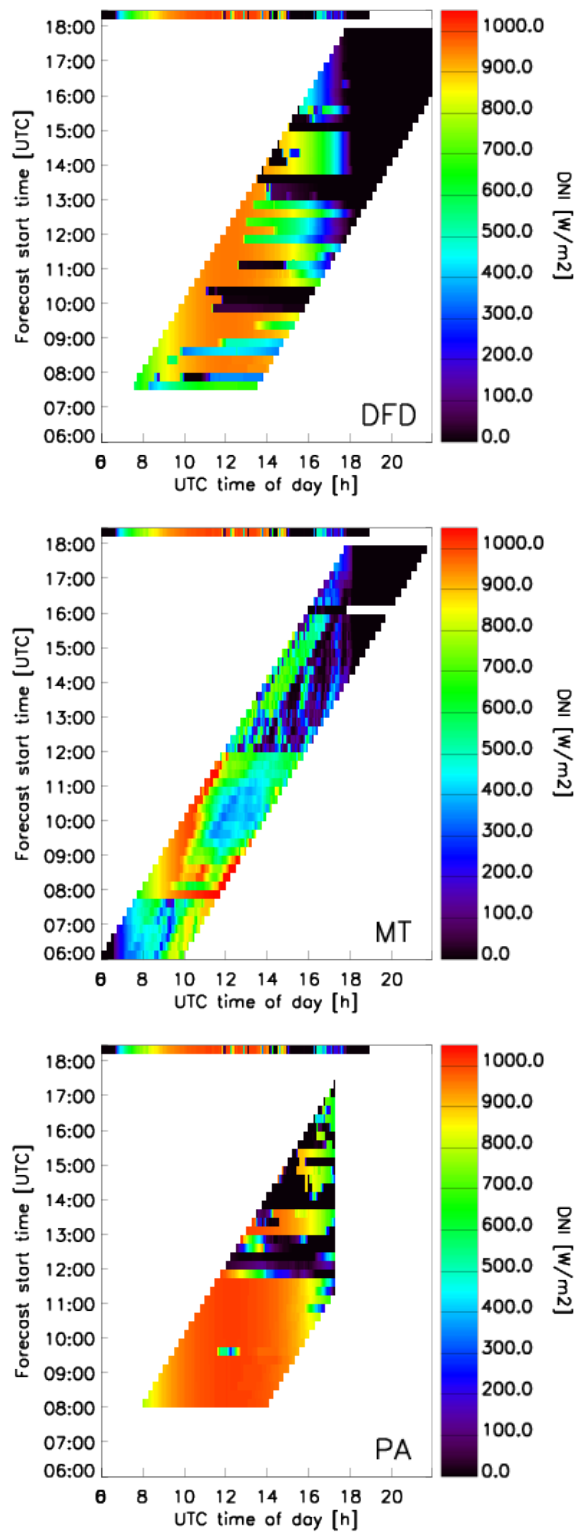


Figure 4.25: Nowcasts from DFD (top), MT (middle) and PA (bottom) for 11 March 2013. Ground measurements are given as the horizontal bar at the top of the image.

start time increases upwards. Thus, every vertical line shows all forecasts for a time of the day and these forecasts can be compared to the corresponding ground measurement. MT provide forecasts for 4 h, with a temporal resolution of 5 min, whereas DFD and PA have a forecast horizon of 6 h with a temporal resolution of 5 min up to 2 h, 15 min up to 4 h and 1 h up to 6 h (DNI values in between are determined by interpolation). MT provides forecasts directly after sunrise, while DFD and PA start when the zenith solar angle (sza) is smaller than 80° and 75° and stop when sza is higher than 80° and 75° , respectively, due to the fact that at high solar zenith angles optical and micro-physical properties of clouds are difficult to retrieve. For this reason, until 07:00 UTC the observed and forecasted DNI values of MT do not match the measured DNI, but all methods correctly predict the clear-sky conditions throughout the day except of MT, which forecasts reduced DNI in the afternoon.

On 11 March 2013 (Fig. 4.25) the conditions change during the day, with high DNI in the morning until 12:00 UTC, variable conditions at noon (12:00-14:00 UTC) and low DNI in the afternoon. PA correctly forecasts the high DNI in the morning, while DFD and MT predict some clouds and underestimate the DNI. All methods are not able to predict the high variability at noon for longer forecast lead times ($> \sim 2$ h), whereas the observations and short-term forecasts of DFD and PA partially capture the changes from high to low DNI. MT is not able to resolve the high variability at noon and gives medium DNI values, which can be explained in the following way. MT uses a clearness index, which has values between 0 and 1 depending on the cloud situation, whereas DFD and PA strictly separate between cloudy or cloud free pixel. So, for example, in case of high variability or at cloud edges, where a pixel can be partially cloudy, DFD and PA derive either maximum or zero DNI (without consideration of optical thin clouds), whereas MT gives medium DNI values. The low DNI values in the afternoon can be captured in some cases, but all methods overestimate the DNI in the remaining forecasts.

4.5.2 Statistical evaluation

The presented examples are meant to provide some insight in the typical behaviour of the three forecast methods. By means of statistical error metrics a systematic evaluation is done in this section. The examined period is from March to May 2013 and the forecasts are performed during daytime (solar zenith angle less than 80°) with a refresh rate of 15 min. First all forecasts are taken into account followed by a separation into different cloud types.

Error metrics

In general there are various reasons for errors/uncertainties in the DNI forecasts:

- errors/uncertainties in clear-sky models (aerosol load, water vapor etc.)
- errors/uncertainties in the forecast algorithms
- errors/uncertainties due to the coarse temporal/spatial resolution of the satellite

For calculating the uncertainties following error metrics have been used:

$$MBE = \frac{1}{N} \sum_{i=1}^N (DNI_{\text{pred},i} - DNI_{\text{meas},i}) \quad (4.24)$$

$$MAE = \frac{1}{N} \sum_{i=1}^N |DNI_{\text{pred},i} - DNI_{\text{meas},i}| \quad (4.25)$$

$$RMSE = \sqrt{\frac{1}{N} \sum_{i=1}^N (DNI_{\text{pred},i} - DNI_{\text{meas},i})^2}, \quad (4.26)$$

with the predicted DNI value $DNI_{\text{pred},i}$ and the DNI value $DNI_{\text{meas},i}$ measured at ground by the pyrheliometer. The Mean Bias Error (MBE) quantifies the general tendency of a forecast to over- or underpredict. The Mean Absolute Error (MAE) is a measure for the mean deviation between forecast and observation. The Root Mean Squared Error (RMSE) is more sensitive to large errors due to the squaring of individual errors and directly related to the standard deviation for normally distributed errors. These three error metrics are chosen because they are commonly used, widely known and recommended in literature for assessing solar forecasting accuracy [Lorenz et al., 2009, Zhang et al., 2015].

4.5.3 Comparison and validation of forecasted DNI for all cases

To provide an overview of the general performance of the methods the results for all forecasts have been compared against ground measurements. Fig. 4.26 shows the error metrics for a forecast horizon of 360 min for DFD (green curve) and PA (red curve) as well as for 240 min for MT (blue curve). MT provides forecasts for 4 h with a time step of 5 min, whereas DFD and PA have a forecast horizon of 6 h with a time step of 5 min up to 2 h, 15 min up to 4 h and 1 h up to 6 h due to requirements in DNICast. Note that the number of forecasts decrease with increasing forecast lead time as the forecasts are not available in the afternoon/evening because of the sunset.

The PA and DFD methods have a low MBE (solid curve) around zero with a maximum value of $\sim 20 W/m^2$ and $\sim -20 W/m^2$, respectively, which is a very good result, having in mind that the forecast horizon is 6 h. The small MBE shows that there is no strong tendency for both methods to over- or underestimate the

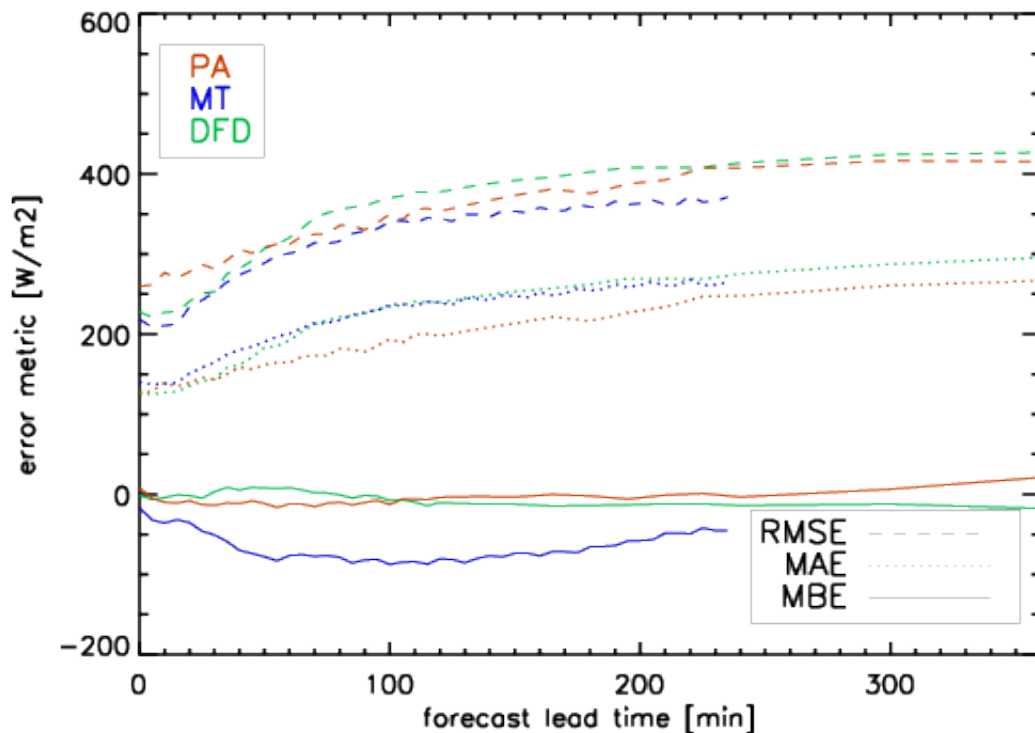


Figure 4.26: Error metrics for all cases for PA (red), MT (blue) and DFD (green).

DNI. In contrast to that, the MT method has a high negative MBE starting at $t=0$ with -25 W/m^2 , increasing to a maximum value around -90 W/m^2 for a forecast lead time of 100 min and decreasing afterwards to -50 W/m^2 after 240 min. The forecasts provided by MT are thus underestimating the DNI in general. The MAE (dotted curve) continuously increases with forecast lead times for all methods. PA and DFD show similar results up to 40 min (rising from 125 to 160 W/m^2) with a stronger increase of DFD afterwards and thus approximating MT. The MAE of DFD and MT is $30 - 60 \text{ W/m}^2$ higher than for PA (maximum of 265 W/m^2 after 360 min) for a forecast lead time larger than 60 min, which means that individual deviations of forecasted DNI from actual individual measured DNI are larger for MT and DFD. In case of the RMSE the results are reversed as MT shows the lowest errors with a minimum of 215 W/m^2 at $t=0$ and a maximum of 370 W/m^2 after 240 min. PA and DFD show only small differences (up to $\sim 40 \text{ W/m}^2$) throughout all forecast lead times with maximum values of 410 W/m^2 for PA and 430 W/m^2 for DFD after 360 min.

Having in mind that the MT method has a higher MBE and MAE, this low RMSE is remarkable. A likely reason for that is the mentioned usage of clearness index and the derivation of medium DNI values for situations with high variability, where DFD and PA determine maximum or zero DNI values. Those cases result in stronger deviations, which increase especially the RMSE as it is very sensitive to large errors. In the numerical weather prediction verification theory on various

spatial scales this effect is known as 'double penalty' effect. Although this method is leading to a smaller RMSE, it is not useful for power plant operators as the predicted DNI values are wrong and the information about the high variability in DNI is lost.

Overall, both MAE and RMSE increase with forecast lead time due to rising errors/uncertainties in the forecast algorithms. This is mainly caused by the nonlinearity of atmospheric motion and the creation and dissipation of clouds, which is not modeled explicitly.

4.5.4 Comparison and validation of forecasted DNI with respect to cloud types

To obtain a deeper insight about the reasons of the presented results all cases have been split into three categories: 1) clear sky, 2) thin clouds and 3) thick clouds. Pixels with thin clouds are those classified as thin cirrus clouds by COCS (see Sect. 4.1.1) after parallax correction (Sect. 4.4.1), whereas thick clouds are those pixels which have been classified as water clouds or multi-layer clouds. In total there are 2160 clear-sky, 1185 optically thick cloud and 481 optically thin cloud cases, which have been evaluated separately in the following. Additionally to the proposed error metrics a relative error [%] - errors are divided by the average DNI_{meas} - is added to take into account the different amount of DNI for the three categories in comparison to the errors. Thus, the same absolute error values result in higher relative errors if the average DNI_{meas} is lower.

For clear-sky cases (Fig. 4.27, top) DFD and PA show a similar behaviour in the MBE with increasing negative values with forecast lead time. The MBE for DFD is higher than for PA (maximum values of $-120 W/m^2$ (17%) and $-70 W/m^2$ (10%), respectively) except for the first 20 min, where PA has a slightly positive MBE and DFD is around zero. The relative error is quite low due to the high DNI for clear sky. MT starts with a MBE of $-50 W/m^2$ (7%) rising to $-200 W/m^2$ (20%) at 100 min forecast lead time. Afterwards a slightly reduction of $10 - 20 W/m^2$ can be observed. This behaviour points towards deficiencies in the clear-sky model used by MT. By definition of the MBE the DNI for clear-sky cases is in general underestimated, which can be explained by the direction of the potential wrong forecast. Errors in the atmospheric parameters, i.e. water vapor and aerosol load, lead to positive and negative deviations from the ground measurements of DNI, but the effect of inaccurate aerosol load and amount of water vapor is moderately low. In case a clear-sky situation is predicted as cloudy by the forecast methods, the DNI will always be lower than in the ground measurements, thus showing a negative MBE. With increasing forecast lead time the probability of such a wrong forecast is increasing.

The rising inaccuracy of the forecasts with forecast lead time is also the reason for the increase of MAE (dotted line). The MT method has high MAE, ranging from 140 (19%) to $270 W/m^2$ (34%) due to deficiencies in the clear-sky model.

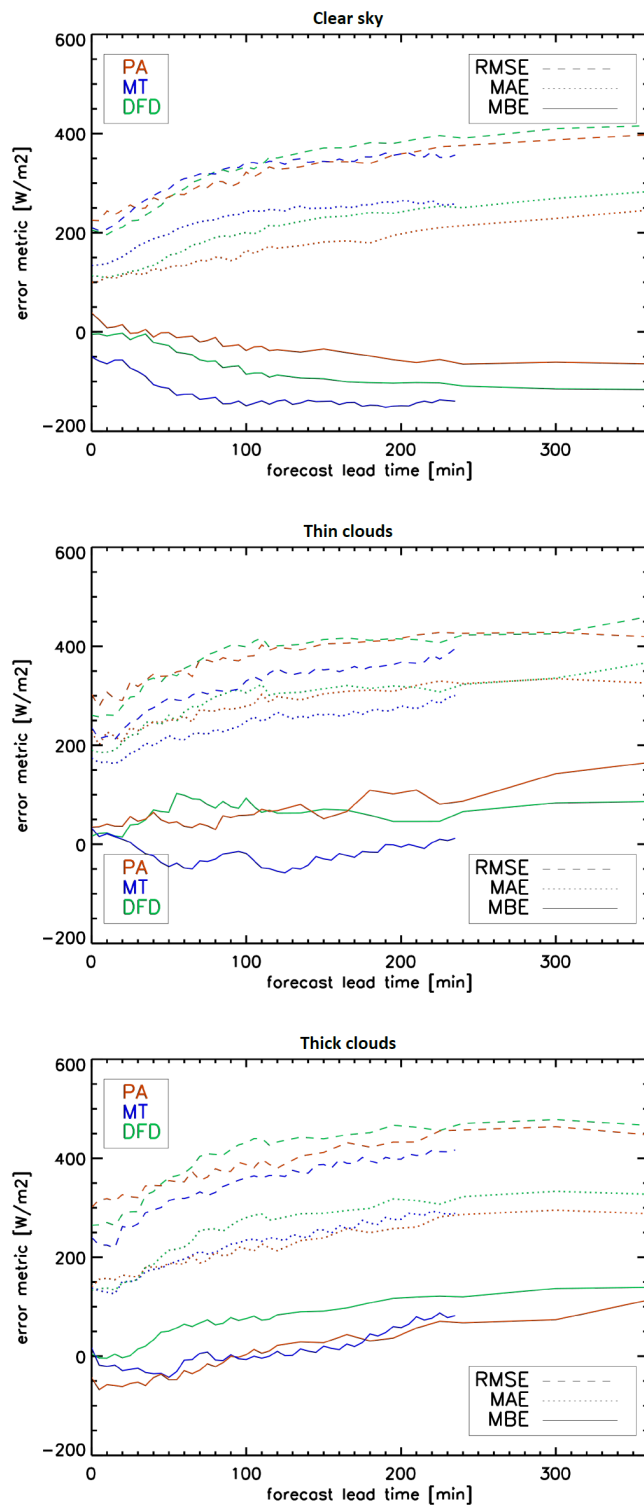


Figure 4.27: Error metrics for clear sky (top), thick clouds (middle) and thin ice clouds (bottom).

DFD and PA show a similar behaviour until 40 min forecast lead time, both start at $\sim 100 W/m^2$ (14%), with a stronger increase of DFD afterwards reaching maximum values of $280 W/m^2$ (42%) and $240 W/m^2$ (37%) after 6 h for DFD and PA, respectively. The RMSE is similar for all methods up to a forecast lead time of ~ 140 min, starting at $200 - 230 W/m^2$ (28-30%) and rising up to $340 - 370 W/m^2$ (45-47%). Afterwards DFD has a $20 - 50 W/m^2$ higher RMSE than PA and MT with maximum values of $360 W/m^2$ (47%) after 240 min for MT and $390 W/m^2$ (51%) after 360 min for PA.

For optically thick clouds (Fig. 4.27, bottom) a positive MBE increasing over forecast lead times for all methods is observed except for the first 100 min for MT and PA (negative MBE), which show similar behaviour throughout all forecast lead times. The MBE for DFD is $30 - 90 W/m^2$ higher except for the first 30 min (MBE around zero). The explanation for the positive MBE is analogous to the clear-sky cases, but with reversed conditions. In these cases, the situations with thick clouds are wrongly predicted as clear-sky or thin clouds resulting in an overestimation of DNI and thus a positive MBE. The MAE is very similar up to 40 min for all methods - starting at $\sim 130 W/m^2$ (69%) and rising to $\sim 180 W/m^2$ (90%). Afterwards DFD shows a stronger increase up to $330 W/m^2$ (170%) after 360 min, which is about $40 W/m^2$ higher than for PA. MT and PA have a similar behaviour with a maximum of $250 W/m^2$ (140%) for MT after 230 min. The relative error is considerably higher compared to clear-sky due to the low DNI values for optically thick clouds. Regarding the RMSE MT has lower values than DFD and PA, which is, as mentioned, caused by the higher sensitivity of the RMSE to rare, but large errors. The RMSE of PA is slightly higher ($0 - 40 W/m^2$) than for DFD for a forecast lead time up to 50 min. Afterwards the RMSE for DFD is increasing stronger reaching a maximum of $480 W/m^2$ (250%), whereas the maximum for PA is around $460 W/m^2$ (244%).

For optically thin clouds (Fig. 4.27, middle) the MBE for MT has low values close to zero ($[-50, 30] W/m^2$ (12%)), whereas for DFD and PA the MBE is positive ranging from $20 W/m^2$ (4%) and $40 W/m^2$ (7%) to maximum values of $100 W/m^2$ (22%) and $160 W/m^2$ (42%), respectively. According to the definition of the MBE, DFD and PA in general overestimate the DNI and thus underestimate the optical thickness of the cirrus clouds. The MAE and RMSE is lowest for MT and increases with forecast lead time to a maximum of $300 W/m^2$ (63%) and $390 W/m^2$ (83%), respectively. DFD and PA show a similar behaviour for both error metrics except for the first 20 min, when DFD is lower than PA, and for the last hour, when DFD reaches higher values.

Summarising, in clear-sky cases the errors of PA are mainly lowest, which indicates deficiencies in the clear-sky models of DFD and especially MT. For thin clouds MT performs best, which points out inaccuracy in the determination of cirrus cloud optical thickness for DFD and PA. In case of thick clouds MT and PA show a similar behaviour except for the lower RMSE for MT due to the 'double penalty' effect for PA. In general, both MAE and RMSE increase with forecast lead time up to 3-4 hours due to rising errors/uncertainties in the forecast al-

gorithms caused by the nonlinearity of atmospheric motion and the creation and dissipation of clouds. For the forecasts with longer lead times the errors are nearly constant in most cases - an indication that the forecasts are approximating a statistical value. Therefore, a forecast for more than 3-4 hours can be performed, but the results should be treated with caution.

It should be kept in mind that MT performs a post processing by means of onsite measurements of DNI, thus having an advantage over the DFD and PA method due to more exact initial conditions. With an implementation of ground measurements the errors of the DFD and PA method could be reduced.

4.6 Conclusions

The performance of the nowcasting algorithm is assessed in terms of common error statistics, forecasting skill over persistence, where a doubling of lead time is found, and also in terms of a comparison to two satellite-based forecasting methods. This comparison confirmed the good performance of the clear-sky model and the forecasting algorithm, but also points out inaccuracy in the determination of cirrus cloud optical thickness. An evaluation over two months with different cloud coverage and cloud types and three case studies showed the dependence of the performance of the algorithm for different meteorological situations. For widely distributed, homogeneous clouds the spatial resolution of MSG/SEVIRI is sufficient to determine the DNI due to its low variability. Those cases show the good performance of the forecast algorithm for advective clouds with approximately constant velocity, but also the challenges in predicting accurate cloud optical properties when cloud properties evolve with time - see period in March (Sect. 4.3) and the second case study (Sect. 4.4.3). In case of convective clouds, the limitations of DNI forecasts for longer lead times can be observed - see period in July (Sect. 4.3) and the first case study (Sect. 4.4.2). Due to small-scale variability in the atmosphere a forecast for a lead time of more than one hour is not able to predict the correct time of arrival or accurate optical properties of a cloud. The third case study (Sect. 4.4.4) clearly demonstrates the limitations of observing and nowcasting DNI with satellites due to their coarse spatial resolution. Small-scale variability as well as changing cloud optical properties due to atmospheric microphysical processes can make satellite-based forecasts useless for CSP operators within a short period of time under certain conditions. One possibility to improve the performance of the forecasts could be the implementation of the channel with higher spatial resolution, the HRV (Sect. 5), or of all-sky imagers with their higher spatial and temporal resolution (Sect. 6).

Chapter 5

Synergistic use of high and low resolution MSG/SEVIRI data for an improved cloud and DNI forecast

As mentioned in Sect. 3.1.1 the SEVIRI imager aboard MSG has a broadband high resolution visible (HRV) channel in a spectral range of about $0.4 - 1.1 \mu\text{m}$ (Table 3.1). The sampling distance is 1 km (referred to as HRES) instead of 3 km (referred to as LRES) at sub-satellite point allowing a more detailed observation of the earth for a part of the disc (see Fig. 3.1). Because of the Earth's shape and the slant view this spatial resolution is reduced when observing regions north or south of the equator. For the investigated area around the PSA a resolution of approximately $1.1 \text{ km} \times 1.4 \text{ km}$ ($3.2 \text{ km} \times 4.3 \text{ km}$ in low resolution) can be calculated.

To illustrate the benefit of the higher spatial resolution of the HRV Fig. 5.1 shows the reflectivity of the SEVIRI channel centred at 600 nm (a) and of the HRV (b) for a scene over the Iberian Peninsula. Pixels with high reflectivity indicate cloudy pixels. By comparison of the images more details and finer cloud structures can be seen in case of the HRV and additionally small-scale clouds, which could not be resolved in low resolution. For this, a detection of clouds and the derivation of their properties in high resolution could result in a significant improvement of the nowcasting of clouds and thus DNI. Small-scale variability, e.g. cumuli, which leads to partial shading of the power plant, as well as exact determination of start-up and shut-down times due to cloud movement could be derived more accurately.

As only one channel in high resolution is available the standard method from Sect 3.1.1 cannot be applied and additional data are required for the determination of cloud optical properties. To this end, a synergistic exploitation of high and

low resolution together with radiative transfer calculations has been applied in order to derive cloud mask (Sect. 5.1.2) and cloud optical properties (Sect. 5.2). The benefits and limitations of the forecasts in high resolution are illustrated via three case studies (Sect. 5.4). Additionally, a systematic validation with surface DNI is shown together with a comparison to the forecasts in low resolution (Sect. 5.5). All forecasts are performed with data from the MSG satellite operating in rapid-scan-mode (located at 9.5° East) in order to use the higher repetition rate.

5.1 Synergistic cloud mask

5.1.1 Challenges

The HRV channel is a solar channel and no thermal information is available at this resolution. Therefore, the detection of thin cirrus clouds with this channel alone is very difficult. Additionally, the cloud optical thickness cannot be determined in the usual way with the method described by Nakajima and King [1990] because of missing near-infrared information. To this end, a synergistic exploitation of high and low resolution together with radiative transfer calculations has been applied in order to derive cloud mask (Sect. 5.1.2) and cloud optical properties (Sect. 5.2).

For this, the following issues must be considered: 1) The HRV is a broadband channel ranging from 0.4 – 1.1 μm and hence covering the vegetation’s red edge - a surface albedo in this spatial resolution for this spectral range is not available. 2) The calibration of the HRV is not monitored regularly by EUMETSAT as the focus lies on the low resolution channels. 3) The geolocation and the inter-channel registration is not very precise so that the single pixels are not congruent for all channels.

5.1.2 HRV cloud detection

The aim is to derive a HRES cloud mask that is consistent with the LRES cloud mask and that can improve at least the detection of small-scale clouds, that have been shown in Sect. 4.4 to represent a challenge for the determination and forecast of DNI. The procedure works in three steps. In a first step a clear-sky reflectivity $R_{\text{cs}}(\text{HRV})$ for the HRV is constructed by determining the reflectivities for 600 nm $R_{\text{cs}}(\text{VIS600})$ and 800 nm $R_{\text{cs}}(\text{VIS600})$ at TOA (top of atmosphere) for clear sky. For this, the radiative transfer model libRadtran [Mayer and Kylling, 2005, Emde et al., 2016] is used to calculate look-up tables of clear-sky reflectivities given sun

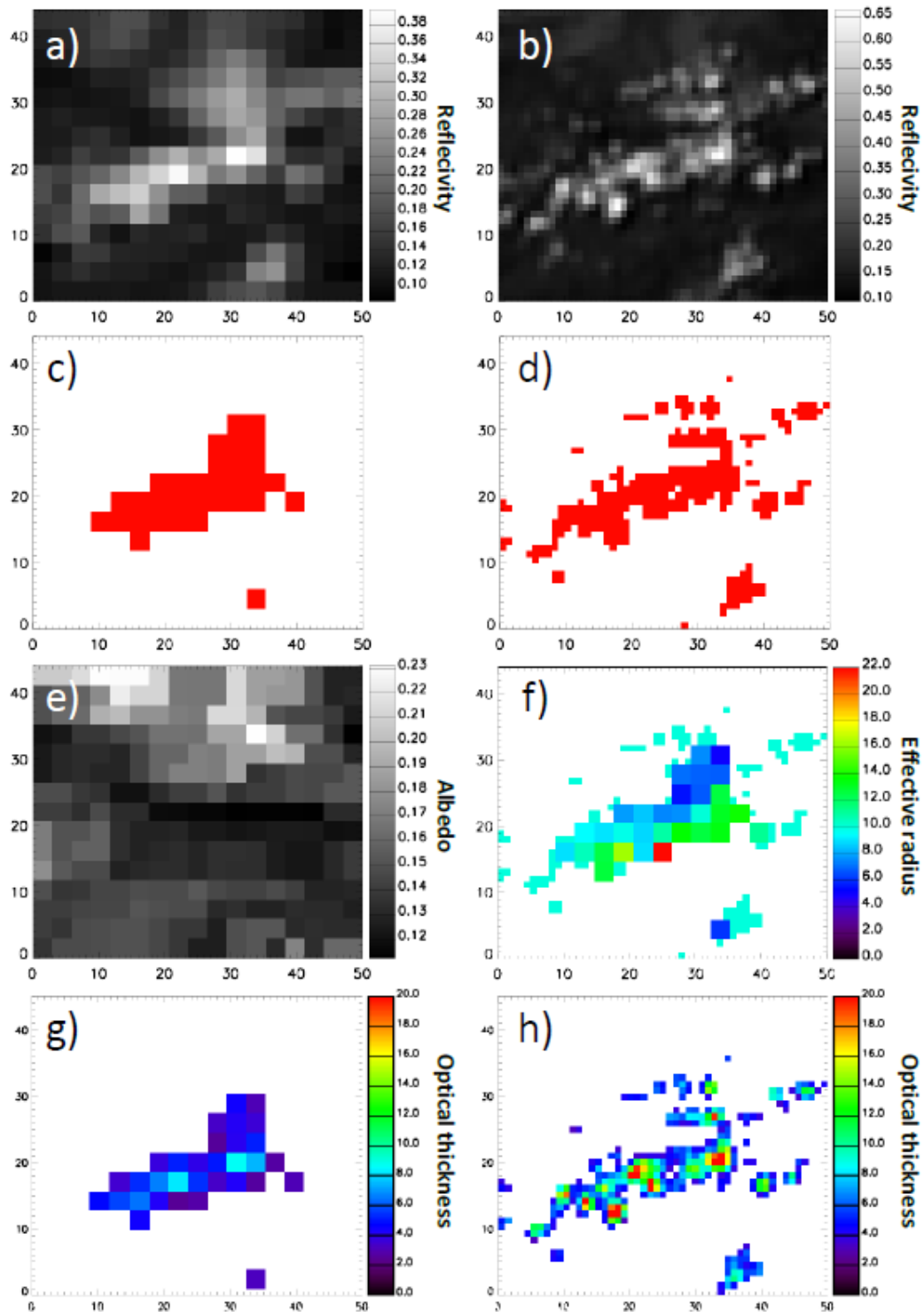


Figure 5.1: (a) Reflectivity for 600 nm and (b) of the HRV for a scene over the Iberian Peninsula. The derived cloud mask in (c) low and (d) high resolution, (e) the albedo for 600 nm, (f) the effective radius in high resolution as well as the optical thickness in (g) low and (h) high resolution.

and satellite geometry as well as the surface albedo. Surface albedo is then taken from the black sky albedo product from MODIS (Moderate-resolution Imaging Spectroradiometer) MCD43C1 [Schaaf et al., 2002], available in 0.05° resolution. A mid-latitude standard atmosphere [Anderson et al., 1986] is used here, so the dependence of reflectivity on water vapor and ozone is neglected at this stage. A pre-requisite for this work is an adjustment of the geolocation accuracy for MSG and MODIS by shifting the MODIS data and quantifying the correlation between both data sets.

With these reflectivities $R_{cs}(HRV)$ has been approximated [Deneke and Roebeling, 2010] by

$$R_{cs}(HRV) = a * R_{cs}(VIS600) + b * R_{cs}(VIS800), \quad (5.1)$$

where a and b are fit coefficients determined by least-squares linear regression and the obtained annually averaged parameters are 0.667 ± 0.025 for a and 0.368 ± 0.020 for b . Notice that $R_{cs}(HRV)$ is in low resolution.

In order to determine cloudy pixel in low resolution the difference of this calculated clear-sky reflectivity and the observed reflectivity from SEVIRI is examined. To clarify the functionality of the subsequent procedure Fig. 5.2 illustrates an example of the distribution of HRES pixels in one LRES pixel. For every

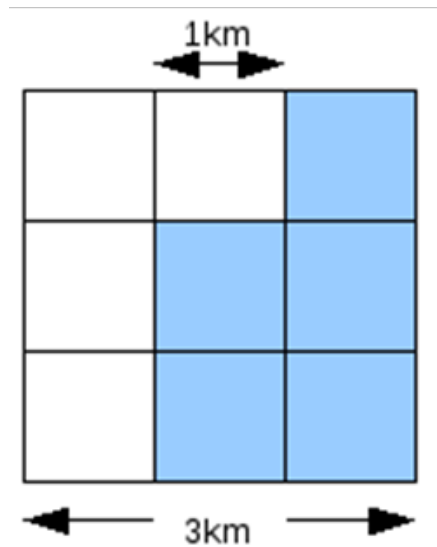


Figure 5.2: Example of the distribution of HRES pixels ($1 \text{ km} \times 1 \text{ km}$) in one LRES pixel ($3 \text{ km} \times 3 \text{ km}$).

scene the observed HRES reflectivities are averaged over the corresponding nine pixels to obtain mean HRV reflectivities $R_{3 \times 3}(HRV)$ in LRES. The difference of $R_{3 \times 3}(HRV)$ and the LRES reflectivity $R_{cs}(HRV)$ calculated with Eq. 5.1 is determined for every pixel and a threshold value c for the determination of cloudy pixels is derived: a pixel is cloudy if the observed $R_{3 \times 3}(HRV) > R_{cs}(HRV) + c$. The threshold value is chosen in a way that $\sim 97\%$ of the cloudy pixels detected by APICS and COCS, which are supposed to be the LRES truth, have values

higher than $R_{cs} + c$ to minimise a wrong classification.

In a second step the threshold c for LRES pixels is then applied to the HRES reflectivities $R(HRV)$: a pixel is cloudy if $R(HRV) > R_{cs}(HRV) + c$. An example of a cloud mask in high resolution is shown in Fig. 5.1 d. When compared to the cloud mask in low resolution (Fig. 5.1 c) the finer structures of the clouds as well as additionally small clouds can be observed in high resolution.

Due to the lack in thermal information the detection of thin ice clouds below an optical thickness of ~ 1.5 is not reasonable as the uncertainties are too large. For these pixels the LRES cloud mask is used (third step). This procedure is performed for every image because $R_{cs}(HRV)$ varies for each scene. Furthermore, because of different absolute values and gradients in surface albedo the described method is applied for land, sea and coasts separately. Best results can be achieved for sea as the surface albedo is homogeneous and quite low compared to cloud albedo. As a consequence, more cloudy pixels and pixels with thinner clouds can be determined compared to pixels over land and coasts, where absolute values and gradients in surface albedo are considerably higher.

5.1.3 HRV cloud classification

As shown in Sect. 4 the forecast is performed for low level and high level clouds separately. In order to operate this technique for the high resolution forecast procedure the derived HRES cloud mask must be split into upper and lower cloud masks according to Sect. 4.1.1. HRES Pixels, which have been classified as upper and/or lower clouds in low resolution, are assumed to be upper and/or lower clouds, respectively. Small clouds, which have not been detected in low resolution, are assumed to be lower clouds due to the fact that upper ice clouds usually exhibit a large spatial extent and can thus be observed in low resolution.

5.2 Synergistic cloud optical properties

The approach of the APICS algorithm using one near-infrared (NIR1.6) and one visible (VIS600) channel to derive effective radius and optical thickness cannot be applied in high resolution as only one channel is available. Thus, we adapt this method to provide consistent optical thickness in HRES. To this end, the cloud optical thickness of the clouds detected in high resolution (Sect. 5.1.2) is derived from look-up tables (LUTs), which have been computed with the radiative transfer model libRadtran. Therefore, parameters in low resolution have been adapted to provide a reasonable optical thickness to the forecast algorithm. The input data for the LUTs are HRES reflectivity, albedo, effective radius, sun and satellite geometry. Additionally, a recalibration factor is applied, which is

introduced in this chapter.

5.2.1 Input parameter

Albedo

An albedo in this spatial resolution for this spectral range is not available. For this, the albedo A has been approximated by

$$A(\text{HRV}) = a * A(\text{VIS600}) + b * A(\text{VIS800}), \quad (5.2)$$

with the coefficients $a=0.667$ and $b=0.368$. Fig. 5.1 e shows the derived albedo $A(\text{HRV})$ for the scene described in Sect. 5.1. $A(\text{HRV})$ is assumed to be constant over 3×3 HRES pixels.

Effective radius

Because of missing near-infrared information in high resolution the optical thickness and the effective radius cannot be derived with the HRV. Therefore, the effective radius determined in low resolution is used as input parameter for the LUTs. In case no effective radius in low resolution is available for HRES cloudy pixels, which have not been detected in low resolution, a fixed value of $10 \mu m$ for water clouds is assumed. This assumption can lead to an uncertainty in optical thickness up to 20% when compared to calculations with the minimum and maximum effective radius of $5 \mu m$ and $30 \mu m$, respectively. An example for the effective radius is displayed in Fig. 5.1 f for the scene described in Sect. 5.1.

HRV reflectivity

The solar channels of MSG/SEVIRI are not calibrated onboard and therefore a vicarious calibration must be performed. Meirink et al. [2013] presented a method for the inter-calibration of geostationary and polar-orbiting imager solar channels based on regressions of collocated near-nadir reflectances. With this method the solar channels of MSG/SEVIRI have been calibrated with corresponding channels of MODIS and the derived recalibration factors are $F_{0.6} = 1.087$ for $0.6 \mu m$ and $F_{1.6} = 0.966$ for $1.6 \mu m$, which are multiplied with the measured reflectivities of MSG/SEVIRI to get the calibrated reflectivities. For the HRV no recalibration factor has been determined in this work. Thus, we applied another method to produce consistent optical thickness. For this, the LRES optical thickness derived by APICS and COCS with the two recalibration factors $F_{0.6}$ and $F_{1.6}$ is compared

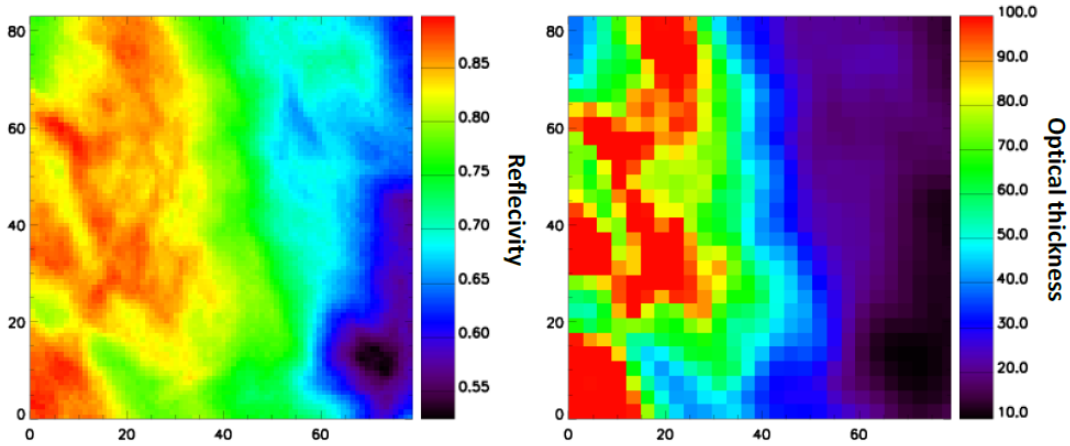


Figure 5.3: (left) HRES reflectivity and (right) 3×3 averaged HRES cloud optical thickness for a selected cloud scene in the tropics.

to the HRES optical thickness derived with LUTs. A calibration factor for the HRV F_{HRV} is determined in the following.

In order to enable the comparison, the HRES optical thickness has to be reduced to low resolution. For this, the observed reflectivities of 3×3 HRV pixels are averaged and the cloud optical thickness is derived with $F_{\text{HRV}} = 0.9$ as a first guess. Fig. 5.3 (left) shows the HRV reflectivity for a selected cloud scene in the tropics and the corresponding 3×3 averaged HRES cloud optical thickness. To reduce uncertainties a relatively homogeneous scene has been chosen.

F_{HRV} is varied in steps of 0.05 until the minimum MAE (see Sect. 4.5.2) between

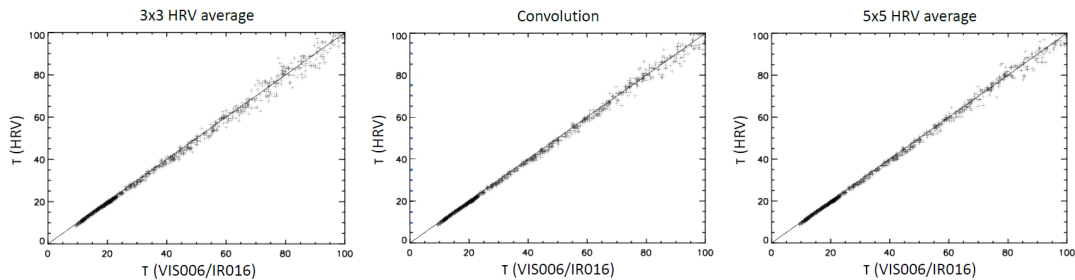


Figure 5.4: Scatter plot of derived optical thickness in low and high resolution for a recalibration factor of 1.048 for the scene depicted in Fig. 5.3: (left) without convolution and averaged over 3×3 HRES pixels, (middle) with LRES convolution and (right) without convolution and averaged over 5×5 HRES pixels.

the optical thickness in high and low resolution is achieved. Fig. 5.4 (left) depicts the distribution of the derived optical thickness in low ($tau_{\text{VIS006/VIS016}}$) and high (tau_{HRV}) resolution for each pixel in the cloud scene. With a calibration factor F_{HRV} of 1.048 the HRES and LRES optical thicknesses are comparable with deviations up to 10% for this scene. One source for these deviations are uncertainties due to atmospheric gas extinction (described in Sect. 5.2.2), which lead to errors

in the derivation of optical thickness. Another reason is the spatial response of the SEVIRI detectors [EUMETSAT, 2006], so that contributions of surrounding pixels influence the observed reflectivities in each pixel (Sect. 3.1.1) and in order to exactly compare HRES and LRES optical thickness this influence must be considered.

First, a deconvolution is applied to the HRES reflectivity to consider the influence of the PSF for high resolution. In a second step, the HRES pixels are convoluted with the PSF for low resolution. The consistency between HRES and LRES optical thickness increases, recognizable by the narrower distribution (Fig. 5.4, middle) and a higher correlation coefficient. As the application of two convolutions is difficult and computationally expensive the reflectivity of 5×5 instead of 3×3 averaged HRES pixels (see Fig. 5.4, right) is used for the comparison, which is faster and produces similar results, i.e. the same correlation coefficients.

The described procedure is executed for every scene as F_{HRV} varies. After applying the recalibration factor the optical thickness in high resolution can be determined. Fig. 5.1 shows the optical thickness in low (g) and high (h) resolution. In HRES the high variability in cloud optical thickness as well as the finer structures of the clouds and also small clouds can be detected confirming the expected benefit by using a channel with a higher spatial resolution.

5.2.2 Uncertainties: atmospheric gas extinction

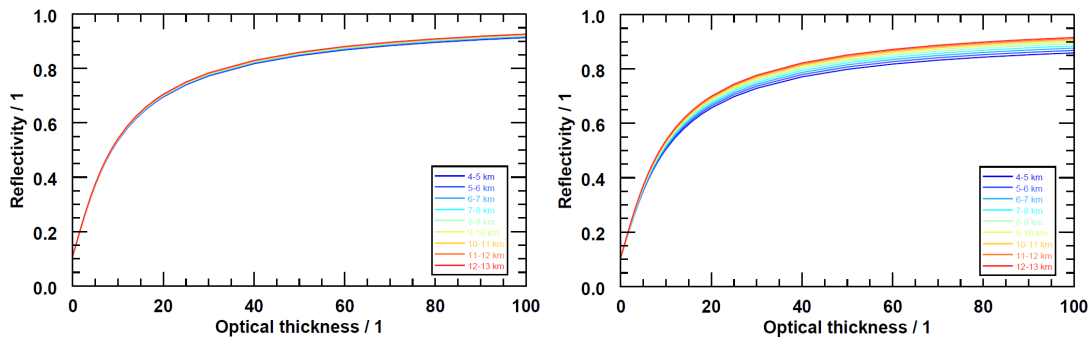


Figure 5.5: VIS006 (left) and HRV (right) reflectivity for optical thicknesses between 0 and 100 for various cloud top heights in the atmosphere.

On its way through the atmosphere radiation interacts with matter (molecules and particles) in the atmosphere by scattering and absorption, which inter alia depend on wavelength (see Sect. 2.2). Only a few weak absorption bands (ozone and water vapor) occur in the range which is covered by the SEVIRI channel VIS006 ($0.56\text{-}0.71\ \mu\text{m}$). In contrast water vapor absorption bands within the wide spectral range covered by the HRV ($\sim 0.4\text{-}1.1\ \mu\text{m}$) influences the radiation on its way through the atmosphere. This leads to a height dependence of the observed reflectivity when a thick cloud is present at different levels as the reflected radiation is lower for lower cloud top heights due to the longer paths and thus

more absorption through the atmosphere. With increasing optical thickness the cloud shields the lower part of the atmosphere. This effect also depends on the sun geometry due to its influence on the length of the path through the atmosphere. Fig. 5.5 shows the VIS006 (left) and HRV (right) reflectivity for optical thicknesses between 0 and 100 for various cloud top heights in the atmosphere with a cloud geometrical thickness of 1 km. In case of the VIS006 the reflectivities for the single cloud top heights differ by 2-3%, while these differences are much larger for the HRV (up to 10%), thus, confirming the higher influence of atmospheric extinction on the broadband channel. The figure has been created with the radiative transfer model libRadtran for an albedo of 0.1 and a standard atmosphere for mid-latitude summer [Anderson et al., 1986].

To quantitatively calculate the influence of this effect on the reflected radiation an exact knowledge of the cloud top height and the concentrations of the absorbers, i.e. water vapor as the strongest absorber, would be necessary. No information about these parameters, except for cloud top height for ice clouds from COCS, is available and their derivation, e.g. by NWP models, would be time-consuming and computationally expensive, which is a limiting factor for nowcasting methods as forecasts have to be available in the short term. And as also the uncertainties would still be high, the influence of atmospheric extinction is not implemented in the derivation of optical thickness.

5.3 Forecast in high resolution

The forecast in high resolution is performed with the method described in Sect. 4 applied to HRES data. For this the derived HRES cloud optical thickness is split into upper and lower clouds by means of the HRES cloud phase mask (Sect. 5.1.2). In case of multi-layer clouds the percentage of upper and lower clouds on the total optical thickness in low resolution is determined and is applied to the HRES total optical thickness to obtain the amount of optical thickness for the upper and lower clouds in high resolution. The HRES disparity vector field $\vec{V}_{A \rightarrow B}$ between the initial images A and B separated by a time interval $\Delta t = 15$ min is determined by the pyramidal matcher (Sect. 3.4) and the object classification (Sect. 4.2.2), the interpolation of cloud-free background motion (Sect. 4.2.3) as well as the optical thickness correction for rapidly thinning convective clouds (Sect. 4.2.4) is applied. Due to the finer cloud structures and additional small-scale clouds, which cannot be observed in low resolution, the HRES and LRES cloud motion vector fields and thus the forecasts differ. These differences as well as the overall performance of the forecasting algorithm in high resolution are examined by means of three case studies (Sect. 5.4) and a systematic validation (Sect. 5.5).

5.4 Case studies

As mentioned in Sect. 4.4 high spatial and temporal variability in cloudiness, optical thickness and thus DNI cannot be observed and predicted due to the coarse resolution of the satellite. For this, the channel with higher spatial resolution (HRV) is used. The benefits and limitations of the determination and forecast of DNI in high resolution compared to low resolution is shown with case studies for the same scenes and equal forecast starts/lead times as in Sect. 4.4.

5.4.1 24 June 2014

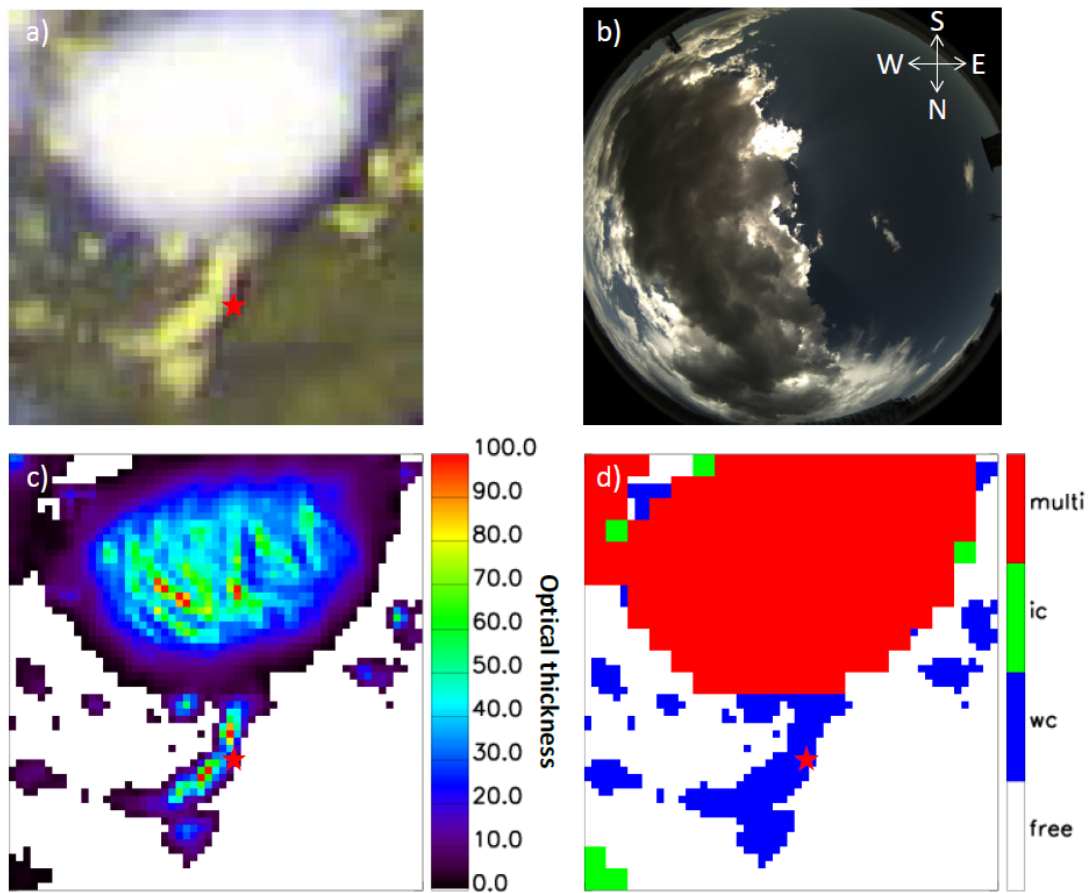


Figure 5.6: (a) False colour composite, (b) camera image, (c) total optical thickness in high resolution and (d) cloud phase mask for 24 June 2014, 13:30 UTC, in high resolution. The red star marks the position of the PSA.

As described in Sect. 4.4.2 a large cumulus cloud (cloud base height ~ 2 km) is crossing the PSA on 24 June 2014 between 13:30 UTC and 14:00 UTC reducing the incoming DNI from more than $900 W/m^2$ to $\sim 0 W/m^2$ within two minutes and vice versa half an hour later. The false colour composite in Fig. 5.6a shows

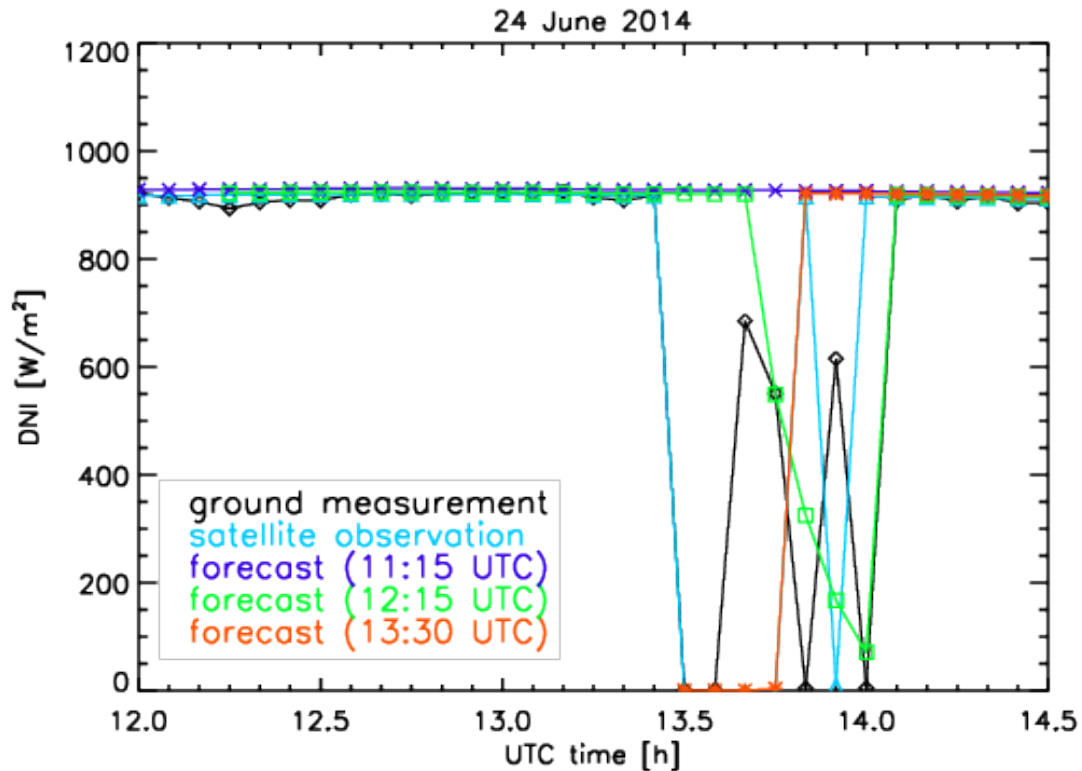


Figure 5.7: Measured (black curve) and observed (cyan curve) DNI values for 24 June 2014, 12:00-14:30 UTC. Three forecasts, started at 11:15 UTC (blue curve), 12:15 UTC (green curve) and 13:30 UTC (red curve), have been performed to show the accuracy for various forecast lead times.

the area around the PSA (red star) and the above-mentioned cloud (yellowish cloud in the center) at 13:30 UTC like in Fig. 4.17. Keep in mind the reversed north-south direction in the camera image displaying the Cb, which can be seen in the northern half of the false color composite, on the lower edge.

The derived HRES optical thickness for this scene, which is used to calculate the DNI according to Sect. 4.2.5, is depicted in Fig. 5.6c together with the HRES cloud phase mask (Fig. 5.6d). The measured DNI (Fig. 5.7, black curve) for this time period (12:00 - 14:30 UTC) illustrates the sharp gradient caused by the cloud at 13:30 and 14:05 UTC, which is also apparent in the observations (cyan curve). In contrast to the observation in low resolution (see Fig. 4.18) there is no temporal shift in the gradient at 13:30 UTC and a shift of 5 min at 14:05 UTC. Thus, the higher spatial resolution enables a more accurate determination of the time when the cloud reaches the PSA, but is also not able to resolve the DNI variability during this time except for a cloud gap at 13:55 UTC.

The forecast which starts at 13:30 UTC (Fig. 5.7, red curve) predicts the same DNI values as those observed and measured for the first 20 min, but forecasts the later gradient at 13:50 UTC, thus 15 min too early. So in this case the motion vectors derived in high resolution overestimate the velocity of the cloud. It is

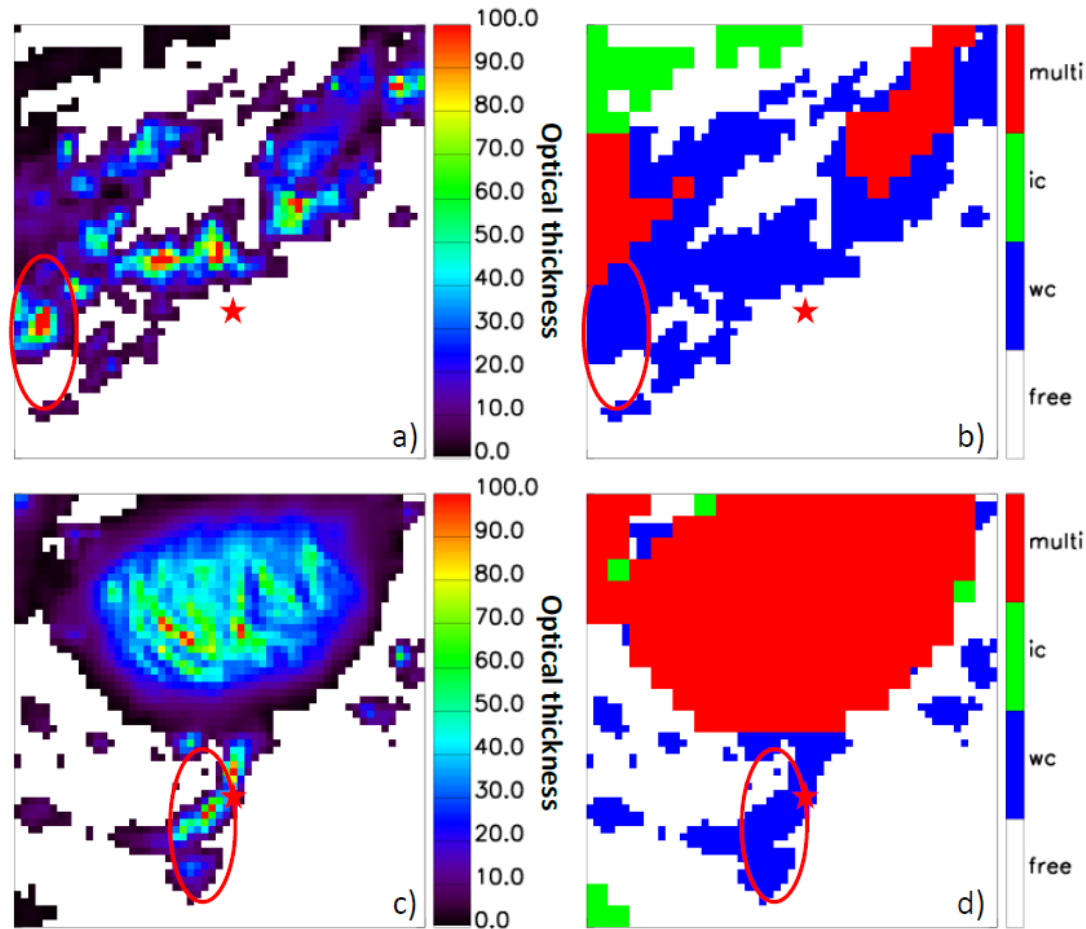


Figure 5.8: (a) Cloud optical thickness and (b) cloud phase mask for 24 June 2014, 12:15 UTC and (c)+(d) 13:30 UTC, in high resolution. The cloud crossing the PSA (red star) is circled in red.

likely, that the small-scale motion vectors show strong local displacements, which do not arise from cloud movement, but occur due to atmospheric variability. Due to their turbulence character a forecast with these motion vectors for longer lead times would result in an inaccurate prediction of cloud position. Therefore, for lead times of more than ~ 15 min the forecast should be performed with LRES cloud motion vectors. Regarding the forecast which starts at 12:15 UTC (Fig. 5.7, green curve), the cloud reaches the PSA later than in reality and the length of the time interval when the DNI is reduced by the cloud, is underestimated, possibly because the cloud was smaller at 12:15 UTC (Fig. 5.8 a,b). Also, the DNI is higher than for the observation, which are similar findings as for the forecast in low resolution. The forecast with longest lead time (start at 11:15 UTC, Fig. 5.7 (blue curve)) is not able to predict the crossing of the cloud over the PSA at all as its formation takes place to a later time.

5.4.2 8 September 2014

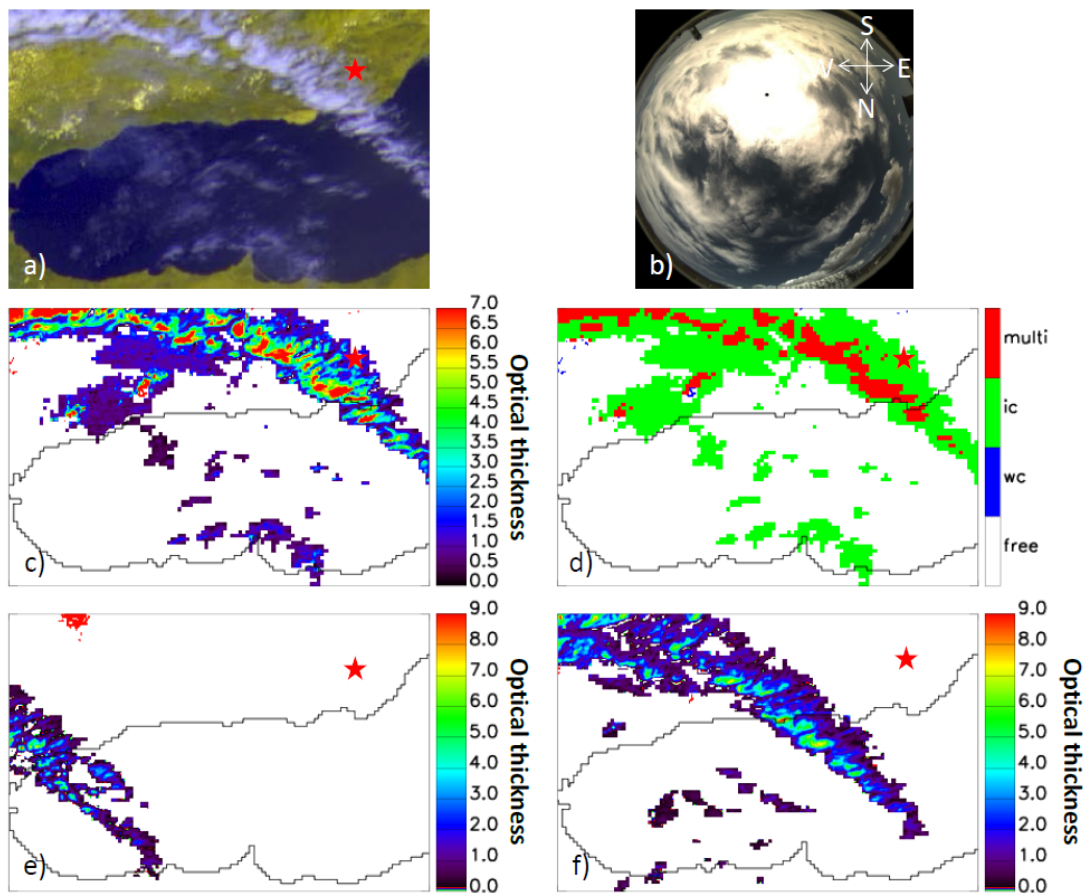


Figure 5.9: (a) False colour composite, (b) camera image, (c) total optical thickness derived by APICS and COCS and (d) cloud phase mask for 8 September 2014, 12:15 UTC, as well as total optical thickness derived by APICS and COCS for (e) 09:15 UTC and (f) 11:15 UTC in high resolution. The red star marks the position of the PSA.

The false colour composite and the camera image in Fig. 5.9 a,b show a cirrus cloud crossing the PSA (red star) on 8 September 2014, 12:05 UTC, with a HRES optical thickness up to 7 in high resolution (Fig. 4.20 c) and a cloud base height of ~ 8 km. The corresponding DNI (Fig. 4.21, black curve) is reduced to values between $\sim 50 W/m^2$ and $\sim 700 W/m^2$ from 12:05 UTC to 12:25 UTC and close to zero afterwards. The observations in high resolution (cyan curve) correctly determine the period with reduced DNI (12:05-12:25 UTC) - DNI values in good agreement with ground measurements except for 12:10 and 12:20 UTC - and subsequently the period with DNI close to zero.

The forecast which starts at 12:00 UTC predicts a stronger reduction of DNI than it is in reality (12:05-12:15 UTC) and overestimates the DNI afterwards ($> 200 W/m^2$). Thus, this forecast in high resolution is less accurate than the one produced with LRES data (Sect. 4.4). The forecasts which start at 09:15 and 11:15 UTC predict a ramp with DNI less than $200 W/m^2$, which could not

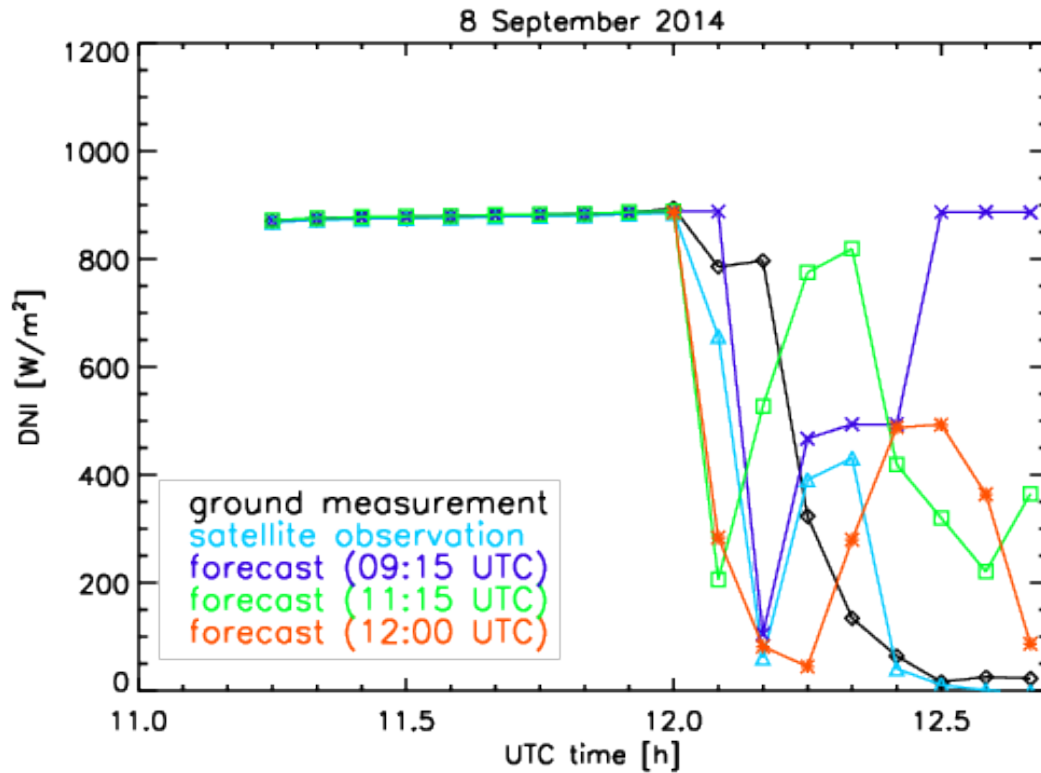


Figure 5.10: Measured (black curve) and observed (cyan curve) DNI values for 8 September 2014, 11:15-12:40 UTC. Three Forecasts, started at 09:15 UTC (blue curve), 11:15 UTC (green curve) and 12:00 UTC (red curve), have been performed to show the accuracy for various forecast lead times.

be predicted by the forecasts in low resolution. As of 12:20 UTC the DNI is overestimated due to an increase in optical thickness during the last hours, which can be seen in the increasing optical thickness and spatial growth of the cirrus (Fig. 5.9) for 09:15 UTC (e) and 11:15 UTC (f). The time when the cirrus reaches the PSA is predicted correctly (forecast at 11:15 UTC) and with a time shift of 5 min (forecast at 09:15 UTC). These are similar findings as for the forecasts in low resolution (Sect. 4.4).

5.4.3 25 June 2014

On 25 June 2014 small cumulus clouds with a cloud base height around 2.1 km develop during the day (see false colour composite in Fig. 5.11 a), which can be observed in high (Fig. 5.11 b), but not in low resolution (Fig. 5.11 c). These small-scale clouds cause a high variability in DNI between 10:00 and 11:30 UTC - see ground measurements of DNI in Fig. 5.12 (black curve). This high variability can only be partially resolved by the HRES observations (cyan curve), but an

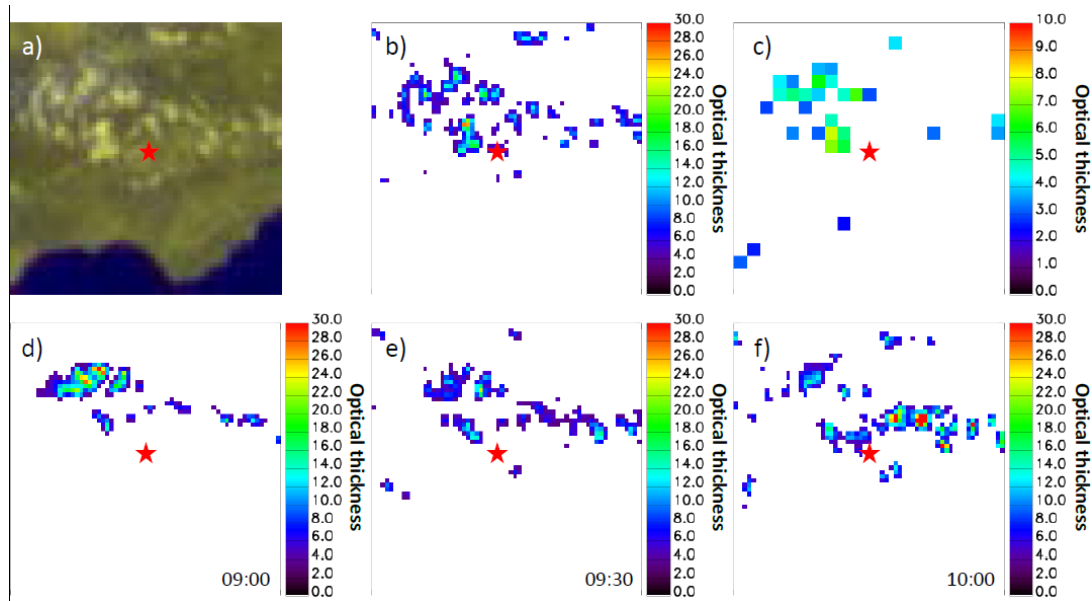


Figure 5.11: (a) False colour composite and (b) camera image and total optical thickness derived by APICS and COCS for 25 June 2014, (c) 10:25 UTC, (d) 09:00 UTC, (e) 09:30 UTC and (f) 10:00 UTC. The red star marks the position of the PSA.

improvement compared to the LRES observations is apparent (Fig. 4.23).

The forecasts, which start at 09:00 and 09:30 UTC, are not able to predict the DNI variability between 10:00 and 10:30 UTC as these clouds, which cause the variability, have not developed yet (Fig. 5.11 d,e). Regarding the forecast which starts at 10:00 UTC (Fig. 5.11 f), clouds between 10:05 and 10:30 UTC and around 11:30 UTC have been predicted. So, this forecast partially captures the reduction of DNI due to clouds but not the high variability. Having in mind that the forecast in low resolution doesn't predict a cloud at all during this time, the benefit of the HRV for situations with high atmospheric variability is obvious.

5.5 Statistical evaluation

To provide an overview of the general performance of the forecasts in high and low resolution the results for all forecasts have been compared against ground measurements. For this the same error metrics (Mean Bias Error (MBE), Mean Absolute Error (MAE) and Root Mean Squared Error (RMSE)) as well as time period (March-May 2013), forecast lead times and horizons (6h) as for the statistical evaluation in low resolution in Sect. 4.5.2 are used. The forecast are performed with the method described in Sect 5.3 using a time interval $\Delta t = 15$ min. First the results for all cases are examined before they are split into clear-sky cases and cases with thin or thick clouds to get a deeper insight.

Fig. 5.13 shows the error metrics for all cases for the forecasts in high (red) and

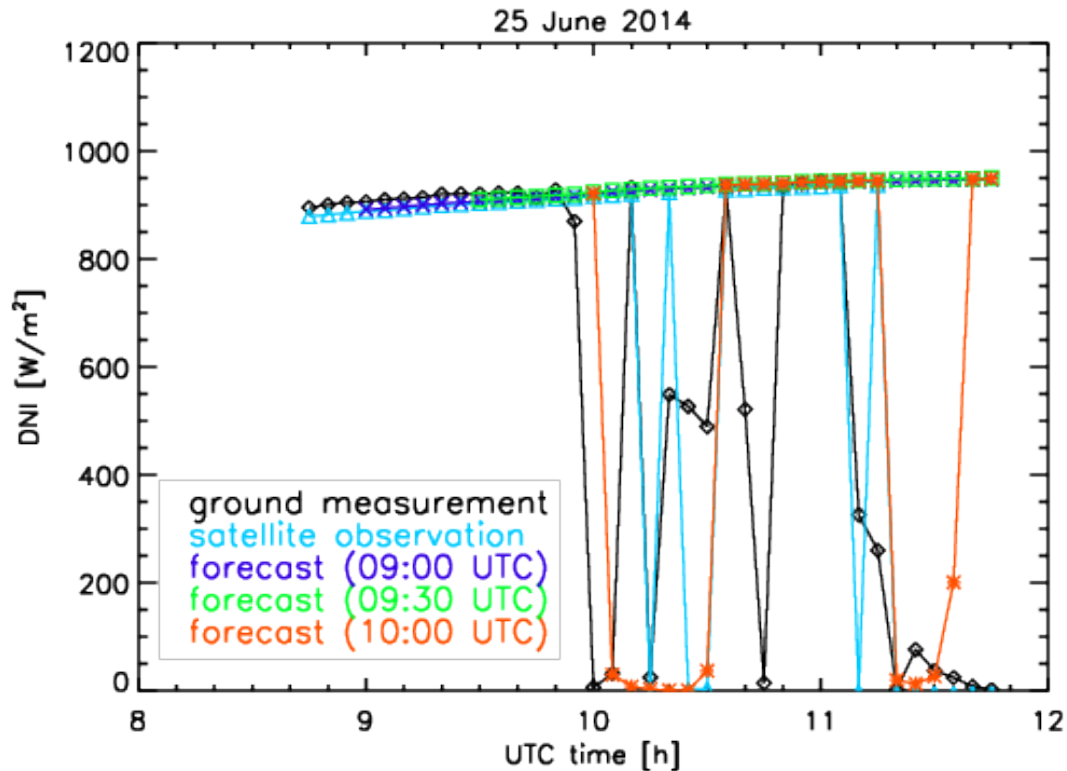


Figure 5.12: DNI cycle of measured (black curve) and observed (cyan curve) DNI values for 25 June 2014, 08:45-11:45 UTC. Three Forecasts, started at 09:00 UTC (blue curve), 09:30 UTC (green curve) and 10:00 UTC (red curve), have been performed to show the accuracy for various forecast lead times.

low (blue) resolution. In general, the behaviour is similar for both forecasts, but the absolute values can differ. Both forecasts have a low MBE around zero for all forecast lead times, thus, showing no tendency to over- or underestimate the DNI. For the first timesteps up to 15 min MAE and RMSE are similar for both forecasts with differences less than $10 W/m^2$. Thus, no improvement of the HRES forecasts due to the higher resolution can be observed as might have been expected. The reason for this is the inaccuracy in the retrieval of HRES optical thickness (missing infrared/thermal information and input parameters in high resolution) which outweighs the gain in accuracy due to the higher resolution. Afterwards the values are $10 - 50 W/m^2$ higher for the forecasts in high resolution for forecast lead times up to 3-4 hours. These results confirm the finding that for longer lead times small-scale motion vectors are not appropriate and the LRES disparity vector field should be used for the forecasts. Similar and nearly constant error metrics for forecast lead times of more than 3-4 hours indicate the approximation to a statistical value.

In order to show the influence of the accuracy in optical thickness and of the different motion vectors in high and low resolution on the error metrics for the various forecast lead times all forecasts are split into three categories: 1) clear sky,

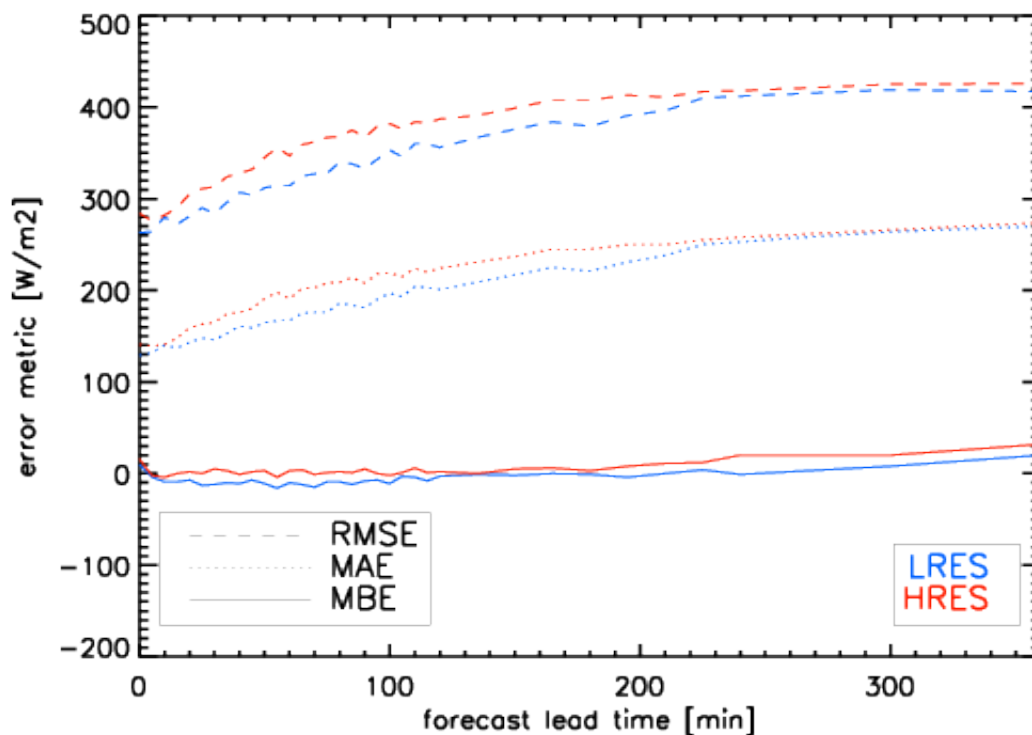


Figure 5.13: Error metrics for all cases for the forecasts in high (red) and low (blue) resolution.

2) thin clouds and 3) thick clouds. In clear-sky cases the forecasts in high and low resolution show a similar behaviour for all error metrics with approximately the same errors for the first time steps up to 15 min. Afterwards MAE and RMSE for the HRES forecasts are slightly higher ($10 - 30 W/m^2$) for forecast lead times up to 3-4 hours, whereas no difference in the MBE can be found. As no cloud optical thickness is needed for the calculation of DNI and the clear-sky model is the same inappropriate small-scale HRES motion vectors, which wrongly move clouds over the PSA, cause the higher errors for the HRES forecast for lead times of more than ~ 15 min.

For optically thin clouds the errors (MAE and RMSE) for the HRES forecasts are $10 - 100 W/m^2$ higher for all forecast lead times. Due to the lack in thermal information in high resolution the inaccuracies in the retrieval of optical thickness especially for thin clouds are higher resulting in a wrong calculation of DNI. Also, as cirrus clouds are usually quite homogeneous and widely distributed the gain in accuracy due to higher resolution is considerably low. The MBE is equal or lower for the HRES forecasts indicating that there is a lower tendency to overestimate the DNI and thus underestimate the optical thickness by the retrieval.

In case of optically thick clouds the error metrics, except the MBE, show similar results for the first time steps. Here, an exact determination of optical thickness is only required for some clouds (optical thickness < 10), thus reducing the errors

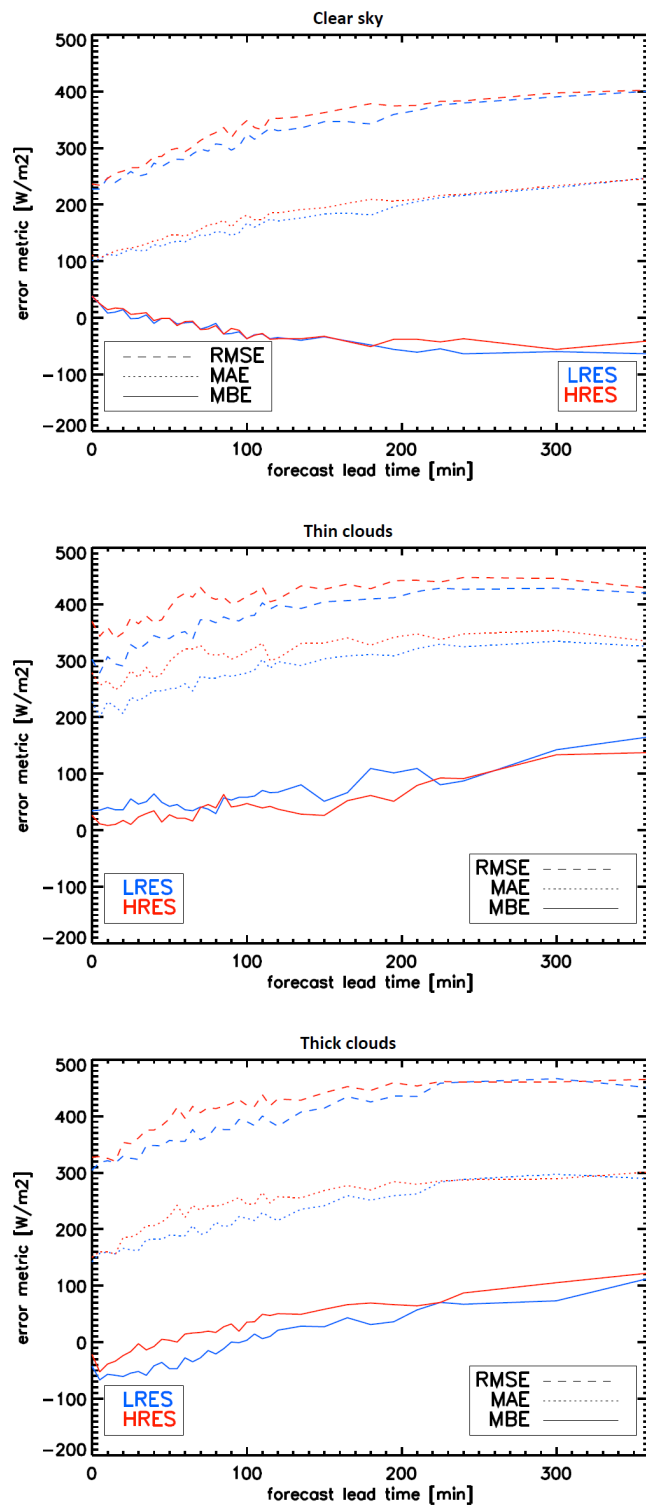


Figure 5.14: Error metrics for clear sky (top), thick clouds (middle) and thin ice clouds (bottom) for the forecasts in high (red) and low (blue) resolution.

due to the inaccurate retrieval of HRES optical thickness. These errors are outweighed by the gain in accuracy in high resolution as sharper cloud edges as well as small-scale clouds can be observed. For longer forecast lead times up to 3-4 hours all error metrics are $20 - 70 W/m^2$ higher due to inappropriate small-scale HRES motion vectors.

5.6 Conclusions

The forecasts performed with HRV data have been compared with the LRES forecasts in terms of common error statistics (cf. Sect. 4.5.2) and three case studies. For forecast lead times up to 15 min both forecasts show similar results when the inaccuracy in the retrieval of HRES optical thickness (missing infrared/thermal information and input parameters in high resolution) is compensated by the gain in detection accuracy of cloud edges, optical thickness and thus gradients in DNI due to the higher resolution (see first and third case study). Not only small-scale clouds and thus high cloud variability can be observed to a certain extent, but also the detection of these small clouds enables the short-term prediction of reduced DNI, where the LRES forecast shows no reduction (see third case study). The forecasts with lead times longer than ~ 15 min have larger errors than those in low resolution and also the case studies show similar or worse results as the small-scale motion vectors not only show the cloud movement, but also local displacements with a turbulent character. Therefore, the determination of large-scale atmospheric flow with LRES data is more appropriate to predict cloud motions for forecast lead times of more than ~ 15 min.

Chapter 6

Synergistic use of all-sky imagers and MSG/SEVIRI data for an improved cloud and DNI forecast

Due to their high spatial and temporal resolution all-sky imagers (ASI) are a valuable instrument for the detection and forecast of clouds [Cheng and Lin, 2017, Peng et al., 2016, Li et al., 2011], but an accurate determination of DNI from all-sky imagers is not feasible. Therefore, they have to be combined with ground measurements and machine learning [Marquez and Coimbra, 2013, Schmidt et al., 2015, Cazorla et al., 2015, Blanc et al., 2016] or more sophisticated devices such as a high dynamic range (HDR) camera system must be used [Urquhart et al., 2015, Kurtz and Kleissl, 2017]. In the following, an approach for the collocation of all sky and MSG/SEVIRI images is presented (Sect. 6.1) in order to predict DNI for the next minutes up to several hours. Such a continuous forecast is required or an optimized operation of solar power plants as intra-day hourly electricity production must be announced to the market operator. In Sect. 3.2 the cameras located at the PSA are described as well as the method used to derive cloud mask and cloud type. The forecast algorithm for satellite images (Sect. 4) is adjusted to enable a prediction of cloud motion (Sect. 6.2). By the description of three case studies the benefits and limitations of this approach are illustrated (Sect. 6.3). All forecasts are performed with data from the MSG satellite operating in rapid-scan-mode (located at 9.5° East) in order to use the higher repetition rate.

6.1 Collocation of ASI and MSG/SEVIRI

A pre-requisite for the collocation is an extrinsic calibration to determine the orientation of the camera in the local reference frame (see Sect. 3.2.2). Fig. 6.1

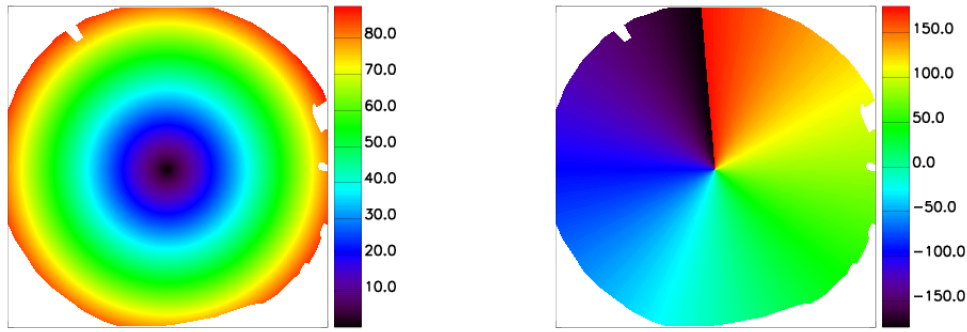


Figure 6.1: Zenith (left) and azimuth (right) angle for the all-sky imager at the KONTAS site.

shows zenith ϑ (left) and azimuth φ (right) angle for the camera at the KONTAS site. With these angles the distance d of every pixel in the image to the location of the camera can be calculated:

$$d = CBH / \tan(\vartheta), \quad (6.1)$$

where CBH is the cloud base height.

To allow a collocation with the satellite grid d must be split into the distance dy in north-south direction - positive values to the north - and the distance dx in east-west direction - positive values to the east:

$$dy = d * \cos(\varphi) \quad (6.2)$$

$$dx = d * \sin(\varphi) \quad (6.3)$$

In order to enable the calculation of the distance d the cloud base height CBH must be derived. The most accurate method is the use of ceilometer data, but as it is a point measurement, only one cloud base height for the whole camera scene can be determined. In case of varying cloud altitudes this leads to errors in the distance of the clouds from the camera location. Also in cases when the clouds do not move across the location of the ceilometer no data are available.

In order to enable a collocation of all sky and satellite data the camera images are brought to the MSG/SEVIRI grid. For this the distances dy and dx from the location of the camera are calculated via Eq. 6.2 and 6.3 with a CBH of 2km in this case, which has been derived from ceilometer data. Fig. 6.2 shows the (a) MSG/SEVIRI false colour composite and (b) the camera image for 24 June 2014, 13:25 UTC, which is one of the case studies shown in Sect. 4.4 and 5.4. Keep in mind the reversed north-south direction in the camera image. With the method described in Sect. 5.1.2 a HRES cloud mask has been made for this scene (Fig. 6.2c). Fig. 6.2d shows the cloud mask of the camera image after transformation to the satellite grid. North is now pointing upwards as it is in satellite projection and the pixel size is 50 m - a much higher resolution than

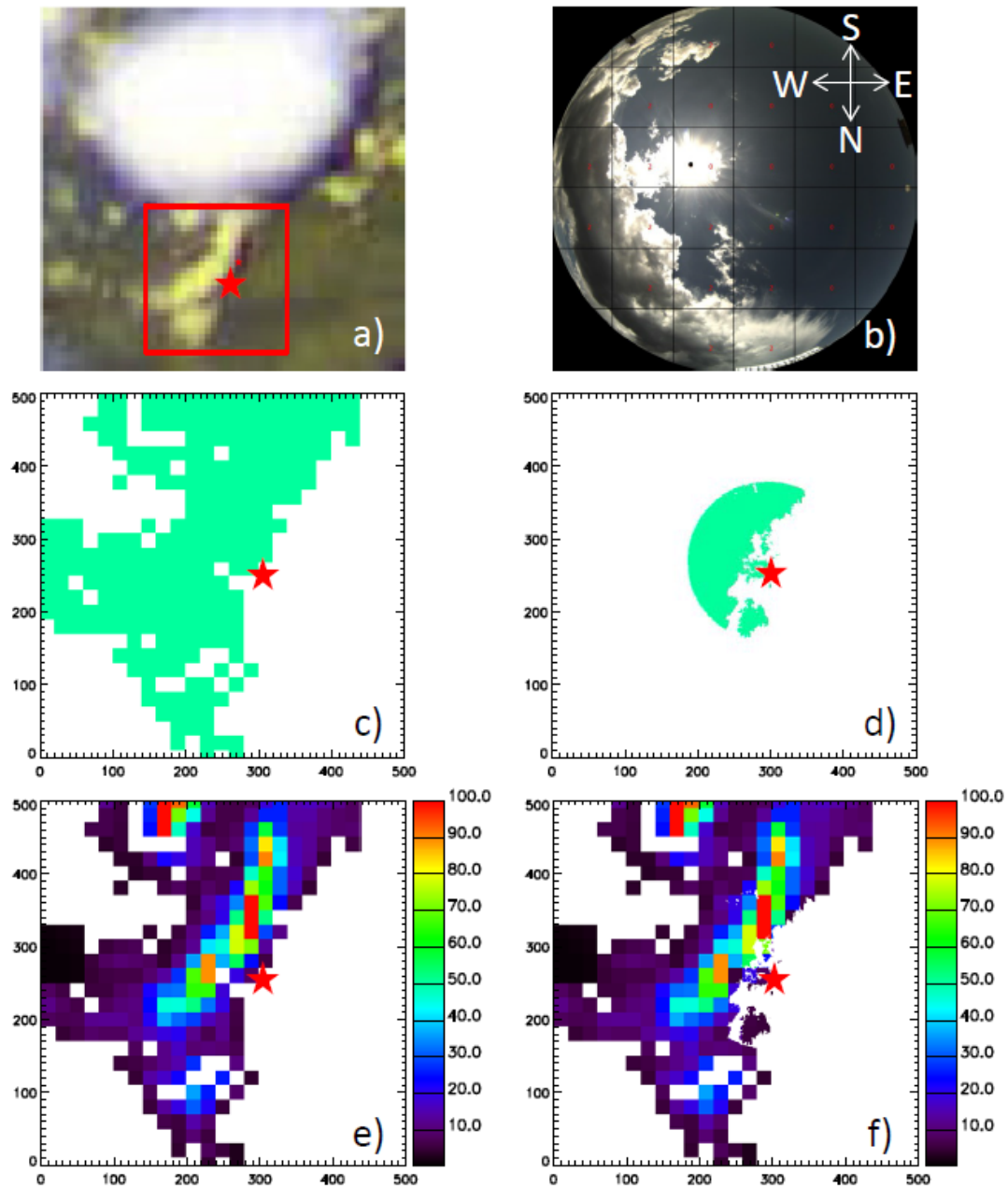


Figure 6.2: (a) False colour composite, (b) camera image, (c) HRES cloud mask, (d) cloud mask of the camera image after transformation to satellite perspective, (e) HRES total optical thickness derived with LUTs and (f) total optical thickness for combined satellite and camera data for 24 June 2014 with the location of the camera in the center. Area size in (a)-(e) is 500×500 pixels with a pixel size of 50 m.

for the satellite. Both cloud masks show the same area with the location of the camera in the center (red star). Note the smaller field of view of the camera and the much finer cloud structures.

The forecast is performed according to Sect. 4. Therefore, the cloud optical

thickness is required, which cannot be derived by camera images and hence the HRES optical thickness is used (Sect. 5.2). For pixels, that have been identified as cloudy by MSG/SEVIRI and the camera, the HRES optical thickness is applied, whereas for those cloudy pixels, that have only been detected by the camera, the mean HRES optical thickness of the neighbouring pixels is used. Pixels, which have been determined as cloudy by MSG/SEVIRI but not the camera, are set to zero optical thickness as the camera is expected to detect cloudy pixels more efficient. Fig. 6.2 e,f shows the HRES cloud optical thickness for this scene and the optical thickness for the camera derived with the method described above.

6.2 Forecast

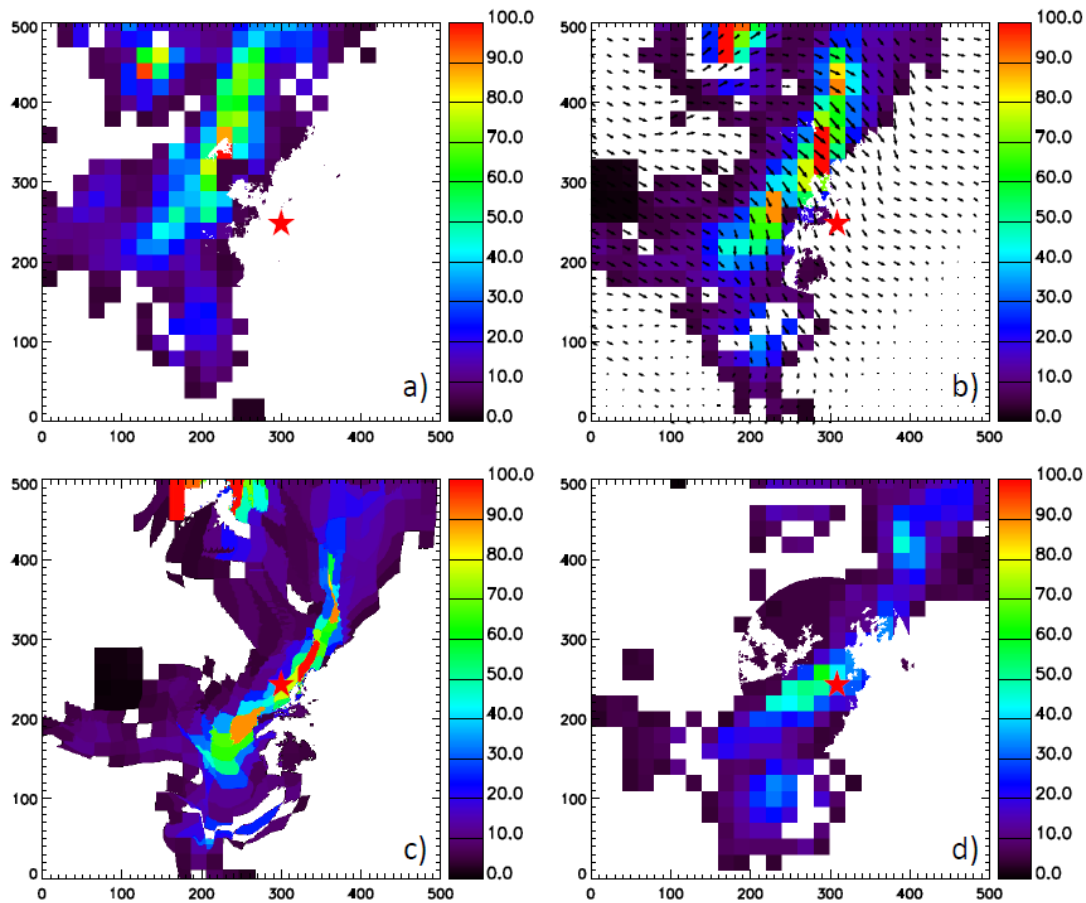


Figure 6.3: Illustration of the forecast of optical thickness for 24 June 2014. (a)+(b) Initial images A (13:20 UTC) and B (13:25 UTC) with the calculated disparity vector field on top. (c) 10 min-forecast (i.e. for 13:35 UTC) of cloud optical thickness. (d) Cloud optical thickness at 13:35 UTC.

The forecast is based on the method described in Sect. 4. In order to take into account the higher spatial resolution the time interval Δt between the initial images

A and B is 5 min (rapid scan mode of MSG/SEVIRI) instead of 15 min. With the pyramidal matcher (Sect. 3.4) the disparity vector field $\vec{V}_{A \rightarrow B}$ is determined. Due to the high spatial resolution the number of sub-sampling levels is set to $N = 3$ and the smoothing is enhanced by an increase of the size of the Gaussian Kernel KE (Sect. 3.4). An object classification (Sect. 4.2.2), the interpolation of cloud-free background motion (Sect. 4.2.3) and the optical thickness correction for rapidly thinning convective clouds (Sect. 4.2.4) are performed. The forecasts are produced with a temporal resolution of $\Delta t_f = 1$ min.

Fig. 6.3 shows an example for a forecast for the same scene as in Fig. 6.2. The optical thickness of the initial images A and B is depicted for 13:20 UTC (a) and 13:25 UTC (b). The disparity vector field $\vec{V} = \vec{V}_{A \rightarrow B}$ obtained from these two images is displayed in Fig. 6.3 b using small arrows. For clarity only one out of ten vectors is shown. The full motion vector field is applied to the 13:25 UTC image to produce a 10 min-forecast (Fig. 6.3 c), which can be compared to the cloud optical thickness observed at this time (Fig. 6.3 d). The movement of the cloud above the PSA is predicted correctly, but the forecast of the small-scale structure is not exact due to the small-scale atmospheric variability causing continuous changes in cloud form and optical thickness.

6.3 Case studies

The three case studies are the same as in Sect. 4.4 and 5.4, but due to the limited spatial coverage of the camera only short term forecasts up to ~ 30 min are considered. Also the temporal resolution is enhanced with $\Delta t_f = 1$ min. In order to enable a comparison between satellite-based forecasts and the forecasts derived by combined satellite and camera data the temporal resolution has to be aligned. For this, forecasts of HRES optical thickness with a time interval $\Delta t = 5$ min between the initial images A and B and a temporal resolution of 1 min has been performed for the case studies. Additionally satellite-based forecasts in low and high resolution with a time interval $\Delta t = 15$ min and a temporal resolution of 1 min are produced to enable a comparison to the forecasts in Sect. 4 and 5, respectively.

6.3.1 24 June 2014

This case study has been introduced in Sect. 6.1 and 6.2 to illustrate the forecast with combined satellite and camera data. Fig. 6.2 shows (a) the false colour composite, (b) the camera image and (f) the total optical thickness for combined satellite and camera data for 24 June 2014, 13:25 UTC. The measured DNI (Fig. 6.4, black curve) for this time period (13:25 - 14:10 UTC) illustrates the sharp gradients caused by the cloud at 13:29 and 14:01 UTC, but also periods

of variable DNI in between due to variability in cloud optical thickness. The satellite-based forecast in low resolution, which starts at 13:25 UTC, predicts the gradients at 13:31 and 14:05 UTC and the forecasts performed with the HRV predict the gradients at 13:26 and 13:55 UTC ($\Delta t = 15$ min) as well as 14:04 UTC ($\Delta t = 5$ min). These shifts are caused by the coarse spatial resolution of the satellite and the inaccuracy of the motion vectors for a high temporal resolution of 1 min. The forecast derived by combined satellite and camera data predicts the gradients with a shift of 1 min (13:30 and 13:59 UTC) using the benefit of the higher spatial resolution of the camera. Note that all forecasts are not able to predict the DNI variability between the gradients as no information about cloud optical thickness from the camera is available and the coarse satellite derived cloud optical thickness is used for the calculation of DNI.

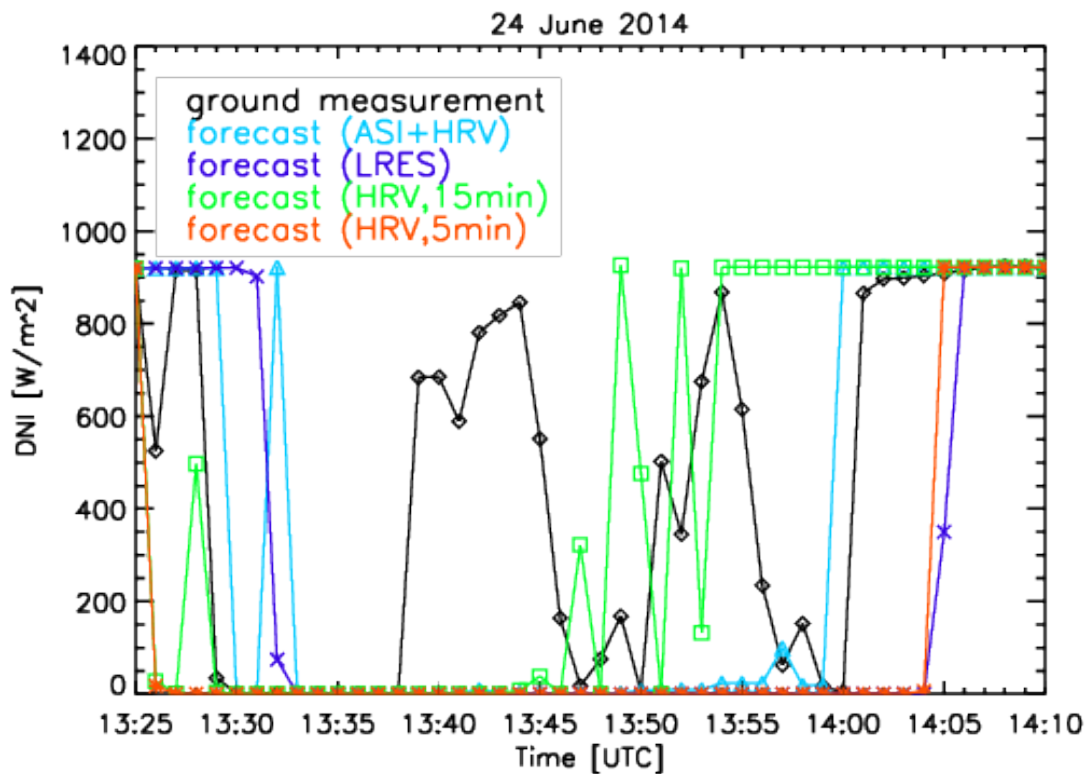


Figure 6.4: Measured (black curve) DNI values for 24 June 2014, 13:25-14:10 UTC, satellite-based forecasts in low resolution (blue curve), in high resolution with a time interval $\Delta t = 15$ min (green curve) and $\Delta t = 5$ min (red curve) as well as a forecast derived with combined satellite and camera data (cyan curve). All forecasts start at 13:25 UTC.

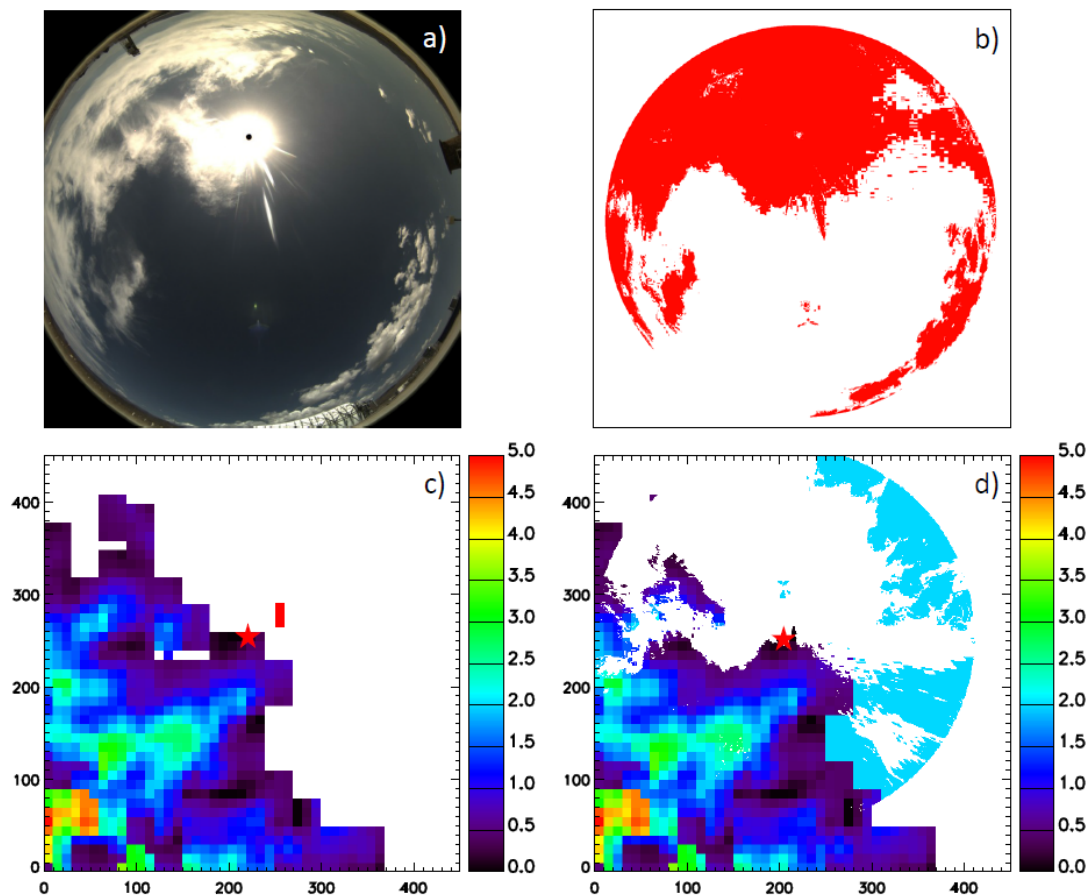


Figure 6.5: (a) Camera image, (b) camera cloud mask (c) HRES total optical thickness and (d) total optical thickness for combined satellite and camera data for 8 September 2014, 12:00 UTC. The red star marks the position of the PSA.

6.3.2 8 September 2014

On 8 September 2014 a cirrus cloud is crossing the PSA (red star) from southwest to northeast (Fig. 6.5). Keep in mind the reversed north-south direction in the camera image. The observed HRES optical thickness is shown in Fig. 6.5 c together with the optical thickness derived with combined satellite and camera data (Fig. 6.5 d). In the right part of Fig. 6.5 d clouds are detected, which have not been observed by MSG/SEVIRI although they should be big enough according to the image. In case of the cloud in the upper right corner (Fig. 6.5 d) the location of the cloud has been incorrectly calculated due to a wrong CBH. This cloud corresponds to the small cloud with high optical thickness north-eastern of the PSA detected by MSG/SEVIRI (Fig. 6.5 c) and the cumulus clouds in the lower right corner of the camera image (Fig. 6.5 a). As only one cloud base height can be determined with the ceilometer this value is applied to all cloudy pixels in the camera scene. In case of varying cloud types this leads to errors in the calculation of the cloud distance to the camera. A CBH of 8 km, which has been

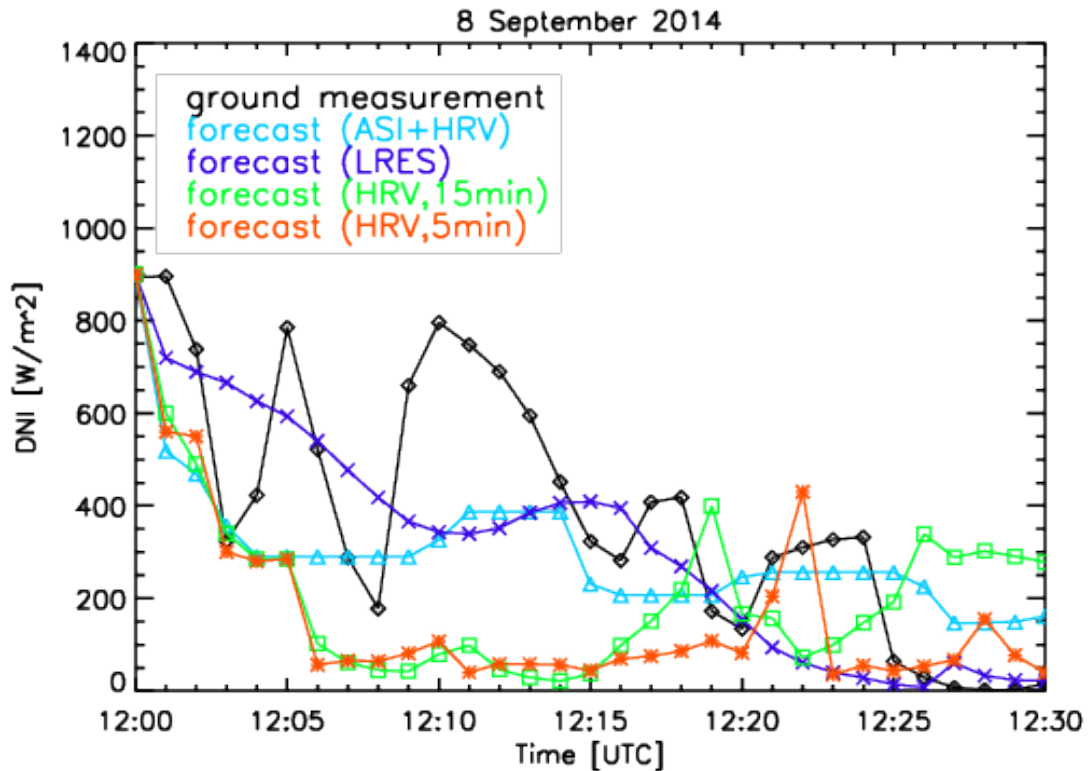


Figure 6.6: Measured (black curve) DNI values for 8 September 2014, 12:00-12:30 UTC, satellite-based forecasts in low resolution (blue curve), in high resolution with a time interval $\Delta t = 15$ min (green curve) and $\Delta t = 5$ min (red curve) as well as a forecast derived with combined satellite and camera data (cyan curve). All forecasts start at 12:00 UTC.

determined for the cirrus clouds by the ceilometer, results in a higher distance of the cumulus clouds (CBH of typically a few kilometers) to the camera than in reality. Therefore, an exact knowledge of the CBH for every cloudy pixel is essential for an accurate collocation of all-sky and MSG/SEVIRI images.

The wrong detection of the cloud in the south-east of the PSA (Fig. 6.5 d) is caused by errors in the camera cloud mask (Fig. 6.5 b). Cloud free pixels in the upper right corner and around the sun (Fig. 6.5 a) has been falsely classified as cloudy.

As these wrongly detected clouds do not cross the PSA an accurate determination and forecast of DNI can be performed though. According to the measured DNI (Fig. 6.6, black curve) for this time period (12:00 - 12:30 UTC) the cirrus reaches the PSA at 12:02 UTC and is increasing in optical thickness, thus reducing the DNI to zero within 25 min. The forecast derived by combined satellite and camera data (cyan curve), which starts at 12:00 UTC, predicts the cloud for 12:01 UTC and is able to forecast the reduction of DNI. This forecast also mostly captures the period with DNI larger than 200 W/m^2 until 12:25 UTC and with DNI less than 200 W/m^2 afterwards. This is also valid for the LRES forecast,

which predicts the decrease in DNI quite well, but not the variability due to the low spatial resolution. By contrast, the forecasts performed with the HRV (green and red curve, start at 12:00 UTC) predict DNI less than $200 W/m^2$ for most of the time except the first six minutes, when the decrease in DNI is forecasted correctly. The low DNI close to zero as of 12:25 UTC is captured by the forecast performed with a time interval $\Delta t = 5$ min, whereas the forecast performed with a time interval $\Delta t = 15$ min predicts DNI larger than $200 W/m^2$. These results confirm the stated inaccuracy in the retrieval of HRES optical thickness due to missing infrared/thermal information and input parameters in high resolution.

6.3.3 25 June 2014

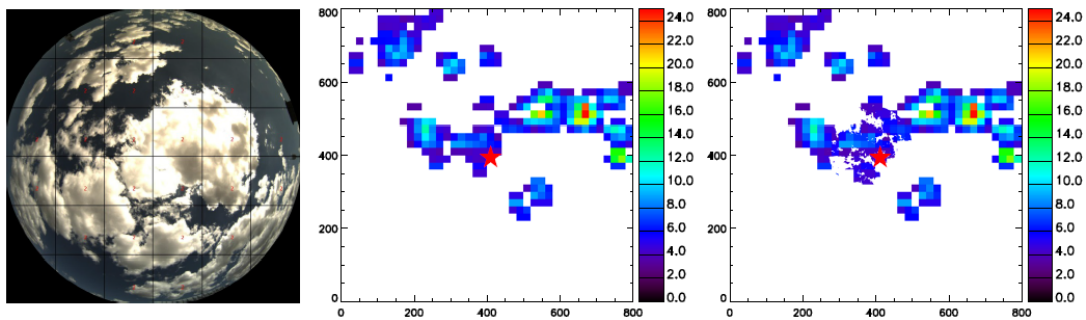


Figure 6.7: (left) Camera image, (middle) HRES total optical thickness and (right) total optical thickness for combined satellite and camera data for 25 June 2014, 10:00 UTC. The red star marks the position of the PSA.

Because of the development of small cumulus clouds on 25 June 2014 (Fig. 6.7) the DNI is highly variable (Fig. 6.8, black curve) during the examined period (10:00 - 10:35 UTC). The forecast derived by combined satellite and camera data (cyan curve), which starts at 10:00 UTC, is able to predict the low DNI for the first minutes, but not the following high variability due to the coarse resolution of the satellite derived optical thickness. Also, the small cloud holes (maximum DNI) can be determined but not predicted as the clouds continuously change due to the high atmospheric variability and as the uncertainties in the forecast algorithm are too large to correctly predict such fine structures. The satellite-based forecasts in high resolution (Fig. 6.8, red curve and green curve) start with maximum DNI values and are thus not able to determine the exact position of the cloud edge due to its coarse resolution. For the same reason the high variability in DNI is not predicted. The LRES forecast (Fig. 6.8, blue curve) is not able to detect and predict the clouds at all and produces clear-sky DNI values for the whole period.

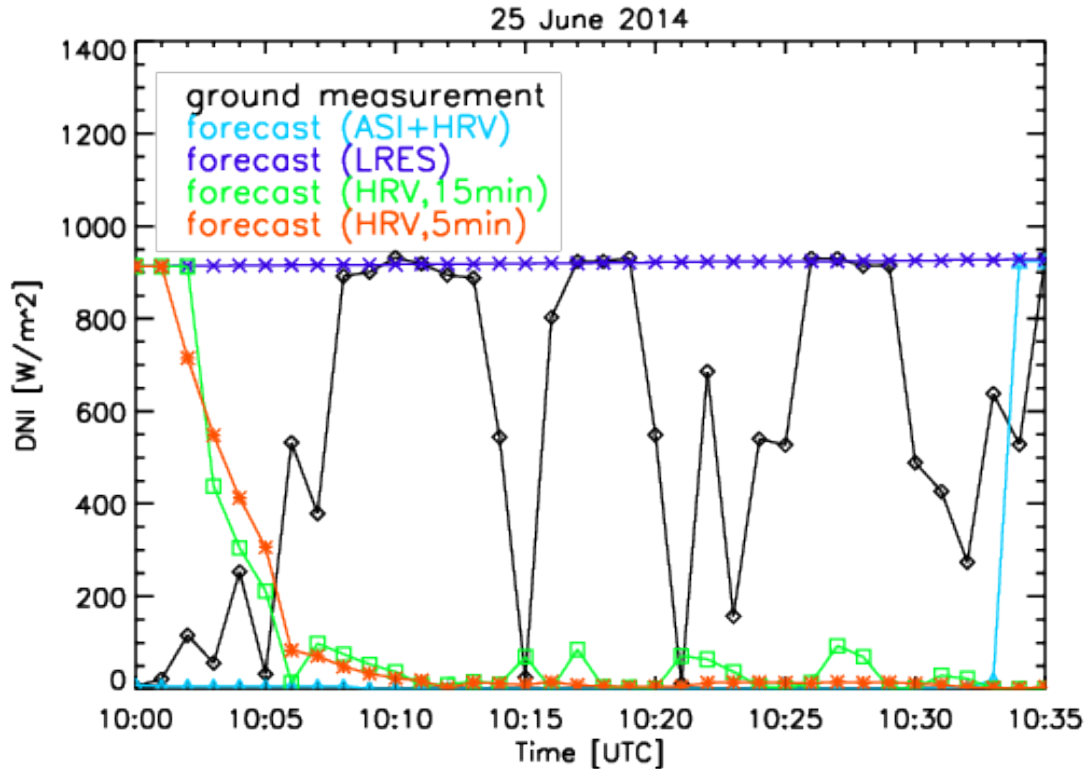


Figure 6.8: DNI cycle of measured (black curve) DNI values for 25 June 2014, 10:00-10:35 UTC, satellite based forecasts in low resolution (blue curve), in high resolution with a time interval $\Delta t = 15$ min (green curve) and $\Delta t = 5$ min (red curve) as well as a forecast derived with combined satellite and camera data (cyan curve). All forecasts start at 10:00 UTC.

6.4 Conclusions

The aim of this approach was to combine the advantages of all-sky imagers (high spatial resolution) and satellite data (large spatial coverage) to overcome their limitations - the coarse spatial and resolution of the satellites as well as the small spatial coverage of the cameras and the lack of cloud optical properties. With this method cloud edges can be determined more accurately than with satellite data alone as can be observed in all case studies. Also, changes in DNI for forecast lead times of 30 min or more can be predicted (see first case study), which is not possible for camera-based forecast methods as these cloud structures don't lie within the field of view of the camera. High variability in DNI cannot be determined and predicted as the cloud optical thickness is derived with satellite data. Also, the forecast of fine cloud structures can become inaccurate within a forecast lead time of a few minutes (see third case study) due to the high atmospheric variability and rising uncertainties in the forecast algorithm and the parallax correction.

Chapter 7

Summary, Conclusions and Outlook

7.1 Summary and Conclusions

For an optimum use of solar energy operators of CSP plants are reliant on the prediction of DNI. Since forecasts of clouds and surface DNI by NWP models are not accurate on the minute to several hour scale, satellite and camera data are used in this work in order to investigate the following hypothesis: "It is possible to provide seamless and accurate forecasts of clouds and surface DNI for the next minutes up to several hours with high spatial resolution for the improved operation of CSP plants."

In order to assess the hypothesis, several questions have to be answered. The first question investigated in this thesis was:

- 1) Can low resolution MSG/SEVIRI data be used for the accurate nowcasting of warm and cold cloud properties and surface DNI at the 3-5 km scale?

For this, a forecast algorithm for input data from the imager SEVIRI aboard the geostationary MSG satellite has been developed, which is based on an optical flow method deriving cloud motion between two consecutive images. The algorithms COCS and APICS provide cloud detection and cloud optical thickness for two vertically separated layers. Because of different velocities and motion directions these low and high level clouds are forecasted separately. Using the derived and forecasted cloud optical thickness the DNI is calculated via a parameterisation. The performance of the forecast algorithm has been qualitatively validated using satellite observations for March and July 2013, case studies for different meteorological situations, ground-based irradiance measurements and two satellite-based nowcasting methods. For cases under clear-sky conditions our method performs

best for most forecast lead times confirming the good performance of the DNI parameterisation and the forecast algorithm as well as the quality of the input data, i.e. aerosol load and water vapour. When thin clouds occur, our algorithm shows equal or worse results compared to the other methods, thus pointing out deficiencies in the retrieval of optical thickness of thin clouds. In case of thick clouds the methods show similar results indicating a comparable performance of the forecast algorithms as there is almost no influence of the accuracy of the clear-sky models and the determination of optical thickness on the results due to the high optical thickness of the clouds (no DNI at the ground). As far as cloud detection is concerned, the largest inaccuracy consists in the difficulty to retrieve clouds below optically thick ice clouds. Consequently, forecast errors for the lower cloud layer are considerably higher than for high clouds. For any given forecast quality requirement, over all cloud (or weather) types and for both cloud layers, a doubling of lead time is found comparing the forecast to the assumption of persistence. For advective clouds with low variability and approximately constant velocity the prediction of DNI gradients is accurate even for forecast lead times of several hours. In case of broken cumulus cloud fields and rapidly changing small-scale convective cloud fields, a correct determination and forecast of DNI is difficult due to the coarse resolution of the satellite and the high variability in the atmosphere.

In order to examine the gain in forecast accuracy of clouds and DNI by enhancing the spatial resolution a synergistic exploitation of high and low resolution together with radiative transfer calculations has been applied. With a threshold technique for LRES and HRES reflectivities cloud masks as well as cloud phase masks are determined and cloud optical thickness is derived from LUTs. In this context the following question has been examined:

- 2) To what extent does the high resolution visible channel of MSG/SEVIRI help enhancing the spatial resolution of the nowcasting of warm and cold cloud properties and surface DNI to the 1-2 km scale?

Due to a statistical evaluation the forecasts performed with LRES and HRES data show similar results for lead times up to 15 min, when the inaccuracy in the retrieval of HRES optical thickness (missing infrared/thermal information and input parameters in high resolution) is compensated by the gain in detection accuracy of cloud position due to the higher resolution. For longer lead times LRES forecasts perform better as motion vectors determined in low resolution are more appropriate to represent the large-scale atmospheric flow. The case studies show that cloud edges and small clouds can be detected more accurate with the HRV, which enables a more exact determination and short-term forecast of DNI. In case of widely distributed and relatively homogeneous clouds no benefit in the usage of the HRV can be seen. Therefore, the HRV can improve short-term forecasts up to 15 min in certain situations (high small-scale variability in the atmosphere) due to its higher spatial resolution, but for most cases and longer

lead times the forecasts should be performed with motion vectors derived in low resolution.

In order to better characterise the local cloud situation at a specific site, e.g. the PSA, which is required for an optimized operation of solar power plants, all-sky imagers have been used to identify clouds in higher resolution. A special focus has been laid on the question:

- 3) Is there a promising approach to get a reasonable forecast of surface DNI by combining satellite and camera data?

For this, a novel approach for the collocation of camera and satellite images has been performed. By bringing the camera images to the satellite grid a synergistic use of camera and satellite data enables a forecast of optical thickness and thus DNI in high accuracy for forecast lead times of 30 min or more for certain situations, i.e. at cloud edges and in case of small-scale clouds. The case studies show the advantages and limitations of the combination of these methods compared to the single methods. Forecasts with longer lead times than with all-sky imagers alone can be performed because of the larger spatial coverage of the satellite. Also, satellite data are required for the determination of cloud optical properties and DNI as those cannot be derived by the all-sky imagers. In case of very high atmospheric variability the forecast of fine cloud structures can become inaccurate within a forecast lead time of a few minutes and high variability in DNI cannot be determined and predicted as the cloud optical thickness is derived with satellite data. Nonetheless, this approach of combining all-sky imager and satellite data is able to provide a more accurate forecast of DNI for lead times up to 30 min or more. For forecasts with longer lead times low resolution data from MSG/SEVIRI should be used as these are more appropriate to represent the large-scale atmospheric flow. But as the results of this method are examined with only three case studies and no statistical evaluation is done the findings should not be generalized.

Thus, the hypothesis of the thesis "It is possible to provide seamless and accurate forecasts of clouds and surface DNI for the next minutes up to several hours with high spatial resolution for the improved operation of CSP plants" could be verified. With the high spatial and temporal resolution of MSG/SEVIRI forecasts every 5 min can be created with a spatial resolution of 1 km. This resolution can also be further enhanced by means of all-sky imagers. The results show good agreement between forecast and measurements/observations.

The presented nowcasting algorithm differs from other forecast methods in some aspects. Unlike feature based approaches, often used for the determination of atmospheric motion vectors [e.g. Bolliger et al., 2003, Schmetz et al., 1993], the optical flow method applied in this work is pixel-based: instead of vectors only for interesting cloud patterns a disparity vector field defined at each pixel position is derived. By exploiting several channels of MSG/SEVIRI cloud optical properties are derived with a focus on thin cirrus clouds as those clouds can reduce DNI to a

still usable level, thus playing an important role in the forecast of DNI. With the derived optical thickness the DNI is calculated via a parameterisation, whereas other methods use e.g. clearness index [Qu et al., 2016, Müller and Remund, 2016] or ANNs trained with ground measurements [Eissa et al., 2013]. So far, the HRV has been used for the improvements of cloud masks for small-scale convective clouds [Bley and Deneke, 2013, Klüser et al., 2008, Derrien et al., 2010] and for the derivation of optical thickness for thick clouds [Henken et al., 2011]. In this work cloud optical properties, i.e. optical thickness, in high resolution are derived by combining LRES and HRES satellite data together with radiative transfer calculations.

7.2 Outlook

One possibility to further improve forecast accuracy of DNI is the implementation of ground measurements in the algorithm. The forecasts profit from more exact initial conditions due the determination of DNI by e.g. pyrheliometers, which is especially valid for clear-sky cases. In particular, aerosols can reduce DNI significantly and their influence on the attenuation of DNI can be determined more precise with ground measurements than with satellite data.

The case studies showed that for the first time steps a disparity vector field derived by combined satellite and camera data should be used and for longer lead times the LRES disparity vector field to consider the large-scale atmospheric flow. But these findings cannot be generalized due to a missing statistical evaluation, which has to be done in the future.

Future work should also deal with the question, at which time step the motion vectors derived by combined satellite and camera data should be replaced by LRES motion vectors and how to avoid discontinuities. One important factor for the determination of this time step is the field of view of the camera as the benefit of the high resolution of the camera can only be exploited for the detection and the forecast of those clouds which are observed by the camera. Also, the velocity of the clouds and their type have to be considered in this context. In case of stationary (cumulus) clouds a later time step could be reasonable as the scene is dominated by small-scale motion and the focus should be on the high spatial resolution. In contrast, in situations with fast moving and/or widely distributed, homogeneous clouds an earlier time step should be chosen as the observed clouds leave the camera field of view after a few minutes due to their high velocity and large-scale movement is more important.

As an exact determination of cloudy pixels in the camera image is crucial for an accurate collocation of camera and satellite data future work should deal with the improvement of the camera cloud masks. If clouds are detected which do not exist and vice versa, the prediction of optical thickness and thus DNI exhibits

large errors rendering the forecast useless for power plant operators. Especially, in case of thin clouds and in the region near the sun a correct cloud detection is challenging. Another important pre-requisite for the presented method is an exact knowledge of CBH for every cloud in the scene to determine the distance of the cloud to the camera and thus its position in the satellite grid. Therefore, methods should be examined which are able to derive a two-dimensional field of CBH by means of two or more all-sky imagers. Most approaches deal with stereographic/stereoscopic methods [Nguyen and Kleissl, 2014, Peng et al., 2015, Blanc et al., 2016], but also combinations of sky imagers with other instruments, e.g. cloud speed sensors [Wang et al., 2016], are investigated. The uncertainties for CBH estimation are in a range of several hundred meters or even more for some situations. With these methods a two-dimensional field of CBH can be derived, but the uncertainties are large and have to be reduced in the future.

Bibliography

- C. Accadia, S. Mariani, M. Casaioli, A. Lavagnini, and A. Speranza. Sensitivity of Precipitation Forecast Skill Scores to Bilinear Interpolation and a Simple Nearest-Neighbor Average Method on High-Resolution Verification Grids. *Weather and Forecasting*, 18(5):918–932, 2003. doi: 10.1175/1520-0434(2003)018<0918:SOPFSS>2.0.CO;2.
- G. Anderson, S. Clough, F. Kneizys, J. Chetwynd, and E. Shettle. AFGL Atmospheric Constituent Profiles (0-120 km). Technical Report AFGL-TR-86-0110, AFGL (OPI), Hanscom AFB, MA 01736, 1986.
- A. Baran. On the scattering and absorption properties of cirrus clouds. *Journal of Quantitative Spectroscopy and Radiative Transfer*, 89:17–36, 2004. doi: 10.1016/j.jqsrt.2004.05.008.
- B. Baum, A. Heymsfield, P. Yang, and S. Bedka. Bulk scattering models for the remote sensing of ice clouds. Part 1: Microphysical data and models. *J. Appl. Meteor.*, 44:1885–1895, 2005. doi: 10.1175/JAM2308.1.
- B. A. Baum, T. Uttal, M. Poellot, T. P. Ackermann, J. M. Alvarez, J. Intrieri, D. O. C. Starr, J. Titlow, V. Tovinkere, and E. Clothiaux. Satellite remote sensing of multiple cloud layers. *J. Atmos. Sci.*, 52(23):4210–4230, 1995. doi: 10.1175/1520-0469(1995)052<4210:SRSOMC>2.0.CO;2.
- B. A. Baum, P. Yang, A. J. Heymsfield, C. G. Schmitt, Y. Xie, A. Bansemmer, Y.-X. Hu, and Z. Zhang. Improvements in Shortwave Bulk Scattering and Absorption Models for the Remote Sensing of Ice Clouds. *J. Appl. Meteor. Climatol.*, 50:1037–1056, 2011. doi: 10.1175/2010JAMC2608.1.
- D. Bernecker, C. Riess, E. Angelopoulou, and J. Hornegger. Continuous short-term irradiance forecasts using sky images. *Sol. Energy*, 110:303–315, 2014. doi: 10.1016/j.solener.2014.09.005.
- H. Beyer, C. Costanzo, and D. Heinemann. Modifications of the HELIOSAT procedure for irradiance estimates from satellite images. *Sol. Energy*, 56(3): 207–212, 1996. doi: 10.1016/0038-092X(95)00092-6.

- P. Blanc, B. Espinar, N. Geuder, C. Gueymard, R. Meyer, R. Pitz-Paal, B. Reinhardt, D. Renne, M. Sengupta, L. Wald, and S. Wilbert. Direct normal irradiance related definitions and applications: The circumsolar issue. *Sol. Energy*, 110:561–577, 2014. doi: 10.1016/j.solener.2014.10.001.
- P. Blanc, P. Massip, A. Kazantzidis, P. Tzoumanikas, P. Kuhn, S. Wilbert, D. Schüler, and C. Prah. Short-term forecasting of high resolution local DNI maps with multiple fish-eye cameras in stereoscopic mode. In *22nd SolarPACES Conference 2016, Oct 2016, Abu Dhabi, United Arab Emirates*, 2016.
- S. Bley and H. Deneke. A threshold-based cloud mask for the high-resolution visible channel of Meteosat Second Generation SEVIRI. *Atmos. Meas. Tech.*, 6:2713–2723, 2013. doi: 10.5194/amt-6-2713-2013.
- S. Bley, H. M. Deneke, and F. Senf. Meteosat-Based Characterization of the Spatio-Temporal Evolution of Warm Convective Cloud Fields over Central Europe. *J. Appl. Meteor. Climatol.*, 55(10):2181–2195, 2016. doi: 10.1175/JAMC-D-15-0335.1.
- M. Bolliger, P. Binder, and A. Rossa. Tracking cloud patterns by METEOSAT rapid scan imagery in complex terrain. *Meteorol. Z.*, 12(2):73–80, 2003. doi: 10.1127/0941-2948/2003/0012-0073.
- J. L. Bosch, Y. Zheng, and J. Kleissl. Deriving cloud velocity from an array of solar radiation measurements. *Sol. Energy*, 87:196–203, 2012. doi: 10.1016/j.solener.2012.10.020.
- L. Bugliaro, T. Zinner, C. Keil, B. Mayer, R. Hollmann, M. Reuter, and W. Thomas. Validation of cloud property retrievals with simulated satellite radiances: a case study for SEVIRI. *Atmos. Chem. Phys.*, 11(12):5603–5624, 2011. doi: 10.5194/acp-11-5603-2011.
- H. R. Byers and R. R. Braham. Thunderstorm Structure and Circulation. *J. Meteor.*, 5(3):71–86, 1948. doi: 10.1175/1520-0469(1948)005<0071:TSAC>2.0.CO;2.
- J. Calbo and J. Sabburg. Feature extraction from whole-sky ground-based images for cloud-type recognition. *J. Atmos. Ocean. Tech.*, 25:3–14, 2008. doi: 10.1176/2007JTECHA959.1.
- D. Cano, J. Monget, M. Albuissou, H. Guillard, N. Regas, and L. Wald. A method for the determination of the global solar radiation from meteorological satellites data. *Sol. Energy*, 37(1):31–39, 1986. doi: 10.1016/0038-092X(86)90104-0.
- J. Casado-Rubio, M. Revuelta, M. Postigo, I. Martinez-Marco, and C. Yague. A Postprocessing Methodology for Direct Normal Irradiance Forecasting Using Cloud Information and Aerosol Load Forecasts. *J. Appl. Meteor. Climatol.*, 56:1595–1608, 2017. doi: 10.1175/JAMC-D-16-0297.1.

- A. Cazorla, C. Husillos, M. Anton, and L. Alados-Arboledas. Multi-exposure adaptive threshold technique for cloud detection with sky imagers. *Sol. Energy*, 114:268–277, 2015. doi: 10.1016/j.solener.2015.02.006.
- S. Chandrasekhar. *Radiative transfer*. Oxford Univ. Press, UK, 1950.
- R. Chauvin, J. Nou, S. Thil, and S. Grieu. Modelling the clear-sky intensity distribution using a sky imager. *Sol. Energy*, 119:1–17, 2015. doi: 10.1016/j.solener.2015.06.026.
- H.-Y. Cheng and C.-L. Lin. Cloud detection in all-sky images via multi-scale neighborhood features and multiple supervised learning techniques. *Atmos. Meas. Tech.*, 10:199–208, 2017. doi: 110.5194/amt-10-199-2017.
- C. W. Chow, B. Urquhart, M. Lave, A. Dominguez, J. Kleissl, J. Shields, and B. Washom. Intra-hour forecasting with a total sky imager at the UC San Diego solar energy testbed. *Sol. Energy*, 85:2881–2893, 2011. doi: 10.1016/j.solener.2011.08.025.
- Y. Chu, H. T. C. Pedro, and C. Coimbra. Hybrid intra-hour DNI forecasts with sky image processing enhanced by stochastic learning. *Sol. Energy*, 98:592–603, 2013. doi: 10.1016/j.solener.2013.10.020.
- Y. Chu, H. T. C. Pedro, L. Nonnenmacher, R. H. Inman, Z. Liao, and C. Coimbra. A smart image-based cloud detection system for intrahour solar irradiance forecasts. *J. Atmos. Ocean. Technol.*, 31:1995–2007, 2014. doi: 10.1175/JTECH-D-13-00209.1.
- S. Cros, O. Liandrat, N. Sebastien, and N. Schmutz. Extracting cloud motion vectors from satellite images for solar power forecasting. In *Geoscience and Remote Sensing Symposium (IGARSS), 2014 IEEE International, Quebec City, Canada*, 2014. doi: 10.1109/IGARSS.2014.6947394.
- A. Dahlback and K. Stamnes. A new spherical model for computing the radiation field available for photolysis and heating at twilight. *Planet. Space Sci.*, 39(5): 671–683, 1991. doi: 10.1016/0032-0633(91)90061-E.
- I. de la Parra, J. Marcos, M. Garcia, and L. Marroyo. Storage requirements for PV power ramp-rate control in a PV fleet. *Sol. Energy*, 118:426–440, 2015. doi: 10.1016/j.solener.2015.05.046.
- H. M. Deneke and R. A. Roebeling. Downscaling of METEOSAT SEVIRI 0.6 and 0.8 μm channel radiances utilizing the high-resolution visible channel. *Atmos. Chem. Phys.*, 10:9761–9772, 2010. doi: 10.5194/acp-10-9761-2010.
- P. Denholm and M. Mehos. Boosting CSP production with thermal energy storage. *Power*, 156(6), 2012.

- M. Derrien, H. Gleau, and M.-P. Raoul. The use of the high resolution visible in SAFNWC/MSG cloud mask. In *2010 EUMETSAT Meteorological Satellite Conference, 20-24 September 2010, Cordoba, Spain*, page 57pp., 2010.
- L. Diabate, H. Demarcq, N. Michaud-Regas, and L. Wald. Estimating incident solar radiation at the surface from images of the earth transmitted by geostationary satellites: the heliosat project. *Int. J. Solar Energy*, 5:261–278, 1988. doi: 10.1080/01425918708914425.
- Y. Eissa, P. R. Marpu, I. Gherboudj, H. Ghedira, T. B. M. J. Ouarda, and M. Chiesa. Artificial neural network based model for retrieval of the direct normal, diffuse horizontal and global horizontal irradiances using SEVIRI images. *Sol. Energy*, 89:1–16, 2013. doi: 10.1016/j.solener.2012.12.008.
- C. Emde, R. Buras-Schnell, A. Kylling, B. Mayer, J. Gasteiger, U. Hamann, J. Kylling, B. Richter, C. Pause, and L. Bugliaro. The libRadtran software package for radiative transfer calculations (Version 2.0). *Geosci. Model Dev.*, 9:1647–1672, 2016. doi: 10.5194/gmd-9-1647-2016.
- EUMETSAT. SEVIRI Modulation Transfer Function (MTF) characterisations for MSG-1, MSG-2 and MSG-3. Tech. rep., EUMETSAT, Darmstadt, Germany, 2006.
- A. Evans. Cloud motion analysis using multichannel correlation-relaxation labeling. *IEEE Geoscience Remote Sensing Letters*, 3(3):392–396, 2006. doi: 10.1109/LGRS.2006.873343.
- H. Feidas and C. Cartalis. Application of an automated cloud-tracking algorithm on satellite imagery for tracking and monitoring small mesoscale convective cloud systems. *Int. J. Remote Sens.*, 26(8):1677–1698, 2005. doi: 10.1080/01431160512331338023.
- M. Fekri and M. K. Yau. An information-theoretical score of dichotomous precipitation forecast. *Mon. Weather Rev.*, 144(4):1633–1647, 2016. doi: 10.1175/MWR-D-15-0225.1.
- J. A. Flueck. A study of some measures of forecast verification. In *10th Conference on Probability and Statistics in Atmospheric Sciences*, pages 69–73, Edmonton, AB, Canada, 1987. Amer. Meteor. Soc.
- V. Fung, J. L. Bosch, S. W. Roberts, and J. Kleissl. Cloud shadow speed sensor. *Atmos. Meas. Tech.*, 7:1693–1700, 2014. doi: 10.5194/amt-7-1693-2014.
- G. Gesell. An algorithm for snow and ice detection using AVHRR data. An extension to the APOLLO software package. *Int. J. Remote Sensing*, 10(4 and 5):897–905, 1989. doi: 10.1080/01431168908903929.

- M. S. Ghonima, B. Urquhart, C. W. Chow, J. E. Shields, A. Cazorla, and J. Kleissl. A method for cloud detection and opacity classification based on ground based sky imagery. *Atmos. Meas. Tech.*, 5:2881–2892, 2012. doi: 10.5194/amt-5-2881-2012.
- A. Gonzalez, B. Mayer, J. F. Gayet, and P. Wendling. Multilayer cirrus cloud property retrieval using dual-view ATSR-2 instrument. *Proc. SPIE*, 4882:224–231, 2003. doi: 10.1117/12.462991.
- J. Gonzalez, E. Serrano, and R. Wiesenbergh. DNI forecasting using coupled WRF and MRM, enhanced with a neural network for CSP applications. In *Proceedings of SolarPACES Conference. Perpignan, France*, 2010.
- D. Goswami and F. Kreith. *Handbook of Energy Efficiency and Renewable Energy*. CRC Press, 2007. ISBN 978-0-8493-1730-9.
- W. Greuell, J. F. Meirink, and P. Wang. Retrieval and validation of global, direct and diffuse irradiance derived from SEVIRI satellite observations. *J. Geophys. Res. Atmos.*, 118:2340–2361, 2013. doi: 10.1002/jgrd.50194.
- A. Gsella, A. de Meij, A. Kerschbaumer, E. Reimer, P. Thunis, and C. Cuvelier. Evaluation of MM5, WRF and TRAMPER meteorology over the complex terrain of the Po Valley, Italy. *Atmos. Environ.*, 89:797 – 806, 2014. doi: 10.1016/j.atmosenv.2014.03.019.
- C. A. Gueymard. Clear-sky irradiance predictions for solar resource mapping and large-scale applications: Improved validation methodology and detailed performance analysis of 18 broadband radiative models. *Sol. Energy*, 86(8): 2145–2169, 2012a. doi: 10.1016/j.solener.2011.11.011.
- C. A. Gueymard. Temporal variability in direct and global irradiance at various time scales as affected by aerosols. *Sol. Energy*, 86:3544–3553, 2012b.
- A. Hammer, D. Heinemann, E. Lorenz, and Lücke. Short-term forecasting of solar radiation: a statistical approach using satellite data. *Sol. Energy*, 67: 139–150, 1999. doi: 10.1016/S0038-092X(00)00038-4.
- A. Hammer, E. Lorenz, A. Kemper, D. Heinemann, H. Beyer, K. Schumann, and M. Schwandt. Direct Normal Irradiance for CSP based on satellite images of Meteosat Second Generation. In *Proceedings of 15th SolarPACES Conference, Berlin, Germany*, 2009.
- J. Hansen and L. Travis. Light scattering in planetary atmospheres. *Space Sci. Rev.*, 16:527–610, 1974.
- A. W. Hanssen and W. Kuipers. On the relationship between the frequency of rain and various meteorological parameters. *Koninklijk Ned. Meteor. Instit., Meded. Verhand.*, 81:2–15, 1965.

- A. Heinle, A. Macke, and A. Srivastav. Automatic cloud classification of whole sky images. *Atmos. Meas. Tech.*, 3:557–567, 2010. doi: 10.5194/amt-3-557-2010.
- C. C. Henken, M. J. Schmeits, H. Deneke, and R. A. Roebeling. Using MSG-SEVIRI Cloud Physical Properties and weather Radar Observations for the Detection of Cb/TCu Clouds. *J. Appl. Meteor. Climatol.*, 50:1587–1600, 2011. doi: 10.1175/2011JAMC2601.1.
- J. S. Henzing, W. H. Knap, P. Stammes, A. Apituley, J. B. Bergwerff, D. P. J. Swart, G. P. A. Kos, and H. M. ten Brink. Effect of aerosols on the downward shortwave irradiances at the surface: Measurements versus calculations with MODTRAN4.1. *J. Geophys. Res.*, 109:D14204, 2004. doi: 10.1029/2003JD004142.
- A. M. Hering, C. Morel, G. Galli, S. Senesi, P. Ambrosetti, and M. Boscacci. Nowcasting thunderstorms in the Alpine region using a radar based adaptive thresholding scheme. In *Proc. 3rd European Conference on Radar Meteorology, Visby, Sweden*, pages 206–211, 2004.
- T. Hirsch. Direct normal irradiance nowcasting methods for optimized operation of concentrating solar technologies. *DNICast, Deliverable Nr. 2.1*, 2014.
- J. Huang, P. Minnis, B. Lin, Y. Yi, M. Khaiyer, R. Arduini, A. Fan, and G. Mace. Advanced retrievals of multilayered cloud properties using multispectral measurements. *J. Geophys. Res.*, 110(D15):2156–2202, 2005. doi: 10.1029/2004JD005101.
- ISO-9488. Solar Energy: Vocabulary. 1999.
- C. P. Jacovides, M. D. Steven, and D. N. Asimakopoulos. Spectral solar irradiance and some optical properties for various polluted atmospheres. *Sol. Energy*, 69(3):215–227, 2000. doi: 10.1016/S0038-092X(00)00062-1.
- J. Joiner, A. P. Vasilkov, P. K. Bhartia, G. Wind, S. Platnick, and W. P. Menzel. Detection of multi-layer and vertically-extended clouds using A-train sensors. *Atmos. Meas. Tech.*, 3:233–247, 2010. doi: 10.5194/amt-3-233-2010.
- E. Kassianov, C. Long, and J. Christy. Cloud-base-height estimation from paired ground-based hemispherical observations. *J. Appl. Meteorol.*, 44:1221–1233, 2005. doi: 10.1175/JAM2277.1.
- S. Kato, T. Ackerman, J. Mather, and E. Clothiaux. The k-distribution method and correlated-k approximation for a shortwave radiative transfer model. *J. Quant. Spectrosc. Radiat. Transfer*, 62:109–121, 1999. doi: 10.1016/S0022-4073(98)00075-2.
- A. Kazantzidis, P. Tzoumanikas, A. F. Bais, S. Fotopoulos, and G. Economou. Cloud detection and classification with the use of whole-sky ground-based images. *Atmos. Res.*, 113:80–88, 2012. doi: 10.1016/j.atmosres.2012.05.005.

- Kipp & Zonen. CHP1 Pyrheliometer Instruction Manual (version 0811). 2008.
- L. Klüser, D. Rosenfeld, A. Macke, and T. Holzer-Popp. Observations of shallow convective clouds generated by solar heating of dark smoke plumes. *Atmos. Chem. Phys.*, 8:2833–2840, 2008. doi: 10.5194/acp-8-2833-2008.
- I. Koren, L. Oreopoulos, G. Feingold, L. A. Remer, and O. Altaratz. How small is a small cloud? *Atmos. Chem. Phys.*, 8:3855–3864, 2008. doi: 10.5194/acp-8-3855-2008.
- S. Kox, L. Bugliaro, and A. Ostler. Retrieval of cirrus cloud optical thickness and top altitude from geostationary remote sensing. *Atmos. Meas. Tech.*, 7(10): 3233–3246, 2014. doi: 10.5194/amt-7-3233-2014.
- B. Kraas, M. Schroedter-Homscheidt, and R. Madlener. Economic merits of a state-of-the-art concentrating solar power forecasting system for participation in the Spanish electricity market. *Sol. Energy*, 93:244–255, 2013.
- K. Kriebel, R. Saunders, and G. Gesell. Optical properties of clouds derived from fully cloudy AVHRR pixels. *Beitr. Phys. Atmosph.*, 62:165–171, 1989.
- K.-T. Kriebel, G. Gesell, M. Kästner, and H. Mannstein. The cloud analysis tool APOLLO: improvements and validation. *Int. J. Rem. Sens.*, 24(12):2389–2408, 2003. doi: 10.1080/01431160210163065.
- P. Kuhn, B. Nouri, S. Wilbert, T. Schmidt, C. Prah, Z. Yasser, L. Ramirez, L. Zarzalejo, L. Vuilleumier, P. Blanc, and R. Pitz-Paal. Validation of an all sky imager based nowcasting system for industrial PV plants. In *Abstract for the 33rd European PV Solar Energy Conference and Exhibition, September 2017, Amsterdam, Netherlands*, 2017.
- B. Kurtz and J. Kleissl. Measuring diffuse, direct, and global irradiance using a sky imager. *Sol. Energy*, 141:311–322, 2017. doi: 10.1016/j.solener.2016.11.032.
- A. Kylling, K. Stamnes, and S.-C. Tsay. A reliable and efficient two-stream algorithm for spherical radiative transfer: documentation of accuracy in realistic layered media. *J. Atmos. Chem.*, 21:115–150, 1995.
- A. A. Lacis and V. Oinas. A description of the correlated k-distribution method for modeling nongray gaseous absorption, thermal emission, and multiple scattering in vertically inhomogeneous atmospheres. *J. Geophys. Res.*, 96(D5): 9027–9063, 1991. doi: 10.1029/90JD01945.
- P. Lang. Cell tracking and warning indicators derived from operational radar products. In *30th International Conference on Radar Meteorology, Munich, Germany*, 2001.

- E. Law, M. Kay, and R. Taylor. Evaluating the benefits of using short-term direct normal irradiance forecasts to operate a concentrated solar thermal power plant. *Sol. Energy*, 140:93–108, 2016. doi: 10.1016/j.solener.2016.10.037.
- D. T. Lee and B. J. Schachter. Two algorithms for constructing a delaunay triangulation. *International Journal of Computer & Information Sciences*, 9(3):219–242, 1980.
- M. Lefevre, A. Oumbe, P. Blanc, B. Espinar, B. Gschwind, Z. Qu, L. Wald, M. Schroedter-Homscheidt, C. Hoyer-Klick, A. Arola, A. Benedetti, J. Kaiser, and J. Morcrette. McClear: a new model estimating downwelling solar radiation at ground level in clear-sky conditions. *Atmos. Meas. Tech.*, 6:2403–2418, 2013. doi: 10.5194/amt-6-2403-2013.
- Q. Li, W. Lu, and J. Yang. A Hybrid Thresholding Algorithm for Cloud Detection on Ground-Based Color Images. *J. Atm. Ocean. Technol.*, 28:1286–1296, 2011. doi: 10.1175/JTECH-D-11-00009.1.
- K. Liou. *An introduction to atmospheric radiation*. Academic Press, 2002. ISBN 978-0124514515. 2nd edition.
- S. Lohmann. *Langzeitvariabilität der globalen und direkten Solarstrahlung für Solarenergieanwendungen*. PhD Thesis, Fakultät für Physik der Ludwig-Maximilians-Universität München, 2006.
- E. Lorenz, J. Remund, S. Müller, S. Traunmüller, G. Steinmaurer, D. Pozo, J. A. Ruiz-Arias, V. L. Fanego, L. Ramirez, M. G. Romeo, C. Kurz, L. M. Pomares, and C. Guerrero. Benchmarking of different approaches to forecast solar irradiance. In *24th European Photovoltaic Solar Energy Conference, September 2009, Hamburg, Germany*, pages 4199–4208, 2009.
- E. Lorenz, J. Kühnert, and D. Heinemann. Short term forecasting of solar irradiances by combining satellite data and numerical weather predictions. In *27th European Photovoltaic Solar Energy Conference and Exhibition, Frankfurt, Germany*, pages 4401–4405, 2012.
- G. Mace, E. Clothiaux, and T. Ackerman. The composite characteristics of cirrus clouds: bulk radiative properties revealed by one year of continuous cloud radar data. *J. Climate*, 14:2185–2203, 2001.
- J. Marcos, O. Storkel, L. Marroyo, M. Garcia, and E. Lorenzo. Storage requirements for PV power ramp-rate control. *Sol. Energy*, 99:28–35, 2014. doi: 10.1016/j.solener.2013.10.037.
- R. Marquez and C. F. M. Coimbra. Forecasting of global direct solar irradiance using stochastic learning methods, ground experiments and the NWS database. *Sol. Energy*, 85(5):746–756, 2011.

- R. Marquez and C. F. M. Coimbra. Intra-hour DNI forecasting based on cloud tracking image analysis. *Sol. Energy*, 91:327–336, 2013. doi: 10.1016/j.solener.2012.09.018.
- R. Marquez, H. T. C. Pedro, and C. F. M. Coimbra. Hybrid solar forecasting method uses satellite imaging and ground telemetry as inputs to ANNs. *Sol. Energy*, 92:176–188, 2013. doi: 10.1016/j.solener.2013.02.023.
- P. Mathiesen, C. Collier, and J. Kleissl. A high-resolution, cloud-assimilating numerical weather prediction model for solar irradiance forecasting. *Sol. Energy*, 92:47–61, 2013. doi: 10.1016/j.solener.2013.02.018.
- B. Mayer and A. Kylling. Technical Note: The libRadtran software package for radiative transfer calculations: Description and examples of use. *Atmos. Chem. Phys.*, 5:1855–1877, 2005. doi: 10.5194/acp-5-1855-2005.
- J. F. Meirink, R. A. Roebeling, and P. Stammes. Inter-calibration of polar imager solar channels using SEVIRI. *Atmos. Meas. Tech.*, 6:2495–2508, 2013. doi: 10.5194/amt-6-2495-2013.
- D. Merk and T. Zinner. Detection of convective initiation using Meteosat SEVIRI: implementation in and verification with the tracking and nowcasting algorithm Cb-TRAM. *Atmos. Meas. Tech.*, 6:1903–1918, 2013. doi: 10.5194/amt-6-1903-2013.
- G. Mie. Beiträge zur Optik trüber Medien, speziell kolloidaler Metallösungen. *Ann. Phys.*, 330(3):377–445, 1908. doi: 10.1002/andp.19083300302.
- Mobotix. Q24m camera manual. 2013.
- M. Möhrlein. *Nowcasting der Wolkenbedeckung für verschiedene Wolkenetagen auf Basis von Meteosatdaten zur Anwendung auf die Einstrahlungsprognose von Solarkraftwerken*. Master Thesis, LMU München, 2013.
- S. Müller and J. Remund. Shortest term regional solar energy forecast for the next 1 to 6 hours. In *28th European Photovoltaic Solar Energy Conference and Exhibition, Paris, France*, 2013. doi: 10.4229/28thEUPVSEC2013-5AO.9.1.
- S. Müller and J. Remund. Shortest term forecasting of DNI for concentrated solar technologies. In *32nd European Photovoltaic Solar Energy Conference and Exhibition, June 2016, Munich*, pages 1490–1492, 2016. doi: 10.4229/EUPVSEC20162016-5AO.8.5.
- T. Nakajima and M. King. Determination of the optical thickness and effective particle radius of clouds from reflected solar radiation measurements. Part I: Theory. *J. Atmos. Sci.*, 47:1878–1893, 1990. doi: 10.1175/1520-0469(1990)047<1878:DOTOTA>2.0.CO;2.

- T. Nakajima and T. Nakajima. Wide-area determination of cloud microphysical properties from NOAA AVHRR measurements for FIRE and ASTEX regions. *J. Atmos. Sci.*, 52:4043–4059, 1995. doi: 10.1175/1520-0469(1995)052<4043:WADCOM>2.0.CO;2.
- H. Nazaryan, M. P. McCormick, and W. P. Menzel. Global characterization of cirrus clouds using CALIPSO data. *J. Geophys. Res.*, 113, D16211, 2008. doi: 10.1029/2007LD009481.
- D. Nguyen and J. Kleissl. Stereographic methods for cloud base height determination using two sky imagers. *Sol. Energy*, 107:495–509, 2014. doi: 10.1016/j.solener.2014.05.005.
- E. Nikitidou, A. Kazantzidis, and V. Salamalikis. The aerosol effect on direct normal irradiance in Europe under clear skies. *Ren. Energy*, 68:475–484, 2014. doi: 10.1016/j.renene.2014.02.034.
- C. S. Peirce. The numerical measure of the success of predictions. *Science*, 4(93): 453–454, 1884. doi: 10.1126/science.ns-4.93.453-a.
- Z. Peng, D. Yu, D. Huang, J. Heiser, S. Yoo, and P. Kalb. 3D cloud detection and tracking system for solar forecast using multiple sky imagers. *Sol. Energy*, 118:496–519, 2015. doi: 10.1016/j.solener.2015.05.037.
- Z. Peng, D. Yu, D. Huang, J. Heiser, and P. Kalb. A hybrid approach to estimate the complex motions of clouds in sky images. *Sol. Energy*, 138:10–25, 2016. doi: 10.1016/j.solener.2016.09.002.
- R. Perez, S. Kivalov, J. Schlemmer, K. Hemker Jr., D. Renne, and T. E. Hoff. Validation of short and medium term operational solar radiation forecasts in the US. *Sol. Energy*, 84:2161–2172, 2010. doi: 10.1016/j.solener.2010.08.014.
- G. W. Petty. *A first course in atmospheric radiation*. Sundog Publishing, Madison, Wisconsin, 2006. ISBN 978-0-9729033-1-8. 2nd edition.
- M. Planck. Über das Gesetz der Energieverteilung im Normalspektrum. *Ann. Phys.*, 309:553–563, 1901. doi: 10.1002/andp.19013090310.
- A. Prsa, P. Harmanec, G. Torres, E. Mamajek, M. Asplund, N. Capitaine, J. Christensen-Dalsgaard, E. Depagne, M. Haberreiter, S. Hekker, J. Hilton, G. Kopp, V. Kostov, D. W. Kurtz, J. Laskar, B. D. Mason, E. F. Milone, M. Montgomery, M. Richards, W. Schmutz, J. Schou, and S. G. Stewart. Nominal values for selected solar and planetary quantities: IAU 2015 Resolution B3. *Astron. J.*, 152:41–47, 2016. doi: 10.3847/0004-6256/152/2/41.
- Z. Qu, A. Oumbe, P. Blanc, B. Espinar, G. Gesell, B. Gschwind, L. Klüser, M. Lefevre, L. Saboret, M. Schroedter-Homscheidt, and L. Wald. Fast radiative transfer parameterisation for assessing the surface solar irradiance:

- The Heliosat-4 method. *Meteorologische Zeitschrift*, 26(1):33–57, 2016. doi: 10.1127/metz/2016/0781.
- S. Quesada-Ruiz, Y. Chu, J. Toivas-Pescador, H. T. C. Pedro, and C. F. M. Coimbra. Cloud-tracking methodology for intra-hour DNI forecasting. *Sol. Energy*, 102:267–275, 2014. doi: 10.1016/j.solener.2014.01.030.
- Renewable Energy Policy Network for the 21st Century (REN21). Renewables 2016: Global Status Report. 2016. URL <http://www.ren21.net>.
- M. Reuter and J. Fischer. A comparison of satellite-retrieved and simulated cloud coverage in the Baltic Sea area as part of the BALTIMOS project. *Theor. Appl. Climatol.*, 118:695–706, 2014. doi: 10.1007/s00704-009-0208-8.
- M. Reuter, W. Thomas, P. Albert, M. Lockhoff, R. Weber, K.-G. Karlsson, and J. Fischer. The CM-SAF and FUB Cloud Detection Schemes for SEVIRI: Validation with Synoptic Data and Initial Comparison with MODIS and CALIPSO. *J. Appl. Meteor. Climatol.*, 48(2):301–316, 2009. doi: 10.1175/2008JAMC1982.1.
- C. Rigollier, O. Bauer, and L. Wald. On the clear sky model of the ESRA - European Solar Radiation Atlas with respect to the Heliosat method. *Sol. Energy*, 68(1):33–48, 2000. doi: 10.1016/S0038-092X(99)00055-9.
- C. Rigollier, M. Lefevre, and L. Wald. The method heliosat-2 for deriving short-wave solar radiation data from satellite images. *Sol. Energy*, 77:159–169, 2004. doi: 10.1016/j.solener.2004.04.017.
- K. Sassen and J. Campbell. A midlatitude cirrus cloud climatology from the facility for atmospheric remote sensing. Part I: Macrophysical and synoptic parameters. *J. Atmos. Sci.*, 58:481–496, 2001.
- R. Saunders and K. Kriebel. An improved method for detecting clear sky and cloudy radiances from AVHRR data. *Int. J. Remote Sensing*, 9(1):123–150, 1988. doi: 10.1080/01431168808954841.
- D. Scaramuzza. *Omindirectional vision: from calibration to robot motion estimation*. PhD Thesis, ETH Zürich, 2008.
- D. Scaramuzza, A. Martinelli, and R. Siegwart. A toolbox for easily calibrating omnidirectional cameras. In *IEEE/RSJ International Conference on Intelligent Robots and Systems, Oct 2006, Beijing, China*, pages 5695–5701, 2006. doi: 10.1109/IROS.2006.282372.
- C. Schaaf, F. Gao, A. Strahler, W. Lucht, X. Li, T. Tsang, N. Strugnell, X. Zhang, Y. Jin, J.-P. Muller, P. Lewis, M. Barnsley, P. Hobson, M. Disney, G. Roberts, M. Dunderdale, C. Doll, R. d’Entremont, B. Hu, S. Liang, J. Privette, and D. Roy. First Operational BRDF, Albedo and Nadir Reflectance Products

- from MODIS. *Rem. Sens. Environ.*, 83:135–148, 2002. doi: 10.1016/S0034-4257(02)00091-3.
- J. Schmetz, K. Holmlund, J. Hoffman, B. Strauss, B. Mason, V. Gaertner, A. Koch, and L. Van De Berg. Operational cloud-motion winds from Meteosat infrared images. *J. Appl. Meteorol.*, 32:1206–1225, 1993. doi: 10.1175/1520-0450(1993)032<1206:OCMWFM>2.0.CO;2.
- J. Schmetz, P. Pili, S. Tjemkes, D. Just, J. Kerkmann, S. Rota, and A. Ratier. An introduction to Meteosat Second Generation (MSG). *Bull. Amer. Meteor. Soc.*, 83(7):977–992, 2002. doi: 10.1175/1520-0477(2002)083<0977:AITMSG>2.3.CO;2.
- T. Schmidt, J. Kalisch, E. Lorenz, and D. Heinemann. Retrieval of direct and diffuse irradiance with the use of hemispheric sky images. In *3rd International Conference Energy & Meteorology, June 2015, Boulder, Co*, 2015.
- T. Schmidt, J. Kalisch, E. Lorenz, and D. Heinemann. Evaluating the spatio-temporal performance of sky-imager-based solar irradiance analysis and forecasts. *Atmos. Chem. Phys.*, 16:3399–3412, 2016. doi: 10.5194/acp-16-3399-2016.
- U. Schumann, B. Mayer, K. Gierens, S. Unterstrasser, P. Jessberger, A. Petzold, and C. Voigt. Effective Radius of Ice Particles in Cirrus and Contrails. *J. Atmos. Sci.*, 68:300–321, 2011. doi: 10.1175/2010JAS3562.1.
- E. Shettle. Models of aerosols, clouds and precipitation for atmospheric propagation studies. In *Atmospheric propagation in the UV, visible, IR and MM-wave region and related system aspects, AGARD Conference Proceedings*, 1989.
- T. Sirch, L. Bugliario, T. Zinner, M. Moehrlein, and M. Vazquez-Navarro. Cloud and DNI nowcasting with MSG/SEVIRI for the optimized operation of concentrating solar power plants. *Atmos. Meas. Tech.*, 10:409–429, 2017. doi: 10.5194/amt-10-409-2017.
- K. Stamnes, S.-C. Tsay, W. Wiscombe, and I. Laszlo. DISORT, a General-Purpose Fortran Program for Discrete-Ordinate-Method Radiative Transfer in Scattering and Emitting Layered Media: Documentation of Methodology. Technical report, Dept. of Physics and Engineering Physics, Stevens Institute of Technology, Hoboken, NJ 07030, 2000.
- D. B. Stephenson. Use of the "odds ratio" for diagnosing forecast skill. *Weather Forecast.*, 15(2):221–232, 2000. doi: 10.1175/1520-0434(2000)015<0221:UOTORF>2.0.CO;2.
- H. J. W. Strutt. On the scattering of light by small particles. *Philosophical Magazine Series 4*, 41(275):447–454, 1871. doi: 10.1080/14786447108640507.

- N. Tartaglione. Relationship between Precipitation Forecast Errors and Skill Scores of Dichotomous Forecasts. *Weather and Forecasting*, 25(1):355–365, 2010. doi: 10.1175/2009WAF2222211.1.
- G. E. Thomas and K. Stamnes. *Radiative Transfer in the Atmosphere and Ocean*. Cambridge Atmospheric and Space Science Series, 1999.
- B. Urquhart, B. Kurtz, E. Dahlin, M. Ghonima, J. Shields, and J. Kleissl. Development of a sky imaging system for short-term solar power forecasting. *Atmos. Meas. Tech.*, 8:875–890, 2015. doi: 10.5194/amt-8-875-2015.
- U.S. Energy Information Administration (EIA). International energy outlook 2016. 2016. URL <http://www.eia.gov/outlooks/ieo/>.
- J. M. Wallace and P. V. Hobbs. *Atmospheric Science: an introductory survey*. Academic Press, 1977.
- G. Wang, B. Kurtz, and J. Kleissl. Cloud base height from sky imager and cloud speed sensor. *Sol. Energy*, 131:208–221, 2016. doi: 10.1016/j.solener.2016.02.027.
- S. R. West, D. Rowe, S. Sayeef, and A. Berry. Short-term irradiance forecasting using skycams: motivation and development. *Sol. Energy*, 110:188–207, 2014. doi: 10.1016/j.solener.2014.08.038.
- D. M. Winker, M. A. Vaughan, A. Omar, Y. Hu, K. A. Powell, Z. Liu, W. H. Hunt, and S. A. Young. Overview of the CALIPSO Mission and CALIOP Data Processing Algorithms. *J. Atmos. Oceanic Technol.*, 26:2310–2323, 2009. doi: 10.1175/2009JTECHA1281.1.
- D. M. Winker, J. Pelon, J. A. Coakley, S. A. Ackerman, R. J. Charlson, P. R. Colarco, P. Flamant, Q. Fu, R. M. Hoff, C. Kittaka, T. L. Kubar, H. Le Treut, M. P. McCormick, G. Mégie, L. Poole, K. Powell, C. Trepte, M. A. Vaughan, and B. A. Wielicki. The CALIPSO Mission: A Global 3D View of Aerosols and Clouds. *Bulletin of the American Meteorological Society*, 91(9):1211–1229, 2010. doi: 10.1175/2010BAMS3009.1.
- WMO. *Guide to meteorological instruments and methods of observation*. 2014. ISBN 978-92-63-10008-5.
- E. L. A. Wolters, H. M. Deneke, B. J. J. M. van den Hurk, J. F. Meirink, and R. A. Roebeling. Broken and inhomogeneous cloud impact on satellite cloud particle effective radius and cloud-phase retrievals. *J. Geophys. Res.*, 115(D10214), 2010. doi: 10.1029/2009JD012205.
- P. Wood-Bradley, J. Zapata, and J. Pye. Cloud tracking with optical flow for short-term solar forecasting. In *50th Conference of the Australian Solar Energy Society, Melbourne*, 2012.

- F. Woodcock. The Evaluation of Yes/No Forecasts for Scientific and Administrative Purposes. *Monthly Weather Review*, 104(10):1209–1214, 1976. doi: 10.1175/1520-0493(1976)104<1209:TEOYFF>2.0.CO;2.
- Q. X. Wu. A correlation-relaxation-labeling framework for computing optical flow: Template matching from a new perspective. *IEEE Trans. Pattern Anal. Mach. Intell.*, 17(8):843–853, 1995.
- Q. X. Wu, S. J. McNeill, and D. Pairman. Correlation and relaxation labelling: An experimental investigation on fast algorithms. *Int. J. Remote Sens.*, 18(3): 651–662, 1997.
- H. Yang, B. Kurtz, D. Nguyen, B. Urquhart, C. W. Chow, M. Ghonima, and J. Kleissl. Solar irradiance forecasting using a ground-based sky imager developed at UC San Diego. *Sol. Energy*, 103:502–524, 2014. doi: 10.1016/j.solener.2014.02.044.
- J. Yang, Q. Min, W. Lu, W. Yao, Y. Ma, J. Du, T. Lu, and G. Liu. An automated cloud detection method based on the green channel of total-sky visible images. *Atmos. Meas. Tech.*, 8:4671–4679, 2015. doi: 10.5194/amt-8-4671-2015.
- J. Yang, Q. Min, W. Lu, Y. Ma, W. Yao, J. Lu, T. Du, and G. Liu. A total sky cloud detection method using real clear sky background. *Atmos. Meas. Tech.*, 9:587–597, 2016. doi: 10.5194/amt-9-587-2016.
- W. Zdunkowski, T. Trautmann, and A. Bott. *Radiation in atmosphere, A course in theoretical meteorology*. Cambridge University Press, 2007. ISBN 978-0521871075.
- J. Zhang, A. Florita, B.-M. Hodge, S. Lu, H. F. Hamann, V. Banunarayanan, and A. M. Brockway. A suite of metrics for assessing the performance of solar power forecasting. *Sol. Energy*, 111:157–175, 2015. doi: 10.1016/j.solener.2014.10.016.
- T. Zinner, H. Mannstein, and A. Tafferner. Cb-TRAM: Tracking and monitoring severe convection from onset over rapid development to mature phase using multi-channel Meteosat-8 SEVIRI data. *Meteorology and Atmospheric Physics*, 101(3-4):191–210, doi: 10.1007/s00703-008-0290-y, 2008.
- T. Zinner, C. Forster, E. de Coning, and H.-D. Betz. Validation of the Meteosat storm detection and nowcasting system Cb-TRAM with lightning network data - Europe and South Africa. *Atmos. Meas. Tech.*, 6:1567–1583, 2013. doi: 10.5194/amt-6-1567-2013.

List of abbreviations

AERONET	AERosol RObotic NETwork
ANN	Artificial Neural Networks
AOD	Aerosol Optical Depth
APICS	Algorithm for the Physical Investigation of Clouds with SEVIRI
ASI	All-Sky Imager
Cb-TRAM	CumulonimBus TRacking And Monitoring
CBH	Cloud Base Height
CTH	Cloud Top Height
CMV	Cloud Motion Vectors
COCS	Cirrus Optical properties derived from CALIOP and SEVIRI during day and night
CSP	Concentrating Solar Power
DFD	German Remote Sensing Data Center
DHI	Diffuse Horizontal Irradiance
DNI	Direct Normal Irradiance
ECMWF	European Centre for Medium-range Weather Forecasts
EUMETSAT	EUropean organisation for the exploitation of METeorological SATellites
GHI	Global Horizontal Irradiance
HK	Hanssen-Kuiper
HRES	High RESolution
HRV	High Resolution Visible
libRadtran	library for Radiative transfer
LRES	Low RESolution
LUT	Look-Up Table
MAE	Mean Absolute Error
MBE	Mean Bias Error
MODIS	MODerate-resolution Imaging Spectroradiometer
MSG	Meteosat Second Generation
MT	Meteotest
NWP	Numerical Weather Prediction
PSA	Plataforma Solar de Almeria
PSF	Point Spread Function
RMSE	Root Mean Squared Error
SEVIRI	Spinning Enhanced Visible and Infrared Imager
TOA	Top Of Atmosphere

Danksagung

Diese Arbeit wäre ohne die Hilfe zahlreicher Personen nicht möglich gewesen, bei denen ich mich an dieser Stelle bedanken möchte.

Dieser Dank gilt zuallererst meinem Doktorvater Prof. Dr. Bernhard Mayer dafür, der mir nicht nur die Gelegenheit zur Durchführung dieser Arbeit gegeben hat, sondern auch mit interessanten Ratschlägen, Anmerkungen und Ideen wesentlich zum Erfolg dieser Arbeit beigetragen hat. Bedanken möchte ich mich auch bei Prof. Dr. Markus Rapp für seine konstruktiven Verbesserungsvorschläge und die Übernahme des Zweitgutachtens.

Ein ganz besonderer Dank gilt Dr. Luca Bugliaro für seine inspirierende, motivierende und lehrreiche Betreuung während der vergangenen Jahre. Seine Hilfsbereitschaft, sein umfassendes Wissen auf dem Gebiet der Fernerkundung der Atmosphäre und seine wertvollen Ratschläge waren für mich eine unschätzbare Hilfe.

Bedanken möchte ich mich auch bei Tobias Zinner, Kaspar Graf, Andre Butz und Johann Strandgren für ihre hilfreichen Ratschläge und Anmerkungen sowie zahlreichen Diskussionen, sowie bei Marion Schroedter-Homscheidt für die inspirierenden Gespräche und die gute Zusammenarbeit innerhalb des Projekts.

Dieser Dank gilt natürlich auch allen Kolleginnen und Kollegen der Abteilung, deren Arbeitsatmosphäre und Zusammenhalt ich sehr zu schätzen gelernt habe und ebenso den Kolleginnen und Kollegen des Meteorologischen Instituts der LMU München.

Bedanken möchte ich mich bei meiner Familie, die mich in allen Lebenslagen unterstützt hat und natürlich besonders bei meinen Eltern, ohne die diese Arbeit nicht möglich gewesen wäre.